

PRECISION ROTATION RATE MEASUREMENTS WITH A
MOBILE ATOM INTERFEROMETER

A DISSERTATION
SUBMITTED TO THE DEPARTMENT OF PHYSICS
AND THE COMMITTEE ON GRADUATE STUDIES
OF STANFORD UNIVERSITY
IN PARTIAL FULFILLMENT OF THE REQUIREMENTS
FOR THE DEGREE OF
DOCTOR OF PHILOSOPHY

Ken Takase
January 2008

© Copyright by Ken Takase 2008

All Rights Reserved

I certify that I have read this dissertation and that, in my opinion, it is fully adequate in scope and quality as a dissertation for the degree of Doctor of Philosophy.

(Mark Kasevich) Principal Adviser

I certify that I have read this dissertation and that, in my opinion, it is fully adequate in scope and quality as a dissertation for the degree of Doctor of Philosophy.

(Philip Bucksbaum)

I certify that I have read this dissertation and that, in my opinion, it is fully adequate in scope and quality as a dissertation for the degree of Doctor of Philosophy.

(Steven Kahn)

Approved for the University Committee on Graduate Studies.

Abstract

The development and operation of a mobile atom interferometer for precision rotation rate, linear acceleration, and gravity gradient measurements is described. Different inertially and gravitationally sensitive configurations are explored using light-pulse matter wave interferometry in a dual atomic fountain. A four-pulse $\frac{\pi}{2} - \pi - \pi - \frac{\pi}{2}$ gyroscope interferometer sequence is demonstrated, and the rotational sensitivity due to the Sagnac effect is evaluated. A proof-of-principle measurement of the Earth's rotation rate is made, with an accuracy of $\Omega/\Omega_E = 1.0007 \pm 0.0005$. A technique for suppressing contributions from multiple interference paths resulting from inefficiencies in the atom optics is presented and implemented. Also, a method of using conventional inertial sensors to compensate for high frequency vibration noise in the optical delivery system, which currently limits the interferometer performance, is demonstrated. The sensitivity to linear accelerations using a three-pulse $\frac{\pi}{2} - \pi - \frac{\pi}{2}$ interferometer sequence is characterized by measuring the gravitational acceleration due to a test mass. A zero dead time scheme for continuous monitoring of a local oscillator in an atomic clock is demonstrated, and its extension to inertial measurements is discussed. New interferometer laser-pulse sequences are considered for a rotation rate measurement with the vibrationally-induced phase noise suppressed, and for a continuous differential velocity measurement for navigation applications. Finally, the parallel development of a compact laser system and control system is described.

Acknowledgement

I am deeply indebted to my advisor Prof. Mark Kasevich for all his guidance and support over the years. He is both a talented researcher and an extraordinary teacher, and I have learned so much from both his knowledge of physics and his approach to problem-solving. In the summer of 2002, Mark moved his labs from Yale back to Stanford where he began his own graduate career, and I was fortunate enough to have been given the opportunity to tag along, for which I will always be grateful.

Throughout my graduate career I have had the pleasure of working with many great and talented people. Postdocs Kai Bongs, Matt Cashen, Jeff Fixler, and Todd Kawakami were kind enough to show me the ropes early on, when I had no idea what I was doing. I am grateful to Brent Young and Todd Gustavson for all the help they have given me over the years, and for putting up with my incessant phone calls even long after they had left. I am thankful for the insightful discussions and generous advice that Louis Deslauriers has provided me over the past year. Also, thanks to John Stockton for his help and for taking over the experiment, ensuring that it will be at least another year before it gets completely dismantled and cannibalized like the old gradiometer and gyro. Big thanks to fellow grad students Grant Biedermann, Xianan Wu, Sean Roy, and Chetan Mahadeswaraswamy for their invaluable assistance in the lab, and for always being there with helpful suggestions or to just bounce ideas off of. Also gone but not forgotten are the efforts of Wei Li, Mingchang Liu, Mike Minar, Hui-Chun Chien, Jessie Petricka, and countless other students who have contributed to the experiment. I also appreciate the work that Paul Bayer and Larry Novak have put into this project, as well as Karlheinz Merkle and the rest of the machine shop crew.

Special thanks to Jeff, Kamal, Tony, Nes, Chris, Marc, and all of my other great friends for keeping me grounded and for always being there for me. Without all of them, California never would have felt like home. Finally, I would like to thank my family and Vannie for their continued love and support.

Contents

Abstract	v
Acknowledgement	vi
1 Introduction	1
1.1 Rotation Measurements	1
1.2 Atom Interferometry	2
1.3 Overview	4
2 Gyroscopes	6
2.1 Gyroscope Applications	6
2.1.1 Inertial Navigation	6
2.1.2 Geophysics	7
2.1.3 General Relativity	9
2.2 Gyroscope Metrics	11
2.2.1 Angle Random Walk	11
2.2.2 Bias and Scale Factor Stability	12
2.3 Gyroscope Technologies	13
2.3.1 Mechanical Gyroscopes	13
2.3.2 Interferometric Gyroscopes	14
2.3.3 The Sagnac Effect	15
2.3.4 Other Gyroscope Technologies	17
2.3.5 Gyroscope Performance Comparison	18

3	Laser Manipulation of Atoms	21
3.1	Atomic Structure of Cesium	21
3.2	Two-Level System Dynamics	23
3.3	Laser Cooling	25
3.3.1	Doppler Cooling	25
3.3.2	Sub-Doppler Cooling	27
3.4	Magneto-Optical Trap	27
3.5	Atomic Fountain	28
3.6	Two-Photon Stimulated Raman Transitions	28
4	Atom Interferometer Theory	32
4.1	Differential Phase Shifts	32
4.2	The Path Integral Approach	33
4.2.1	Propagation Phase	36
4.2.2	Separation Phase	37
4.2.3	Laser Interaction Phase	38
4.3	Interferometer Pulse Sequences	40
4.3.1	Three-Pulse Accelerometer: $\frac{\pi}{2} - \pi - \frac{\pi}{2}$	40
4.3.2	Four-Pulse Gyroscope: $\frac{\pi}{2} - \pi - \pi - \frac{\pi}{2}$	47
5	Experimental Apparatus	49
5.1	Compact Laser System	49
5.1.1	Master Lasers	51
5.1.2	Amplifier Lasers	53
5.1.3	Tapered Amplifiers	53
5.2	Control System and Electronics	55
5.2.1	Microwave Frequency Generation	57
5.3	Sensor Hardware	57
5.4	Vacuum System	59
5.5	Magnetic Field Control	61

6 Interferometer Operation	65
6.1 Atom Loading and Launching	65
6.2 State Preparation	67
6.3 Raman Beam Configuration	68
6.4 Detection System	74
6.4.1 Signal-to-Noise Ratio	76
7 Rotation Rate Measurements	78
7.1 Four-Pulse Interferometer Sequence	78
7.2 Contrast	80
7.3 Multiple Interfering Paths	82
7.4 Measurement of the Earth's Rotation Rate	89
7.5 Vibration Compensation	94
8 Accelerometry and Gravity Gradiometry	97
8.1 Acceleration Measurements	97
8.2 Gravity Gradiometry	100
8.2.1 Ellipse Fitting	101
8.2.2 Gradiometer Performance	103
8.3 Mass Testing	104
9 Zero Dead Time Operation	108
9.1 The Dick Effect in Atomic Clocks	108
9.1.1 Example: the Microwave Fountain Clock	109
9.2 Zero Dead Time Atomic Clock	112
9.3 Experimental Demonstration	114
9.4 Zero Dead Time Inertial Measurements	116
10 Conclusion	120
10.1 Future Improvements	120
10.2 Future Measurements	122
A Fundamental Constants and Numerical Values	124

B Cesium Properties	125
C Laser Frequencies	126
Bibliography	128

List of Tables

2.1 Gyroscope performance comparison	19
A.1 Fundamental constants and numerical values	124
B.1 Cs properties	125

List of Figures

2.1	Sagnac effect	16
3.1	Cs energy levels	22
3.2	Raman transition level diagram	29
4.1	Phase contributions from multiple paths	34
4.2	Three-pulse interferometer sequence	41
4.3	Trajectories for launched atoms	46
4.4	Additional interfering loops due to imperfect pulse areas	48
5.1	Picture of experimental apparatus	50
5.2	Frame stack assembly	51
5.3	Cs lock schematic	52
5.4	Tapered amplifier module	54
5.5	Block diagram of the control system	56
5.6	Sensor with magnetic shield removed	58
5.7	Zerodur vacuum cell	59
5.8	Magnetic bias field coils and MOT coils	63
5.9	Inner and outer magnetic shields	64
6.1	Schematic of the experimental sequence	66
6.2	Raman beam generation schematic	69
6.3	Raman beam layout	69
6.4	Raman beam spectrum	71
6.5	Rabi frequency vs. retro-reflecting mirror position	72

6.6	Spatially varying Rabi frequency for different detunings	73
6.7	CCD image of the $F = 3$ and $F = 4$ atoms	75
6.8	Schematic of the detection system	75
6.9	Detection system SNR	77
7.1	Raman beam intensity profile	81
7.2	Atom temperature measurement	83
7.3	Multiple path interference dependence on relative amplitude	85
7.4	Multiple path interference dependence on relative phase	86
7.5	Multiple path contributions	87
7.6	Elimination of multiple path contributions	88
7.7	Projection of Earth rotation rate	90
7.8	Interferometer phase for Earth rotation rate measurement	92
7.9	Allan deviation of Earth rotation rate measurement	93
7.10	Gyroscope correlations	95
8.1	Accelerometer fringes	99
8.2	Ellipse fitting	102
8.3	Low noise interferometer ellipse	103
8.4	Schematic of mass test	104
8.5	Gravity gradiometer ellipse	105
8.6	Interferometer phases for mass test	107
9.1	ZDT pulse sequence	112
9.2	Clock random phase walk and ZDT	115
9.3	ZDT Allan deviation	117
9.4	Pulse sequence for continuous velocity measurement	118
10.1	Staggered launching sequence	123
C.1	Laser frequencies	127

Chapter 1

Introduction

1.1 Rotation Measurements

Precision rotation measurements are of great importance to a variety of applications, ranging from navigation to geophysics to tests of general relativity. Instruments capable of sensing rotations, commonly referred to as “gyroscopes”, typically rely on either conservation of angular momentum or the Sagnac effect to sense changes in orientation, and can measure either angular displacement or rotation rate depending on the specific implementation.

The first gyroscope was developed in 1852 by Foucault based on the Machine of Bohnenberger [1] for the purpose of measuring the Earth’s rotation rate. The apparatus consisted of a rapidly spinning disk with a heavy rim in a low friction gimbal mount. Once it is set in motion, the disk’s spin axis maintains its orientation due to conservation of angular momentum despite any motion of the gimbal platform. Over the next century, similar mechanical gyroscopes became increasingly common as navigational tools in ships. Since then, both practical and scientific interests have driven the development of more sensitive and accurate gyroscopes, giving rise to a variety of different gyroscope technologies including micro-electro-mechanical systems (MEMS), fiber optic gyroscopes, ring lasers, and, as described here, atom interferometers.

In the field of navigation, gyroscopes are used to measure and maintain one’s

orientation relative to a fixed reference frame. In inertial navigation, knowledge of one's position and orientation is determined without the aid of external references (e.g. GPS) by measuring accelerations (linear or rotational) of the moving reference frame. This requires gyroscopes and accelerometers with ultra-high precision and accuracy, as small errors in angular rate or acceleration can rapidly integrate up to large position errors in time.

In geophysics, fluctuations in the Earth rotation rate provide valuable information about the composition and dynamics of the Earth. Very sensitive portable gyroscopes could also provide local measurements of rotational effects due to seismic events, tectonic movements, and tidal effects.

Sensitive gyroscopes can also be used in fundamental tests of general relativity. Accurate measurements of the geodetic precession of a gyroscope in orbit would constrain any deviations from general relativity predicted by some other theories of gravity in the weak-field limit. Also, a measurement of the Lense-Thirring or frame-dragging effect due to the rotation of the Earth would provide the first direct evidence of gravito-magnetism decoupled from other relativistic gravitational effects [2].

These applications, as well as many others, would benefit greatly from the availability of a very sensitive, mobile gyroscope.

1.2 Atom Interferometry

The wave nature of matter is one of the fundamental concepts underlying the theory of quantum mechanics. The idea that massive particles exhibit wave-like properties with a wavelength determined by the particle's momentum was first proposed by de Broglie in 1924 [3]. Today, a variety of matter wave interferometry experiments are exploiting the wave nature of atoms for precision measurements and fundamental tests of quantum mechanics. There are many inherent advantages to using atom interferometers: they have extremely high sensitivities, their intrinsic calibration leads to excellent long-term stability, and their relative simplicity makes them a good candidate for cost effective mass production.

Interference in matter waves was first demonstrated in 1927 in a pair of electron beam diffraction experiments by Davisson and Germer [4] and by Thomson and Reid [5]. The first experiment demonstrating interference in atoms was performed by Ramsey in 1950 [6] using the separated oscillatory field method in a thermal atomic beam. While this experiment was very sensitive to the phase of the local oscillator driving the microwave transition, hence providing the basis for modern atomic clocks, the momentum recoil from the rf photons was too small to produce a significant spatial separation between the interfering paths, and it was therefore largely insensitive to any gravitational or inertial effects.

Gravitational and inertial effects in matter waves were first observed in 1975 through the gravitational phase shift in a neutron interferometer [7]. These effects were not observed in atom interferometers until the advent of laser cooling and trapping techniques, as well as parallel developments in atom optics, paved the way for a new generation of atom interferometers with spatially separated trajectories. The initial experimental demonstrations were performed by several groups in 1991, including a Young's double slit experiment with helium [8], a three-grating Mach-Zehnder type Sagnac interferometer with sodium [9], a Ramsey-Bordé type interferometer with calcium [10], and a three-pulse $\frac{\pi}{2} - \pi - \frac{\pi}{2}$ interferometer using two-photon stimulated Raman transitions [11].

Interferometric rotation measurements began with optical interferometers in the early 20th century, with the first rotation-induced interference experiment performed by Sagnac [12]. In 1925, Michelson and Gale measured the Earth's rotation using a large area (2010×1113 ft.) ring interferometer [13]. With the invention of the laser, the development of optical gyroscopes progressed rapidly, leading to the demonstration of the first ring laser gyroscope in 1963 [14], and the first fiber optic gyroscope in 1976 [15].

By then, the idea of using atom interferometers for rotation measurements had already been proposed by Altshuler and Frantz [16]. The Sagnac phase shift in matter-wave interferometers was calculated by Page [17] and by Anandan [18], and was experimentally demonstrated in a neutron interferometer in 1979 [19]. In 1988 Clauser

proposed several configurations for neutral atom interferometers for measuring gravitational and inertial effects [20]. Soon after, the Sagnac effect was demonstrated in neutral atoms [10, 21, 22], as well as in charged particles (electrons) [23]. Today, atom interferometers have demonstrated some of the most sensitive rotation rate measurements [24].

Atom interferometers are very versatile in that depending on their specific configuration and implementation, they can be used to measure a variety of inertial and gravitational effects, as well as different interactions between the atoms and external potentials. In recent years, in addition to precision rotation measurements, they have achieved great success in measuring gravitational accelerations [25], gravity gradients [26, 27], and fundamental constants such as Newton's gravitational constant G [28] and the fine structure constant α [29]. Recent proposals have been made to use atom interferometry for tests of general relativity [30, 31, 32], including tests of the equivalence principle [33], measurements of the curvature of space-time [34] and the frame-dragging effect [35], and also for the detection of gravitational waves [36, 37, 38].

1.3 Overview

The format of this dissertation is as follows. Chapter 2 presents the motivation behind developing an atom interferometer gyroscope by highlighting some of the applications of high sensitivity gyroscopes, and describing the existing technologies available for precision rotation measurements. Chapter 3 reviews some of the basics of atom-photon interactions and the two-level system in the context of laser cooling and trapping, as well as two-photon stimulated Raman transitions. Atom interferometer theory is discussed in chapter 4, including the calculation of differential phase shifts and the rotation sensitivity of different Raman pulse sequences. The mobile experimental apparatus is detailed in chapter 5, including the laser and vacuum systems. Chapter 6 discusses different aspects of the atom interferometry experiment, including the atomic state preparation and detection, and the Raman beam configuration. Chapter 7 presents the results of the rotation rate measurements, and discusses the

sensitivity and accuracy performance limits of the system. The next two chapters illustrate the flexibility of the apparatus by detailing modes of operation other than rotation measurement. In chapter 8, acceleration and gravity gradient measurements are discussed, and in chapter 9, a zero dead time technique for continuous phase monitoring in an atomic clock system is introduced, and its application to inertial sensing is discussed. Finally, chapter 10 concludes with a brief discussion of possible future improvements and measurements to be made with the apparatus.

Chapter 2

Gyroscopes

This chapter discusses some of the important applications for sensitive gyroscopes, including navigation and basic science. Different technologies used in precision rotation rate measurements are described and evaluated based on their relative performance. In particular, interferometric gyroscopes based on the Sagnac effect are discussed, and the phase sensitivities for both an optical and atomic interferometer are calculated.

2.1 Gyroscope Applications

This section outlines three of the primary applications of high sensitivity gyroscopes: inertial navigation, geophysics, and tests of general relativity.

2.1.1 Inertial Navigation

Navigation has always been one of the principle driving forces behind the development of sensitive gyroscopes. Today, the Global Positioning System (GPS) allows for very accurate navigation via communication with a constellation of orbiting satellites. However, GPS is not perfect, as the satellite signals may be blocked by structures or intentionally jammed. Therefore, the most demanding applications require very sensitive accelerometers and gyroscopes for inertial navigation.

In general, an inertial navigation system (INS) consists of three orthogonal gyroscopes for measuring and maintaining orientation, and three accelerometers for determining displacement along each axis. For an ultra-high precision INS, access to a gravity map or real-time measurement of the gravity gradient tensor is required for gravity compensation of the acceleration signal [39]. Atom interferometers are a good candidate for an INS since they can be configured as a gyroscope, accelerometer, or gravity gradiometer [40].

The sensitivities of INS accelerometers and gyroscopes are particularly important because a small error in angular rate or acceleration can lead to very large position errors in time. A bias error in the measured acceleration Δa , when integrated over some time T , leads to a position error of $\Delta x = \frac{1}{2}\Delta aT^2$. Likewise, a bias error in the rotation rate $\Delta\Omega$ leads to an angle error of $\Delta\theta = \Delta\Omega T$, giving a position error of $\Delta x \approx \Delta\Omega vT^2$.

Typical requirements for an inertial grade gyroscope are $< 0.001 \text{ deg}/\sqrt{\text{hr}}$ angle random walk, $< 0.01 \text{ deg/hr}$ bias stability, and 0.001% scale factor stability [41]. Current INS positional accuracy drifts are limited to $\sim 0.5 \text{ miles/hr}$ when unaided by GPS. The development of an INS based on atom interferometry aims to achieve drift rates of $< 5 \text{ m/hr}$ [42].

2.1.2 Geophysics

There are many important applications for atom interferometry in solid-earth geophysics, particularly in the areas of seismology, geodesy, and tectonophysics. Very sensitive gyroscopes may be used to monitor length of day fluctuations, which reflect the composition and dynamics of the Earth. A sensitive, portable gyroscope would be particularly useful in monitoring local rotations due to seismic events or tidal effects. These applications, along with others, are discussed below. For a more comprehensive review of the application of gyroscopes to geophysical studies, see, for example, [43].

Seismic Rotations

There is great interest in measuring the rotational component of seismic waves. The study of rotations is complementary to the study linear motions in understanding the propagation of seismic waves. Also, a better understanding of seismic rotations could reduce the vulnerability of buildings and structures to earthquakes and other seismic events.

The rotational component of seismic waves arises from the curl of the velocity field

$$\boldsymbol{\Omega} = \frac{1}{2} \nabla \times \mathbf{v}. \quad (2.1)$$

Precision rotation measurements can aid in determining the local phase velocity and propagation direction of seismic waves and help to constrain physical models [44]. Rotations are also sensitive to local variations in ground density and composition due to conversion between linear and circular polarizations at media boundaries [43]. A sensitive, mobile gyroscope or array of gyroscopes and accelerometers would benefit this type of seismic monitoring.

Rotations due to seismic events are generally in the range of $\Omega = 10^{-14} - 1$ rad/s, and cover a frequency span from 3 mHz to 10 Hz [45, 46]. In particular, intercontinental mantle (Love) waves that induce rotations about the local vertical occur at the 0.05 Hz level, as compared to microseismic background motions at 0.1 – 0.5 Hz [43].

Length of Day Fluctuations

In geodesy, precision measurements of the Earth rotation rate Ω_E are important in understanding the composition, rheology, and dynamics of the Earth's mantle. Changes in the orientation of the spin axis are referred to as polar motion, while changes in the angular velocity are reflected in length of day (LOD) fluctuations. Both effects are dominated by solar and lunar tides, which deform the Earth and affect its moment of inertia. Seasonal wind patterns, seismic events [47], and local geographical variations [48] can also contribute to polar motion and LOD fluctuations.

These effects represent small fractional changes in the Earth rotation rate, typically around $10^{-8} \Omega_E$. Space-based measurements, including Very Long Baseline

Interferometry (VLBI) [49] and Lunar Laser Ranging (LLR) have shown great sensitivity in determining LOD fluctuations, but are generally limited to time scales on the order of several hours to a day. Ground-based rotation rate measurements with finer time resolution would improve on existing knowledge of the Earth's rotation dynamics.

Other Tidal Effects

Besides affecting the global Earth rotation rate and polar motion, solar and lunar tides can exhibit local effects as well. Deformations of the Earth's surface lead to a change in the local vertical, which can be measured directly, or indirectly through the projection of Ω_E on the Sagnac area A with the interferometer axis acting as a tiltmeter. Displacements due to solar and lunar tides in solid earth can be up to 30 cm [50].

For lunar and solar Earth tides, the oscillation frequencies are at half the lunar day $\sim 25 \mu\text{Hz}$ [43]. Tidal effects dominate at the $10^{-8} \Omega_E$ level, as compared to other geophysical sources of vorticity at $10^{-8} - 10^{-9} \Omega_E$ [51], and general relativistic corrections at $10^{-10} \Omega_E$ [52].

2.1.3 General Relativity

Very sensitive gyroscopes can also provide fundamental tests of general relativity. Two of the effects of Einstein's theory of general relativity within experimental reach are the geodetic and Lense-Thirring effects. The geodetic effect refers to the effect of the curvature of space-time on the spin axis of a moving gyroscope. The Lense-Thirring or frame-dragging effect is due to the dragging of space-time by a massive rotating body [53].

The geodetic effect can be understood by an analogy in two dimensions. Consider a particle in a flat, two-dimensional space with some initial spin vector. In the absence of any torques, the spin direction will stay constant no matter what path the particle moves along. Now consider a particle on a sphere, initially positioned at the equator with its spin facing north. If this particle travels 90° east, then 90° north, then

90° back to its original position, then the spin direction will have rotated by 90° . Similarly, a particle orbiting the Earth will experience a precession of its spin axis, with the rotation given by

$$\boldsymbol{\Omega}_{GD} = \frac{3GM}{2c^2r^3}(\mathbf{r} \times \mathbf{v}), \quad (2.2)$$

where M is the mass of the Earth, and \mathbf{r} and \mathbf{v} are the position and velocity of the test mass.

The Lense-Thirring effect arises when a massive rotating body “drags” space-time around it, thereby affecting the spin of a nearby test body. The rotation induced by the Lense-Thirring effect is given by

$$\boldsymbol{\Omega}_{LT} = \frac{GI}{c^2} \frac{3(\boldsymbol{\omega} \cdot \mathbf{r})\mathbf{r} - \boldsymbol{\omega}r^2}{r^5}, \quad (2.3)$$

where \mathbf{r} is the position of the test body, I is Earth’s moment of inertia, and $\boldsymbol{\omega}$ represents the rotation of the Earth [54]. For a 642 km high polar orbit where the two effects are orthogonal, the precession rates for the geodetic and Lense-Thirring effects are 2.1×10^{-7} deg/h and 1.2×10^{-9} deg/h, respectively [55].

One ambitious attempt to measure both the geodetic and Lense-Thirring effects is the Gravity Probe B (GPB) experiment at Stanford. A series of superconducting gyroscopes were placed in a drag-free satellite in polar orbit around the Earth, and measured the induced rotations relative to a distant guide star. The flight mission has concluded successfully, and the initial data is consistent with general relativistic predictions at the 1% level [56].

The prospect of using an atom interferometer gyroscope to measure the Lense-Thirring effect has been discussed [20, 31, 57], and a satellite mission for mapping the Lense-Thirring effect close to the Earth using atom interferometry has been considered [35]. Additionally, there have been proposals to use atom interferometers in space to put an upper bound on the rotation rate of the universe [58].

2.2 Gyroscope Metrics

In this section, the most common parameters for characterizing gyroscope performance are introduced. The relative performances of different gyroscope technologies will be compared and discussed in subsequent sections using these metrics.

2.2.1 Angle Random Walk

The angle random walk (ARW) of a gyroscope, typically given in units of rad/s/ $\sqrt{\text{Hz}}$ (or deg/ $\sqrt{\text{hr}}$ in the field of navigation), is used to characterize the noise floor of the sensor. For rotation rate gyroscopes, the output has to be integrated to determine the total angular displacement, and any noise $\eta(t)$ on the rotation rate measurement is integrated to give the total angle error

$$\delta\theta(t) = \int_0^t \eta(\tau) d\tau. \quad (2.4)$$

If $\eta(\tau)$ is white noise, then this results in a random walk of the angular error. The standard deviation $\sigma_{\delta\theta}(t)$ of the angular error grows with the square root of the number of measurements $N = B \times T$, where B (Hz) is the bandwidth of the sensor and T (s) is the total integration time. If the standard deviation of the noise on the rotation rate measurement is given by σ_η , then

$$\sigma_{\delta\theta}(T) = \frac{\sigma_\eta \cdot T}{\sqrt{N}} = \frac{\sigma_\eta}{\sqrt{B}} \sqrt{T} = \text{ARW} \times \sqrt{T}, \quad (2.5)$$

where $\text{ARW} = \sigma_\eta / \sqrt{B}$ (rad/s/ $\sqrt{\text{Hz}}$).

Alternatively, the ARW can be thought of in terms of the power spectral density of the sensor noise. For pure white noise, the gyroscope output has a flat frequency response with a constant value σ_η^2/B (rad/s) $^2/\text{Hz}$. The ARW is simply given by the square root of this power spectral density.

2.2.2 Bias and Scale Factor Stability

The bias stability, given in units of rad/hr (or deg/hr), is a measure of the long-term accuracy of the gyroscope. Bias refers to an offset in the rotation rate, independent of the signal being measured. The bias stability is determined by monitoring the drift in the long-term average of the measured rotation rate, typically for a null signal. How long to average for each bias measurement, and over what time scales to track the bias instability is most readily determined by the Allan deviation of the rotation rate signal.

The Allan variance was originally developed to quantify the stability of clocks, but can be applied to any system to determine the noise as a function of the averaging time. In order to calculate the Allan variance, the sample data is broken up into N bins based on an integration time of τ . The Allan variance is then defined as

$$\sigma_y^2(\tau) = \frac{1}{2} \langle (y_{i+1} - y_i)^2 \rangle, \quad (2.6)$$

where y_i is the average measured value for the i th bin. The factor of $\frac{1}{2}$ is added to make the Allan variance be equal to the classical variance if y_i is an uncorrelated set. The Allan deviation $\sigma_y(\tau)$ is simply the square root of the Allan variance, and has the units of the quantity being measured, in this case rotation rate (rad/s).

For a system dominated by white noise, the Allan deviation decreases for a longer averaging time τ . As the size of the bins increase, the standard deviation of the bin averages should integrate down as $1/\sqrt{\tau}$. However, as τ gets large, the Allan deviation will begin increasing again as long-term drifts in the bias lead to a random walk in the rotation rate measurement. The minimum value of the Allan deviation is typically referred to as the bias stability.

In addition to ARW and bias stability, scale factor stability is often used to characterize drifts in the measurement of a constant rotation rate signal. This serves to determine the accuracy of the overall calibration of the instrument. For an atom interferometer, the scale factor stability depends only on the frequency stability of the Raman laser, the pointing of the Raman beam, the laser pulse timing, and knowledge of local gravity.

2.3 Gyroscope Technologies

There are two main types of rotation rate sensors: mechanical gyroscopes and analogous systems based on conservation of angular momentum, and interferometric gyroscopes based on the Sagnac effect. This section provides an overview of the different types of gyroscope technologies currently available.

2.3.1 Mechanical Gyroscopes

A conventional mechanical gyroscope consists of a flywheel spinning about its axis of symmetry, mounted in a gimbal so that its axis of rotation can turn freely. Conservation of angular momentum allows the flywheel to maintain its orientation regardless of the motion of the base. Measuring the deflection of the spin axis gives the total angular displacement of the platform. Alternatively, these types of mechanical systems can be configured as rate gyroscopes by adding a spring, in which case the deflection is proportional to the rotation rate. Because mechanical gyroscopes rely on moving parts, they are subject to friction and wear, which can affect their long-term stability. In addition, any defects in the flywheel lead to residual torques in the presence of gravity, which limits the accuracy of the gyroscope.

The most sensitive mechanical gyroscopes to date are the superconducting gyroscopes developed for the GPB experiment. A set of four precision machined 1.5 in. diameter quartz spheres, smoothed to within 40 atomic layers (0.1 ppm) of a perfect sphere, are coated with superconducting niobium and used as the flywheels. They are electrostatically levitated in a nano- g environment in a drag-free satellite. As each sphere spins, the lattice of superconducting nuclei spins with it while the surface electrons remain at rest, giving rise to a magnetic moment that is parallel to the spin axis of the sphere. This spin axis is read out by using a series of SQUID magnetometers. The GPB gyroscopes are able to achieve very good long-term accuracies in space because the residual gravitational torques tend to average out over the orbital motion of the satellite.

2.3.2 Interferometric Gyroscopes

Ring laser gyroscopes consist of a laser gain medium within a ring-shaped resonator. Light propagates along both directions of the loop where the frequency is restricted such that the perimeter is an integer multiple of the optical wavelength. Small rotations give rise to an effective path length difference through the Sagnac effect, as described in the next section, resulting in a frequency difference

$$\Delta\nu = \frac{4\Omega \cdot \mathbf{A}}{\lambda P}, \quad (2.7)$$

where \mathbf{A} is the enclosed area, P is the optical path length or perimeter of the ring laser, and λ is the wavelength in the absence of rotation [59]. The rotation rate Ω can be determined by measuring the beat frequency between the two counterpropagating modes of the ring laser. Currently the largest ring laser gyroscope in operation is UG1a in Christchurch, New Zealand. It was built 30 m underground in a former World War II bunker, and has a perimeter of 77.0 m and an area of 367 m² [60]. One issue with ring lasers is that they suffer from “lock-in” at very small rotation rates, whereby the two counter-rotating modes lock to the same frequency because of mode coupling due to backscatter. As a result, ring laser gyroscopes often rely on mechanical dither or multi-oscillator techniques to reduce this effect, or they are biased away from zero to avoid lock-in altogether [43].

Fiber optic gyroscopes also rely on the Sagnac effect, but measure the differential phase accrued along two different optical paths rather than a beat frequency between counterpropagating modes. The Sagnac phase shift due to rotations is given by

$$\Delta\phi = \frac{4\pi\Omega \cdot \mathbf{A}}{\lambda c}, \quad (2.8)$$

where, \mathbf{A} is the enclosed area and λ is the optical wavelength. Very large effective areas may be achieved by repeatedly coiling as much as 5 km of fiber. Fiber optic gyroscopes generally exhibit better rotation sensitivity than ring lasers, but suffer from greater bias and scale factor drifts.

Atom interferometers are analogous to fiber optic gyroscopes, except that optical

interference is replaced with matter wave interference. As with the fiber optic gyroscope, an incoming matter wave is coherently split between two spatially separated paths, and small rotations induce a differential Sagnac phase shift given by

$$\Delta\phi = \frac{2m}{\hbar} \boldsymbol{\Omega} \cdot \mathbf{A}, \quad (2.9)$$

where m is the mass of the atom, and \mathbf{A} is the enclosed area.

One of the principal advantages of atom interferometers is their large inherent rotation sensitivity. When comparing an atom interferometer and a fiber optic gyroscope with equal areas, the phase sensitivity scales as the ratio of the energies of the interfering particles, $mc^2/\hbar\omega$. For typical values of m and ω , this leads to a factor of $\sim 10^{11}$ improvement in the inherent phase sensitivity of an atom interferometer over an optical interferometer. In practice, however, fiber optic gyroscopes are able to achieve much larger areas than atom interferometers, as well as higher fluxes leading to better signal-to-noise performance, greatly reducing the advantage that atom interferometers have over their optical counterparts.

2.3.3 The Sagnac Effect

Interferometric gyroscopes rely on the Sagnac effect [12, 61] to measure angular velocity. The Sagnac effect is special-relativistic in nature [62], and leads to a phase shift proportional to the rotation rate in a closed-loop interferometer. In this section, the Sagnac phase shift due to a constant rotation in an optical interferometer is derived, and analyzed in the context of atom interferometers.

Consider a circular, closed-loop interferometer as shown in fig. 2.1. Light from a laser source is split by a beamsplitter at A along two paths, one clockwise and one counterclockwise. The light propagates along the two paths and interferes at a second beamsplitter located at B.

The time of travel for the two paths is given by

$$ct^\pm = \pi r \pm \Omega r t^\pm, \quad (2.10)$$

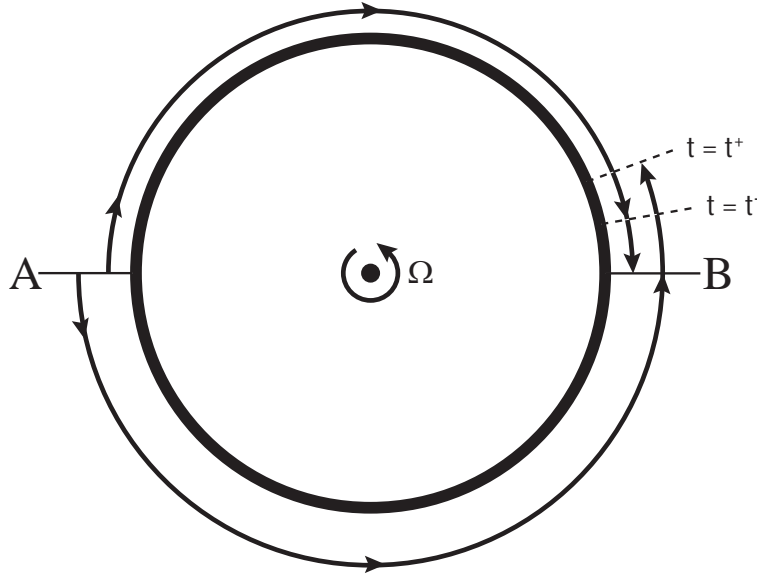


Figure 2.1: The Sagnac effect in a closed loop interferometer. A constant rotation changes the effective path lengths of the two arms of the interferometer, leading to a relative phase difference of $\Delta\phi = \frac{4\pi\Omega \cdot \mathbf{A}}{\lambda c}$ between the two paths.

where Ω represents the rate of rotation about the axis normal to the plane of the interferometer. The difference between the travel times of the two paths is therefore

$$\Delta t \equiv t^+ - t^- \approx \frac{2\Omega \cdot \mathbf{A}}{c^2}, \quad (2.11)$$

where \mathbf{A} represents the area vector of the closed loop. This corresponds to a phase difference of

$$\Delta\phi = \omega\Delta t = \frac{2\omega\Omega \cdot \mathbf{A}}{c^2} = \frac{4\pi\Omega \cdot \mathbf{A}}{\lambda c} \quad (2.12)$$

between the two paths of the interferometer.

In the case of an atom interferometer, the light is replaced by an atom, and the atomic wavepacket is split along two paths. The atom's classical velocity \mathbf{v} is substituted for the speed of light, and the de Broglie wavelength λ_{dB} replaces the optical wavelength, giving

$$\Delta\phi = \frac{2m\Omega \cdot \mathbf{A}}{\hbar}. \quad (2.13)$$

Another way of understanding this phase shift is to note that interference only occurs when the two contributing paths overlap both spatially and temporally at the end of the interferometer. In order for the two interfering wavepackets to arrive at B at the same time, they must originate from two different locations, separated by

$$\Delta\mathbf{x} = \mathbf{v}\Delta t = \frac{2\Omega \cdot \mathbf{A}}{v} \hat{\mathbf{v}}. \quad (2.14)$$

Modeling the initial atomic wavefunction as a momentum plane wave with $\mathbf{k} = \mathbf{p}/\hbar$ gives the relative phase shift

$$\Delta\phi = \mathbf{k} \cdot \Delta\mathbf{x} = \frac{2m\Omega \cdot \mathbf{A}}{\hbar}. \quad (2.15)$$

For an atom interferometer with a fixed area, the rotation sensitivity increases with greater mass and is independent of the atom's velocity. However, in this experiment, the area is not fixed. Photon momentum recoils are used to generate the spatial separation between the two paths, so the area enclosed is inversely proportional to the atomic mass, making the rotation sensitivity independent of atomic mass. Furthermore, if the atom position is restricted over a certain distance, the maximum possible enclosed area decreases with greater atom velocity, making it beneficial to have slower moving atoms.

2.3.4 Other Gyroscope Technologies

A comagnetometer gyroscope [63] is analogous to a conventional mechanical gyroscope, with an atom's nuclear spin serving as the flywheel. The comagnetometer consists of a dual species vapor cell with potassium (K) and helium-3 (${}^3\text{He}$) atoms. A magnetic bias field is applied to cancel the nuclear magnetization of the ${}^3\text{He}$, so that the K atoms operate in a low magnetic field, spin-exchange relaxation free regime. When the apparatus rotates, the ${}^3\text{He}$ nuclear spins lag behind the applied field, and precess out of the plane of the pump and probe beams. The vertical component of the nuclear magnetization causes the K spins to precess, and is measured by the probe beam.

MEMS gyroscopes are micromechanical vibrating systems that rely on the Coriolis effect to measure angular rotation rates. In general, a small test mass is driven to oscillate in a fixed plane at some frequency ω . Rotations induce a Coriolis acceleration $\mathbf{a}_C(t) = -2\boldsymbol{\Omega} \times \mathbf{v}(t)$, causing the test mass to oscillate out of the plane with the same frequency ω . The magnitude of the deflections is measured capacitively, and is proportional to the rotation rate.

Magnetohydrodynamic (MHD) gyroscopes consist of a conductive liquid in a ring or cylindrical shell, with a static magnetic field applied along the axis of symmetry. When the sensor rotates, the electrons in the fluid move relative to the magnetic field and experience a radial force $\mathbf{F} = -e\mathbf{v} \times \mathbf{B}$, generating a current in the fluid. The resulting electric potential across the fluid channel is proportional to the rotation rate.

There are also other types of gyroscopes that rely on the Sagnac effect. A hybrid light-matter-wave interferometer uses ultraslow light propagating in an ultracold gas to measure rotations [64]. In a superfluid gyroscope [65], a cylindrical container with a dividing wall with a Josephson junction is filled with superfluid helium. Because the circulation around any closed path in a superfluid is quantized, small rotations of the cylinder induce a large backflow through the aperture, with a velocity $v_{ap} = -2\boldsymbol{\Omega} \cdot \mathbf{A}/l_{ap}$ proportional to the rotation rate. This expression is analogous to the Sagnac phase shift in an interferometer, as the phase gradient in the superfluid is given by the local velocity.

2.3.5 Gyroscope Performance Comparison

As discussed in section 2.2, the performance of a gyroscope is typically characterized by two main values: the ARW and the bias stability. A comparison of the relative performances of the different gyroscopes discussed in the previous section in terms of these parameters is shown in table 2.1.

MEMS sensors are simple, inexpensive, and very compact, making them useful for a variety of commercial applications such as automotive roll sensors, but are not sensitive enough for more demanding applications. MHD sensors are also compact

	Short-term sensitivity (deg/ $\sqrt{\text{hr}}$)	Stability (deg/hr)
MEMS [66, 67]	0.2	31
MHD (ATA) [68]	8.7×10^{-4}	2.1×10^{-2}
GPB	—	10^{-11}
Superfluid [69]	4.8×10^{-4}	1.2×10^{-4} in 1 day
Comagnetometer [63]	1.7×10^{-3}	4×10^{-2}
Fiber optic gyro (Honeywell) [70]	8×10^{-5}	3×10^{-4}
Ring laser gyro (367.5m^2) [71]	4.8×10^{-8}	7.2×10^{-7} at 10^3 s
Atomic beam [24, 72]	2.1×10^{-6}	7×10^{-5} at 10^4 s
This work (current)	8.1×10^{-3}	$< 6.6 \times 10^{-3}$
This work (expected)	1.1×10^{-4}	—
This work (future)	2.1×10^{-5}	—

Table 2.1: Comparison of relative gyroscope performances.

and robust, and have good high frequency response, making them useful for monitoring angular jitter above 1 Hz. The most sensitive commercial fiber optic and ring laser gyroscopes operate at the $0.1 \text{ mdeg}/\sqrt{\text{hr}}$ level, and are typically used for guidance and navigation systems. They are also resistant to high accelerations, making them ideal for strap down systems. Scientific grade ring laser gyroscopes such as UG1a have demonstrated sensitivities of up to $50 \text{ ndeg}/\sqrt{\text{hr}}$, but they are very large (367.5 m^2) and extremely sensitive to environmental factors such as temperature and atmospheric pressure. The GPB gyroscopes, which are angle sensors rather than rate sensors, exhibit tremendous long-term stabilities in low- g environments, but are extremely expensive and subject to gravitational torques that can limit their accuracy. A 2 m atomic beam interferometer has demonstrated a sensitivity of $2 \mu\text{deg}/\sqrt{\text{hr}}$. However, because its phase sensitivity $\Delta\phi = 2\Omega k_{eff}L^2/v$ scales quadratically with its length L , the performance would suffer greatly if the size were to be reduced for mobile applications.

The current short-term sensitivity of the atom interferometer presented in this dissertation is based on an observed shot-to-shot rms phase noise of 221 mrad. The measured sensitivity and stability are both limited by the high frequency vibration

noise of the sensor platform. The expected value for the short-term sensitivity represents the anticipated shot noise limited performance of the atom interferometer given the current values for the detected atom number (5×10^6) and fringe contrast (30%). The future value is based on a factor of 10 improvement in the detected atom number that could be achieved with better state preparation, and an improved interferometer fringe contrast of 50%.

Chapter 3

Laser Manipulation of Atoms

One of the key innovations that have enabled very sensitive atom interferometry was the development of laser cooling and trapping in the early 1990s. These techniques provide a dense, robust source of cold atoms, leading to increased inertial and gravitational sensitivity through longer interrogation times, higher interferometer fringe contrast, and larger numbers of atoms contributing to the interferometer signal. Atom-photon interactions can also be used to directly manipulate atomic trajectories in light-pulse atom interferometry, as well as for detecting the output of the interferometer by measuring the final distribution of atomic states. This chapter reviews some of the basics of two-level system dynamics, and highlights important concepts in laser cooling and trapping. In addition, two-photon stimulated Raman transitions are discussed.

3.1 Atomic Structure of Cesium

The Cesium (Cs) atom is used exclusively in the work described in this dissertation. A simplified energy level diagram is shown in fig. 3.1. The ground state atomic structure of Cs, like all other alkali-metal atoms, consists of a closed inner shell plus a single valence electron in an S-shell. There are two hyperfine ground states, the $6^2S_{1/2}$ $F = 3$ and $F = 4$ levels, corresponding to different spin states of the electron and separated by exactly 9.192631770 GHz. Here, $F = I + J$ represents the total angular

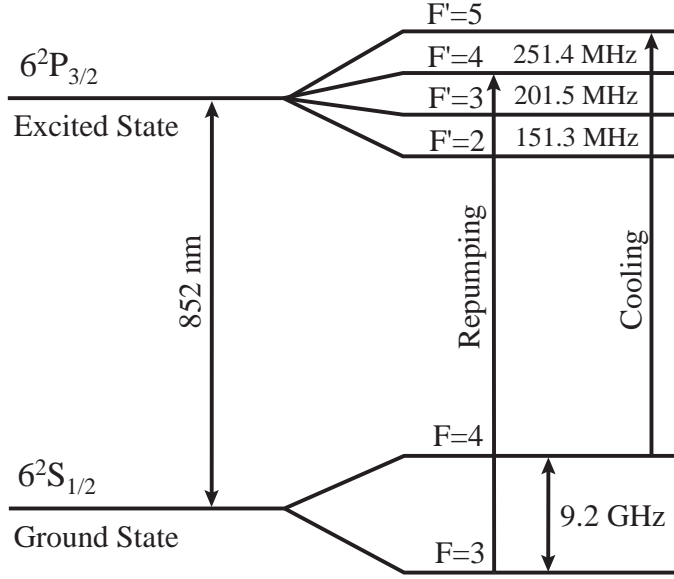


Figure 3.1: Simplified energy level diagram for the Cs D_2 -line.

momentum. For Cs, the nuclear angular momentum is $I = 7/2$, and the electron angular momentum $J = L + S$ is given by the sum of the orbital angular momentum and spin. Each hyperfine level is further split into $2F + 1$ Zeeman m_F sub-levels in the presence of a magnetic field. The $F = 3, m_F = 0$ and $F = 4, m_F = 0$ sub-levels are the principal states used in this atom interferometry experiment because of their first-order insensitivity to magnetic fields.

The two lowest excited states in Cs are the $6^2P_{1/2}$ and the $6^2P_{3/2}$ states. The transitions from the ground states to these excited states are referred to as the D_1 and D_2 lines, respectively. The D_2 line at 852 nm is the transition used for laser cooling and trapping. The $6^2P_{3/2}$ state consists of four levels, $F' = 2$, $F' = 3$, $F' = 4$, and $F' = 5$, where the prime denotes an excited state. When combined with angular momentum selection rules, this leads to the formation of closed cycling transitions that can be exploited for the efficient cooling and trapping of atoms. For example, an atom initially in $F = 4, m_F = +4$ driven to $F' = 5, m_F = +5$ with circularly polarized light necessarily decays back down to $F = 4, m_F = +4$. In practice, imperfect polarizations and off-resonant couplings to other states can lead to some

atoms being driven out of the cycling transition into dark states that do not interact with the driving field, requiring the addition of a repumping frequency that pumps these atoms back into the cycling transition.

3.2 Two-Level System Dynamics

While a real atom has many different energy levels, if it is driven close to resonance about a closed transition, then it can often be approximated as a simple two-level system. In this section, the dynamics of a two-level atom in an optical field are analyzed, ignoring the effects of spontaneous emission and treating the driving field as a classical field.

The Hamiltonian for a two-level atom subject to an electric field \mathbf{E} is given by

$$\hat{H} = \hbar\omega_e|e\rangle\langle e| + \hbar\omega_g|g\rangle\langle g| - \mathbf{d} \cdot \mathbf{E}, \quad (3.1)$$

where $\hbar\omega_e$ and $\hbar\omega_g$ represent the internal energy levels of the excited and ground states, and \mathbf{d} is the electric dipole moment of the atom. For a fixed driving frequency, the applied electric field is given by

$$\mathbf{E} = \mathbf{E}_0 \cos(\omega t + \phi). \quad (3.2)$$

The dipole interaction gives rise to an off-diagonal coupling term $\hbar\Omega_{eg}$, where the Rabi frequency

$$\Omega_{eg} \equiv \frac{\langle e | \mathbf{d} \cdot \mathbf{E} | g \rangle}{\hbar} \quad (3.3)$$

represents the frequency of Rabi oscillations between the excited and ground states for a resonant interaction ($\omega = \omega_e - \omega_g \equiv \omega_{eg}$).

The time-dependent Schrödinger equation may be solved for this Hamiltonian by transforming coordinates and applying the rotating wave approximation, as detailed in [73]. The time-evolution of the ground state and excited state amplitudes is given

by

$$c_e(t_0 + \tau) = e^{-i\delta\tau/2} \left\{ c_e(t_0) \left[\cos\left(\frac{\Omega_r\tau}{2}\right) - i \cos\theta \sin\left(\frac{\Omega_r\tau}{2}\right) \right] + c_g(t_0) e^{-i(\delta t_0 + \phi)} \left[-i \sin\theta \sin\left(\frac{\Omega_r\tau}{2}\right) \right] \right\} \quad (3.4)$$

$$c_g(t_0 + \tau) = e^{i\delta\tau/2} \left\{ c_e(t_0) e^{i(\delta t_0 + \phi)} \left[-i \sin\theta \sin\left(\frac{\Omega_r\tau}{2}\right) \right] + c_g(t_0) \left[\cos\left(\frac{\Omega_r\tau}{2}\right) + i \cos\theta \sin\left(\frac{\Omega_r\tau}{2}\right) \right] \right\}, \quad (3.5)$$

where

$$\begin{aligned} \delta &\equiv \omega - \omega_{eg} \\ \Omega_r &\equiv \sqrt{|\Omega_{eg}|^2 + \delta^2} \\ \sin\theta &= \Omega_{eg}/\Omega_r \\ \cos\theta &= -\delta/\Omega_r. \end{aligned} \quad (3.6)$$

Note that the phase of the final state amplitudes depends on the local phase ϕ of the driving field. The probability of being found in the excited state oscillates at the effective Rabi frequency Ω_r , with the contrast depending on the detuning δ . In the special case of resonant excitation where $\delta = 0$, the probability of an atom initially prepared in the ground state being found in the excited state becomes

$$P_e(\tau) = \frac{1}{2}[1 - \cos(\Omega_{eg}\tau)]. \quad (3.7)$$

If the atom is driven by a resonant field for a time τ such that $\Omega_{eg}\tau = \pi$, then it is transferred to the excited state with a probability of 100%. This condition is referred to as a π -pulse. Similarly, if the atom is driven by a pulse of duration $\Omega_{eg}\tau = \frac{\pi}{2}$, then it will put the atom into an equal coherent superposition of the ground and excited states, and is referred to as a $\frac{\pi}{2}$ -pulse.

In addition, the interaction between the atom and light field shifts the ground and

excited state energy levels by

$$\Delta E_g = -\Delta E_e = \frac{\hbar\Omega_{eg}^2}{4\delta} \quad (3.8)$$

in the limit of large detuning. This energy level shift, called the ac Stark shift, is only present when the driving field is on.

3.3 Laser Cooling

When an atom is driven into the excited state, it absorbs a photon from the driving field, resulting in a small momentum recoil. Laser cooling relies on this momentum transfer between the atom and the electric field through the absorption and emission of photons to decelerate the atom. This requires both a quantum treatment of the driving field and the inclusion of the effects of spontaneous emission. This is most readily accomplished by using a density matrix approach and solving the optical Bloch equations. For a detailed treatment, see [74, 75]; the important results will be summarized in the following sections.

3.3.1 Doppler Cooling

In a two-level system, the excited state population decays at a rate given by the natural linewidth $\gamma = 1/\tau$, where τ is the excited state lifetime. In the presence of an optical field, the probability that an atom absorbs a photon depends on how close the frequency is to the atomic resonance, with the excitation rate depending on the relative populations in the ground and excited states. In steady state, the decay rate due to spontaneous emission equals the excitation rate, and the total scattering rate of photons from the light field is given by

$$\gamma_p = \gamma\rho_{ee} = \frac{s_0\gamma/2}{1 + s_0 + (2\delta/\gamma)^2}, \quad (3.9)$$

where ρ_{ee} is the excited state population and $s_0 \equiv 2|\Omega_{eg}|^2/\gamma^2 = I/I_{sat}$ is the saturation parameter. For Cs, the saturation intensity is $I_{sat} \simeq 1.1 \text{ mW/cm}^2$.

When an atom is excited by a laser field, it absorbs a photon and receives a momentum recoil of $\hbar k$ along the propagation direction of the laser. If the atom subsequently decays back into the ground state through spontaneous emission, it will experience another momentum recoil of $\hbar k$, but in a random direction. As a result, multiple absorption-spontaneous emission cycles lead to a net momentum kick along the propagation direction of the light field. For an atom at rest, this leads to a scattering force given by

$$F_{sp} = \hbar k \gamma_p = \frac{\hbar k s_0 \gamma / 2}{1 + s_0 + (2\delta/\gamma)^2}. \quad (3.10)$$

However, if the momentum of an atom changes, the effective detuning changes due to the Doppler shift, giving rise to a velocity dependent force. If the light is detuned slightly to the red of the atomic resonance ($\delta < 0$), then atoms traveling toward the light will see the light shifted closer to resonance and scatter more photons opposing the atom's motion, while atoms traveling away from the light will see the light shifted further away from resonance and scatter less photons. With two counterpropagating beams, the atom experiences an average damping force $F_{av} = -\beta v$, with the damping coefficient given by

$$\beta = -\hbar k^2 \frac{8s_0(\delta/\gamma)}{(1 + (2\delta/\gamma)^2)^2}. \quad (3.11)$$

This viscous damping is referred to as optical molasses, and may be generalized to three spatial dimensions with the addition of similar counterpropagating beams along the other two axes.

Doppler cooling is limited by the random nature of spontaneous emission. An atom starting at rest in an optical molasses will continue to absorb and spontaneously emit photons, leading to a diffusive random walk in space. This heating process competes with molasses cooling at low temperatures [76], giving a Doppler cooling temperature limit of

$$T_D = \frac{\hbar \gamma}{2k_B}. \quad (3.12)$$

For Cs, $T_D \approx 125 \mu\text{K}$.

3.3.2 Sub-Doppler Cooling

Atoms can be cooled beyond the Doppler limit by utilizing polarization gradients [77]. Counterpropagating light with either crossed-circular ($\sigma^+ - \sigma^-$) or crossed-linear ($\text{lin} \perp \text{lin}$) polarizations can be used, although they rely on different mechanisms to cool atoms. Here, only the $\sigma^+ - \sigma^-$ case will be considered.

Crossed-circular polarization produces a standing wave of linearly polarized light, with the polarization axis rotating in space with a spatial periodicity of $\lambda/2$. For a constant linear polarization, the steady-state ground state population distribution is symmetric about $m_F = 0$. As the atoms move across the standing wave, they experience a rotation of the quantization axis defined by the optical field. If this process is non-adiabatic, then it alters the ground state distribution asymmetrically depending on which direction the atom is traveling. For example, an atom moving toward the σ^+ light is more likely to be in $m_F = +1$ than $m_F = -1$, making it more likely to scatter a σ^+ photon than a σ^- photon. This gives an additional damping force allowing atoms to cool beyond the Doppler limit. The temperature limit of polarization gradient cooling is a few photon recoils, which, for Cs, is typically $\sim 2 \mu\text{K}$.

3.4 Magneto-Optical Trap

While an optical molasses can cool atoms efficiently, it does not trap the atoms. Even at very low velocities, the atoms continue to scatter photons in random directions, and eventually diffuse out of the laser beams. The atoms can be trapped by adding a magnetic field gradient to the molasses, which results in a position-dependent restoring force that allows for confinement of the atoms.

Here, a $J_g = 0 \rightarrow J_e = 1$ transition is considered, although the following arguments may be naturally extended to transitions with more sub-levels. σ^+ and σ^- polarized light couple the ground state to the $m_F = +1$ and $m_F = -1$ excited levels, respectively. A one-dimensional optical molasses is formed by two counterpropagating beams with polarizations σ^+ and σ^- . Applying a linear magnetic field gradient

shifts the excited levels in such a way that the $m_F = +1$ level is shifted closer to resonance on one side, while the $m_F = -1$ level is shifted closer on the other side. As a result, the atom preferentially scatters either σ^+ or σ^- light depending on its position due to the difference in detunings, and tends to recoil toward the center of the trap.

3.5 Atomic Fountain

The performance of atom interferometers generally scales with some power of the interrogation time T . Launching atoms along a ballistic trajectory from the bottom of a vacuum chamber doubles the interrogation time as compared to releasing atoms from a MOT at the top, allowing for increased interferometer sensitivity. Such an atomic fountain was first demonstrated by Kasevich et. al. [78].

The basic operating principle behind the atomic fountain is a moving molasses. Consider a one-dimensional optical molasses. If the two beams are detuned by $\pm\delta\omega$, the blue detuned beam will be closer to resonance and impart more radiation pressure, accelerating the atoms along that direction. The atoms will continue to accelerate until they attain a velocity $\mathbf{k} \cdot \mathbf{v} = \delta\omega$, at which point the Doppler shift cancels out the differential detuning, resulting in a regular optical molasses in the moving frame. Atoms accelerated in an atomic fountain can be simultaneously cooled in much the same way as a conventional optical molasses. This leads to narrow velocity distributions despite large mean velocities.

3.6 Two-Photon Stimulated Raman Transitions

In this experiment, two-photon stimulated Raman transitions [79, 80] are used for coherent manipulation of the atomic wavepackets. Raman pulses couple the two hyperfine ground levels with two optical frequencies, resulting in large momentum recoils and finer spatial phase resolution. A detailed discussion may be found in [73].

Consider a three-level system as shown in fig. 3.2. The two hyperfine ground state levels $|g\rangle$ and $|e\rangle$ are coupled to an intermediate level $|i\rangle$ via two optical fields with

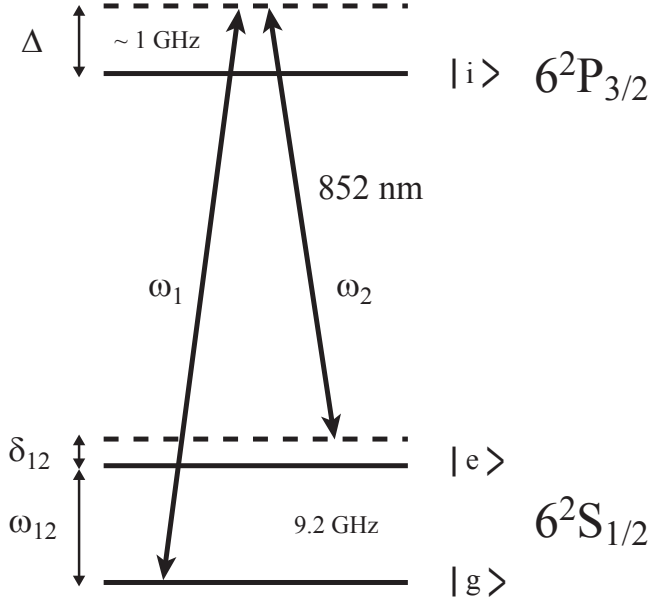


Figure 3.2: Energy level diagram for two-photon stimulated Raman transitions.

frequencies ω_1 and ω_2 . The combined electric field of the two coupling fields is

$$\mathbf{E} = \mathbf{E}_1 \cos(\mathbf{k}_1 \cdot \mathbf{x} - \omega_1 t + \phi_1) + \mathbf{E}_2 \cos(\mathbf{k}_2 \cdot \mathbf{x} - \omega_2 t + \phi_2). \quad (3.13)$$

The Hamiltonian for the three-level system is given by

$$\hat{H} = \frac{\mathbf{p}^2}{2m} + \hbar\omega_g|g\rangle\langle g| + \hbar\omega_i|i\rangle\langle i| + \hbar\omega_e|e\rangle\langle e| - \mathbf{d} \cdot \mathbf{E}, \quad (3.14)$$

where, once again, spontaneous emission has been ignored. For a large single photon detuning Δ , the intermediate level may be adiabatically eliminated. The resulting Hamiltonian, given in the spinor representation for $|e, \mathbf{p} + \hbar\mathbf{k}_{eff}\rangle$ and $|g, \mathbf{p}\rangle$ is

$$\hat{H} = \hbar \begin{pmatrix} \Omega_e^{AC} & \frac{\Omega_{eff}}{2} e^{-i(\delta_{12}t + \phi_{eff})} \\ \frac{\Omega_{eff}}{2} e^{i(\delta_{12}t + \phi_{eff})} & \Omega_g^{AC} \end{pmatrix}, \quad (3.15)$$

where

$$\begin{aligned}
\Omega_e^{AC} &\equiv \frac{|\Omega_e|^2}{4\Delta} \\
\Omega_g^{AC} &\equiv \frac{|\Omega_g|^2}{4\Delta} \\
\delta_{12} &\equiv (\omega_1 - \omega_2) - \left(\omega_{eg} + \frac{\mathbf{p} \cdot \mathbf{k}_{eff}}{m} + \frac{\hbar |\mathbf{k}_{eff}|^2}{2m} \right) \\
\Omega_e &\equiv -\frac{\langle i | \mathbf{d} \cdot \mathbf{E}_2 | e \rangle}{\hbar} \\
\Omega_g &\equiv -\frac{\langle i | \mathbf{d} \cdot \mathbf{E}_1 | g \rangle}{\hbar} \\
\Omega_{eff}^* \Omega_g &\equiv \frac{\Omega_e^* \Omega_g}{2\Delta} e^{i\phi_{eff}} \\
\phi_{eff} &\equiv \phi_1 - \phi_2 \\
\mathbf{k}_{eff} &\equiv \mathbf{k}_1 - \mathbf{k}_2.
\end{aligned} \tag{3.16}$$

The solutions for the Hamiltonian are

$$\begin{aligned}
c_{e,\mathbf{p}+\hbar\mathbf{k}_{eff}}(t_0 + \tau) &= e^{-i(\Omega_e^{AC} + \Omega_g^{AC})\tau/2} e^{-i\delta_{12}\tau/2} \\
&\quad \left\{ c_{e,\mathbf{p}+\hbar\mathbf{k}_{eff}}(t_0) \left[\cos\left(\frac{\Omega'_r\tau}{2}\right) - i \cos\Theta \sin\left(\frac{\Omega'_r\tau}{2}\right) \right] \right. \\
&\quad \left. + c_{g,\mathbf{p}}(t_0) e^{-i(\delta_{12}t_0 + \phi_{eff})} \left[-i \sin\Theta \sin\left(\frac{\Omega'_r\tau}{2}\right) \right] \right\} \\
c_{g,\mathbf{p}}(t_0 + \tau) &= e^{-i(\Omega_e^{AC} + \Omega_g^{AC})\tau/2} e^{i\delta_{12}\tau/2} \\
&\quad \left\{ c_{e,\mathbf{p}+\hbar\mathbf{k}_{eff}}(t_0) e^{i(\delta_{12}t_0 + \phi_{eff})} \left[-i \sin\Theta \sin\left(\frac{\Omega'_r\tau}{2}\right) \right] \right. \\
&\quad \left. + c_{g,\mathbf{p}}(t_0) \left[\cos\left(\frac{\Omega'_r\tau}{2}\right) + i \cos\Theta \sin\left(\frac{\Omega'_r\tau}{2}\right) \right] \right\},
\end{aligned} \tag{3.17}$$

where

$$\begin{aligned}
\Omega'_r &\equiv \sqrt{|\Omega_{eff}|^2 + (\delta_{12} - \delta^{AC})^2} \\
\sin\Theta &= \Omega_{eff}/\Omega'_r \\
\cos\Theta &= -(\delta_{12} - \delta^{AC})/\Omega'_r.
\end{aligned} \tag{3.18}$$

The differential Stark shift $\delta^{AC} \equiv \delta_e^{AC} - \delta_g^{AC}$ can be tuned to zero by adjusting the relative intensities of the two driving fields. (This is important if both frequencies come from the same source to cancel the effect of common laser intensity fluctuations.) When the driving field is on resonance ($\delta_{12} = 0$), the atom Rabi flops between the ground and excited states as in the two-level system, with an effective Rabi frequency Ω_{eff} .

When an atom is driven from the ground state to the excited state by a two-photon stimulated Raman transition, it absorbs a photon with frequency ω_1 , and undergoes stimulated emission of a photon with frequency ω_2 . If both frequencies have well defined wave vectors \mathbf{k}_1 and \mathbf{k}_2 , then this results in a fixed momentum recoil of $\hbar\mathbf{k}_{eff}$. For counterpropagating frequencies ($\mathbf{k}_1 \approx -\mathbf{k}_2$), the atom experiences a maximal momentum recoil of $\sim 2\hbar\mathbf{k}_1$, which is important in this experiment for obtaining the largest enclosed area possible for the Sagnac loop. For the two-photon Raman transition in Cs, this momentum recoil is $v_{rec} = \hbar k_{eff}/m \approx 7.1$ mm/s.

When an atom is driven from the excited state back down to the ground state, it receives a momentum kick of $-\hbar\mathbf{k}_{eff}$. Therefore, an atom initially in the ground state with momentum \mathbf{p} will always have momentum \mathbf{p} whenever it is in the ground state, and $\mathbf{p} + \hbar\mathbf{k}_{eff}$ when it is in the excited state, resulting in two possible atomic states $|g, \mathbf{p}\rangle$ and $|e, \mathbf{p} + \hbar\mathbf{k}_{eff}\rangle$. Thus, the two-photon Raman transitions effectively couple the atom's momentum with its internal electronic spin state.

The sensitivity of atom interferometers generally scales with the inverse of the spatial periodicity of the phase of the driving field (\mathbf{k}_{eff}). For a microwave transition at 9.2 GHz, $k_{microwave} \approx 1.9 \times 10^2$ m⁻¹, whereas $k_{eff} \approx 1.5 \times 10^7$ m⁻¹ for a corresponding two-photon Raman transition, resulting in a factor of 10^5 improvement in sensitivity. Because the driving frequency has to be phase coherent with the transition over the total interrogation time, this also puts stringent requirements on the frequency stability of the driving field. For typical interrogation times of ~ 200 ms, this implies Hz-level stability of the driving field. Fortunately, this can be achieved using two-photon Raman transitions since *only* the difference frequency, and not the absolute frequency, needs to be stable at the Hz-level.

Chapter 4

Atom Interferometer Theory

In this experiment, gravitational and inertial effects are monitored by measuring the difference in phases accrued along two arms of an atom interferometer. This chapter outlines the path integral method for computing this differential phase shift. Contributions from the atom's free propagation, laser interactions, and spatial separations are described in detail, and the relationship between inertial forces and phase is derived. Differential phase shifts are calculated for a $\frac{\pi}{2} - \pi - \frac{\pi}{2}$ and $\frac{\pi}{2} - \pi - \pi - \frac{\pi}{2}$ interferometer pulse sequence, and their sensitivities to rotations are discussed.

4.1 Differential Phase Shifts

The observable in these atom interferometry experiments is the final atomic populations in the different possible output states. The relative population reflects the differential phase accrued between the interfering paths, from which the effects of inertial or gravitational forces may be inferred. Any differential forces or interactions experienced by the atom lead to a difference in the phase evolution of the atomic wavepacket between the interfering paths, resulting in a shift in the interference pattern.

Since the desired information (i.e. acceleration, rotation rate, or gravity gradient) is derived from measurements of the differential phase, it is critical to determine the dependence of the atomic phase shift on these quantities. The exact relationship

between differential phase and the relevant physical quantities depends on the specific interferometer pulse sequence. The details of the atomic phase shift calculation using the path integral method are outlined in the following sections, and the differential phase shifts for the three-pulse acceleration-sensitive and four-pulse rotation-sensitive interferometer sequences are derived.

4.2 The Path Integral Approach

Path integrals provide a powerful tool for calculating differential phase shifts in an atom interferometer. In the classical limit where the spatial separation between interfering paths is macroscopic, the path integral approach is particularly appropriate as it reduces the phase calculation to an integral along the trajectory of a classical particle. A detailed description of Feynman's path integral approach [81] applied to atom interferometry is presented in [82], with some of the important details outlined below.

In classical dynamics, the “action” for an arbitrary path Γ from $\mathbf{r}_a = \mathbf{r}(t_a)$ to $\mathbf{r}_b = \mathbf{r}(t_b)$ is given by

$$S_\Gamma = \int_{t_a}^{t_b} L[\mathbf{r}(t), \dot{\mathbf{r}}(t)] dt, \quad (4.1)$$

where the Lagrangian is defined as $L[\mathbf{r}(t), \dot{\mathbf{r}}(t)] = \frac{1}{2}m\dot{\mathbf{r}}^2 - V(\mathbf{r})$. Under the principle of least action, the actual path of a classical particle is the one which minimizes the value of S_Γ , and the corresponding classical action is denoted by $S_{cl} \equiv S_{cl}(\mathbf{r}_a, t_a, \mathbf{r}_b, t_b)$.

In quantum mechanics, the time evolution of the atomic wavefunction $\psi(\mathbf{r}, t)$ is determined by the quantum propagator K

$$\psi(\mathbf{r}_b, t_b) = \int K(\mathbf{r}_b, t_b, \mathbf{r}_a, t_a) \psi(\mathbf{r}_a, t_a) d\mathbf{r}_a. \quad (4.2)$$

The quantum propagator can be viewed as the transition amplitude for a particle initially at (\mathbf{r}_a, t_a) to end up at (\mathbf{r}_b, t_b) . Under Feynman's path integral formalism, the quantum propagator represents the sum of the amplitudes of all possible paths from (\mathbf{r}_a, t_a) to (\mathbf{r}_b, t_b) . The phase factor for the contribution from a particular path

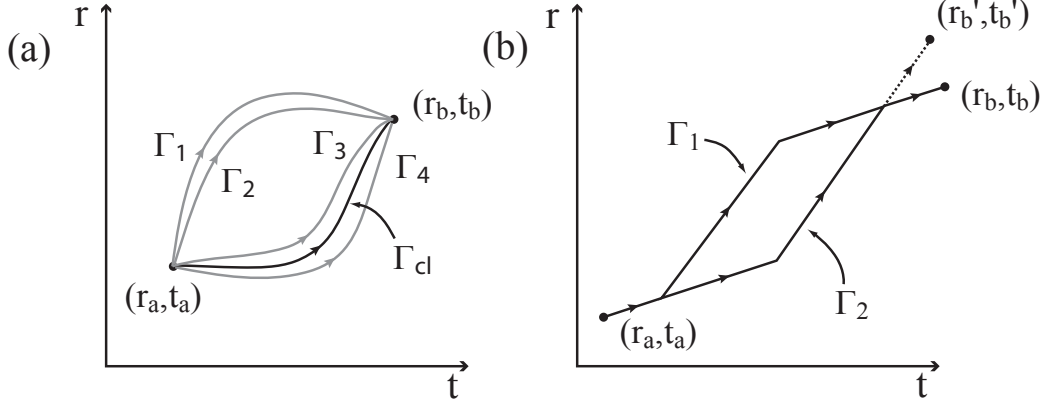


Figure 4.1: All classical and non-classical paths contribute to the phase evolution between two points in space-time. (a) Multiple paths connecting the two space-time point (\mathbf{r}_a, t_a) and (\mathbf{r}_b, t_b) are shown. The classical path Γ_{cl} represents the path for which the action is extremal, and therefore the phase contributions from neighboring paths Γ_3 and Γ_4 add constructively. Away from Γ_{cl} , the phase oscillates rapidly between adjacent paths, and contributions from neighboring paths such as Γ_1 and Γ_2 destructively interfere. (b) Two classical paths Γ_1 and Γ_2 connect (\mathbf{r}_a, t_a) to (\mathbf{r}_b, t_b) . The final phase is the sum of the contributions from both paths.

Γ is simply $\frac{1}{\hbar}$ times the action evaluated over that path, so that

$$K(\mathbf{r}_b, t_b, \mathbf{r}_a, t_a) = \mathcal{N} \sum_{\Gamma} e^{iS_{\Gamma}/\hbar} = \int_a^b \mathcal{D}\mathbf{r}(t) e^{iS_{\Gamma}/\hbar}, \quad (4.3)$$

where \mathcal{N} is some normalization constant.

In the classical limit where $\delta S_{\Gamma} \gg \hbar$, the phase factor S_{Γ}/\hbar oscillates rapidly across adjacent paths everywhere except in the vicinity of the classical path Γ_{cl} . As a result, contributions from paths away from Γ_{cl} tend to destructively interfere, while those close to Γ_{cl} add together constructively, as shown in fig. 4.1a.

The specific form of the quantum propagator depends on the spatial dependence of the potential $V(\mathbf{r})$. For uniform rotations and linear gravity gradients, the Lagrangian is quadratic in $\mathbf{r}(t)$. Evaluating the integral in (4.3) for a quadratic Lagrangian gives

a quantum propagator of the form

$$K(\mathbf{r}_b, t_b, \mathbf{r}_a, t_a) = F(t_b, t_a) e^{\frac{i}{\hbar} S_{cl}(\mathbf{r}_b, t_b, \mathbf{r}_a, t_a)}, \quad (4.4)$$

where $F(t_b, t_a)$ is a functional integral independent of \mathbf{r}_a and \mathbf{r}_b .

Taking the initial wavefunction of the atom to be a momentum plane wave state and evaluating the final wavefunction using the quantum propagator for a quadratic Lagrangian gives

$$\psi(\mathbf{r}_b, t_b) \propto e^{\frac{i}{\hbar} S_{cl}(\mathbf{r}_b, t_b, \mathbf{r}_a, t_a)} \psi(\mathbf{r}_a, t_a). \quad (4.5)$$

Thus, the phase evolution of the wavefunction is simply given by S_{cl}/\hbar .

If the classical action is written in terms of the momentum \mathbf{p} and the total energy of the atom E , then the expression for the phase becomes

$$\begin{aligned} S_{\Gamma}/\hbar &= \frac{1}{\hbar} \int_{\Gamma} \frac{1}{2} m \mathbf{v}^2 - V(\mathbf{r}) dt \\ &= \frac{1}{\hbar} \int_{\Gamma} \frac{\mathbf{p}^2}{2m} - (E - \frac{\mathbf{p}^2}{2m}) dt \\ &= \frac{1}{\hbar} \int_{\Gamma} (\frac{\mathbf{p}^2}{m} - E) dt \\ &= \int_{\Gamma} \frac{\mathbf{p} \cdot d\mathbf{x}}{\hbar} - \frac{E}{\hbar} dt. \end{aligned} \quad (4.6)$$

The first part of the integral represents the phase due to the spatial propagation of the atom in terms of its de Broglie wavelength $\lambda_{dB} = h/\mathbf{p}$. The second part gives the phase evolution of the atomic wavefunction due to its total energy. In this way both the spatial propagation and atomic energy contribute to the full path integral phase.

In the case where multiple classical paths exist between (\mathbf{r}_a, t_a) and (\mathbf{r}_b, t_b) , the final wavefunction is proportional to the sum of the phasors from each of the contributing paths. Consider a basic atom interferometer with two interfering arms, as shown in fig. 4.1b. The atom is initially described by some wavefunction $\psi(\mathbf{r}_a, t_a)$. The atomic wavepacket is split and allowed to propagate along two distinct paths Γ_1 and Γ_2 , then recombined such that the atom exits the interferometer in one of two

states, $\psi_1(\mathbf{r}_b, t_b)$ or $\psi_2(\mathbf{r}'_b, t'_b)$. For one of the output ports,

$$\begin{aligned}\psi_1(\mathbf{r}_b, t_b) &= \mathcal{N}(e^{\frac{i}{\hbar}S_{\Gamma_1}} + e^{\frac{i}{\hbar}S_{\Gamma_2}})\psi(\mathbf{r}_a, t_a) \\ &= \mathcal{N}(e^{i\phi_0} + e^{i(\phi_0 + \Delta\phi)})\psi(\mathbf{r}_a, t_a) \\ &= \mathcal{N}e^{i\phi_0}(1 + e^{i\Delta\phi})\psi(\mathbf{r}_a, t_a)\end{aligned}\quad (4.7)$$

where $\Delta\phi = (S_{\Gamma_2} - S_{\Gamma_1})/\hbar$ represents the differential phase between the two interfering paths. The probability of detecting the atom in state 1 is therefore

$$\begin{aligned}|\psi_1(\mathbf{r}_b, t_b)|^2 &= \mathcal{N}^2(1 + e^{i\Delta\phi})(1 + e^{-i\Delta\phi})|\psi(\mathbf{r}_a, t_a)|^2 \\ &= \frac{1}{2}(1 + \cos(\Delta\phi)),\end{aligned}\quad (4.8)$$

and oscillates as a function of the differential phase $\Delta\phi$.

While the full path integral provides a way of calculating the exact phase shift for the atomic wavefunction, it is often convenient and more intuitive to break up the total phase contribution into several different components. In particular, treating the discrete atom-laser interactions independently from the free propagation of the atom simplifies the calculation. Also, phase shifts due to spatial offsets in the initial/final positions of the interfering paths can be treated independently, so that

$$\Delta\phi_{total} = \Delta\phi_{prop} + \Delta\phi_{sep} + \Delta\phi_{laser}. \quad (4.9)$$

Each of these phase contributions will be discussed in detail in the following sections.

4.2.1 Propagation Phase

The propagation phase ϕ_{prop} represents the phase shift picked up by the atom due to its free propagation between Raman pulses. ϕ_{prop} is given by the path integral along its classical trajectory (excluding the laser interactions), and depends on both the atom's spatial propagation and its total energy, including the internal energy due to its electronic spin state. In most atom interferometers, time-symmetric pulse sequences ensure that both paths spend the same amount of time in each of the spin

states, and the differential phase contribution from the atom's internal energy can be ignored.

In the presence of a constant gravitational field only (i.e. no rotations or gravity gradients), the differential phase for a time-symmetric pulse sequence is given by the integral

$$\Delta\phi_{prop} = \frac{1}{\hbar} \oint L[\mathbf{r}(t), \dot{\mathbf{r}}(t)] dt \quad (4.10)$$

evaluated along the closed loop formed by the classical trajectories of the atom. In the presence of rotations or gravity gradients, the two paths may no longer form a closed loop; however, for small rotations or gravity gradients it is often useful to employ a perturbative approach, in which $\Delta\phi_{prop}$ is still evaluated along the unperturbed trajectory, and any phase shift resulting from a deviation from a closed loop is evaluated as part of $\Delta\phi_{sep}$.

4.2.2 Separation Phase

In the simplest case of a constant gravitational potential with no rotations, the two arms of the interferometer form a closed loop and overlap perfectly at the output. In general, however, the interferometer does not necessarily form a closed loop, and the two paths may need to originate from different points in space in order to overlap and interfere at the end of the interferometer sequence.

If the initial atomic wavefunction is modeled as a plane wave with momentum \mathbf{p} , then the differential phase contribution due to a spatial separation $\Delta\mathbf{r}$ in the origins of the interfering paths is given by

$$\Delta\phi_{sep} = \frac{\mathbf{p} \cdot \Delta\mathbf{r}}{\hbar} = \frac{2\pi\Delta x}{\lambda_{dB}}. \quad (4.11)$$

The relative phase between the two starting points is simply the ratio of the spatial separation along the initial momentum to the de Broglie wavelength of the atom. It is analogous to the phase shift $\Delta\phi = 2\pi\frac{\Delta x}{\lambda}$ due to a path length difference Δx in an optical interferometer with wavelength λ .

4.2.3 Laser Interaction Phase

The laser interaction phase ϕ_{laser} arises from the atom's interactions with the optical field driving the two-photon stimulated Raman transitions. When an oscillating field drives an atomic transition from one state to another, the atom picks up the local phase of the driving field. A more detailed treatment, including the effects of finite detuning is given in [73]. Here, it is assumed that the laser fields are infinitely thin, such that the duration for which the optical field is pulsed on is negligibly small. For a treatment including the effects of finite pulse duration, see, for example [83].

In the limit of a short, intense pulse on resonance, the time evolution of the ground and excited state amplitudes is given by

$$\begin{aligned} c_g(t + \tau) &= \cos\left(\frac{\Omega_\gamma\tau}{2}\right)c_g(t) - i\sin\left(\frac{\Omega_\gamma\tau}{2}\right)e^{i\phi}c_e(t) \\ c_e(t + \tau) &= -i\sin\left(\frac{\Omega_\gamma\tau}{2}\right)e^{-i\phi}c_g(t) + \cos\left(\frac{\Omega_\gamma\tau}{2}\right)c_e(t), \end{aligned} \quad (4.12)$$

where ϕ is the local phase of the applied electric field. The atomic wavefunction picks up a phase factor of $e^{-i\phi}$ when it is driven from the ground state up to the excited state, and a factor $e^{+i\phi}$ when it is driven back down into the ground state. In the absence of an applied field, the state amplitudes remain unchanged.

The differential phase between the two paths depends on the specific Raman pulse sequence chosen for the atom interferometer. A typical interferometer sequence consists of a series of $\frac{\pi}{2}$ - and π -pulses, so named because the “pulse areas” defined as $\Omega_\gamma\tau$ are $\frac{\pi}{2}$ and π respectively for pulses of length τ . A $\frac{\pi}{2}$ -pulse acts to put an atom initially in either the ground state or excited state into an equal, coherent superposition of the two states, while a π -pulse inverts the atomic state.

Here, the differential phase due to a classic three-pulse $\frac{\pi}{2} - \pi - \frac{\pi}{2}$ sequence is calculated as an example. Assume that the atom is initially prepared in the ground state at time $t = 0$ such that $c_g(0) = 1$ and $c_e(0) = 0$. After a $\frac{\pi}{2}$ -pulse at time $t = 0$,

the state amplitudes are

$$\begin{aligned} c_g\left(\frac{\tau}{2}\right) &= \frac{1}{\sqrt{2}} \\ c_e\left(\frac{\tau}{2}\right) &= -\frac{i}{\sqrt{2}}e^{-i\phi_1}, \end{aligned} \quad (4.13)$$

where ϕ_1 is the laser phase for pulse 1.

The atom then propagates for a time T , during which the state amplitudes remain unchanged. At time $t = T + \frac{\tau}{2}$ a π -pulse is applied, giving

$$\begin{aligned} c_g\left(T + \frac{3\tau}{2}\right) &= -\frac{1}{\sqrt{2}}e^{-i\phi_1+i\phi_2} \\ c_e\left(T + \frac{3\tau}{2}\right) &= -\frac{i}{\sqrt{2}}e^{-i\phi_2}. \end{aligned} \quad (4.14)$$

After another free-propagation period of T , a final $\frac{\pi}{2}$ -pulse is applied, closing the interferometer. The final state amplitudes are given by

$$\begin{aligned} c_g(2T + 2\tau) &= -\frac{1}{2}e^{-i\phi_1+i\phi_2} - \frac{1}{2}e^{-i\phi_2+i\phi_3} \\ c_e(2T + 2\tau) &= \frac{i}{2}e^{-i\phi_1+i\phi_2-i\phi_3} - \frac{i}{2}e^{-i\phi_2}. \end{aligned} \quad (4.15)$$

The final ground and excited state populations therefore oscillate as

$$\begin{aligned} |c_g(2T + 2\tau)|^2 &= \frac{1}{2}[1 + \cos(\Delta\phi_{laser})] \\ |c_e(2T + 2\tau)|^2 &= \frac{1}{2}[1 - \cos(\Delta\phi_{laser})], \end{aligned} \quad (4.16)$$

where $\Delta\phi_{laser} = \phi_1 - 2\phi_2 + \phi_3$. This is the total differential phase shift due to the atom's interactions with the three Raman laser pulses in a standard $\frac{\pi}{2} - \pi - \frac{\pi}{2}$ interferometer. The phase shift for a four-pulse $\frac{\pi}{2} - \pi - \pi - \frac{\pi}{2}$ sequence can be computed in a similar fashion, and is given by $\Delta\phi_{laser} = \phi_1 - 2\phi_2 + 2\phi_3 - \phi_4$.

4.3 Interferometer Pulse Sequences

The relationship between the differential phase shift and inertial and gravitational forces depends on the specific interferometer pulse sequence being used. The timing and particular combination of pulses used determines the atomic trajectories, and also controls how the laser phase is sampled by the interfering paths. In the following two sections, the three-pulse $\frac{\pi}{2} - \pi - \frac{\pi}{2}$ and four-pulse $\frac{\pi}{2} - \pi - \pi - \frac{\pi}{2}$ sequences are analyzed, and the effects of constant linear accelerations and rotations on the differential phase are calculated.

4.3.1 Three-Pulse Accelerometer: $\frac{\pi}{2} - \pi - \frac{\pi}{2}$

Consider a three-pulse $\frac{\pi}{2} - \pi - \frac{\pi}{2}$ interferometer sequence as shown in fig. 4.2. The Raman beams are oriented horizontally with a separation time T between pulses, and the atom is released with a small initial horizontal velocity. Tracing out the classical trajectories shows that this sequence resembles a traditional Mach-Zehnder interferometer. For constant acceleration and no rotations, $\Delta\phi_{prop} = \Delta\phi_{sep} = 0$, and the differential phase arises solely from the atom's interactions with the lasers $\Delta\phi_{laser}$. The local laser phase that the atoms experience at the i th pulse is given by

$$\phi_i = \phi_i^0 + \mathbf{k}_{eff} \cdot \mathbf{x}_i - \omega t_i, \quad (4.17)$$

where the arbitrary laser phase ϕ_i^0 is the initial phase of the laser at some reference point, and $\omega = \omega_1 - \omega_2$ is the difference between the two laser frequencies. The differential laser interaction phase is therefore

$$\begin{aligned} \Delta\phi_{laser} &= \phi_1 - 2\phi_2 + \phi_3 \\ &= (\phi_1^0 + \mathbf{k}_{eff} \cdot \mathbf{x}_1 - \omega(0)) - 2(\phi_2^0 + \mathbf{k}_{eff} \cdot \mathbf{x}_2 - \omega(T)) \\ &\quad + (\phi_3^0 + \mathbf{k}_{eff} \cdot \mathbf{x}_3 - \omega(2T)) \\ &= \mathbf{k}_{eff} \cdot (\mathbf{x}_1 - 2\mathbf{x}_2 + \mathbf{x}_3) + \Delta\phi^0, \end{aligned} \quad (4.18)$$

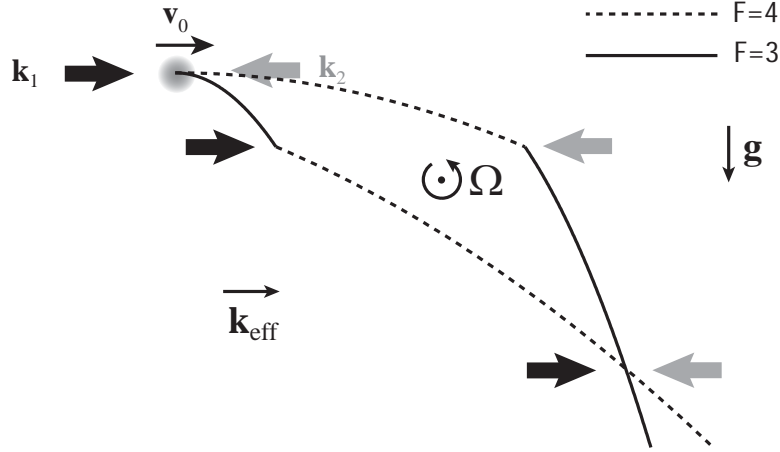


Figure 4.2: Atomic trajectory for a three-pulse $\frac{\pi}{2} - \pi - \frac{\pi}{2}$ interferometer sequence. The atom initially starts in the $F = 3$ hyperfine ground state, with a small horizontal velocity \mathbf{v}_0 to break the symmetry between two pairs of counterpropagating Raman beams. The first $\frac{\pi}{2}$ -pulse puts the atom in an equal superposition of the two states, with the $F = 4$ state receiving an additional momentum kick of $\hbar \mathbf{k}_{\text{eff}} = \hbar(\mathbf{k}_1 - \mathbf{k}_2)$. The π -pulse then reverses the atomic state and momentum, and the final $\frac{\pi}{2}$ -pulse overlaps the two paths to produce interference.

where $\Delta\phi^0 \equiv \phi_1^0 - 2\phi_2^0 + \phi_3^0$. For a constant acceleration \mathbf{g} , the position of the atom is given by the classical expression

$$\mathbf{x}_i = \mathbf{x}_0 + \mathbf{v}_0 t_i + \frac{1}{2} \mathbf{g} t_i^2, \quad (4.19)$$

giving

$$\Delta\phi_{\text{laser}} = \mathbf{k}_{\text{eff}} \cdot \mathbf{g} T^2 + \Delta\phi^0. \quad (4.20)$$

For constant accelerations, the differential phase shift is proportional to the component of acceleration along \mathbf{k}_{eff} .

The differential phase shift resulting from rotations can be calculated using a variety of methods. Here, the Sagnac phase shift due to small rotations in a three-pulse interferometer is calculated three different ways. The first approach is to use perturbation theory, in which the effect of the Coriolis force is integrated along the atom's unperturbed trajectory, leading to the Sagnac phase showing up in $\Delta\phi_{\text{prop}}$. In

the second approach, the exact path is calculated in the rotating coordinate frame, and the resulting corrections to $\Delta\phi_{laser}$ give rise to the Sagnac phase shift. In the third approach, the rotation of the lasers in the lab frame lead to a difference in the momentum recoil between the two paths, and all three contributions including the separation phase $\Delta\phi_{sep}$ must be taken into account to determine the Sagnac phase shift.

The perturbative approach to calculating the phase shift due to a constant rotation involves evaluating $\Delta\phi_{prop}$ in the rotating coordinate frame, in which the velocity of the atom is modified by $\mathbf{v} \rightarrow \mathbf{v} + \boldsymbol{\Omega} \times \mathbf{r}$. The Lagrangian in the rotating coordinate frame is given by

$$\begin{aligned} L' &= \frac{1}{2}m(\mathbf{v} + \boldsymbol{\Omega} \times \mathbf{r})^2 \\ &= \frac{1}{2}mv^2 + m\boldsymbol{\Omega} \cdot (\mathbf{r} \times \mathbf{v}) + O(\Omega^2). \end{aligned} \quad (4.21)$$

Ω is assumed to be small such that $\Omega T \ll 1$, and higher order terms due to, for example, centrifugal acceleration may be ignored. The classical action can be calculated along the unperturbed trajectory using the Coriolis term as a perturbation

$$\begin{aligned} \Delta\phi'_{prop} &= \frac{1}{\hbar} \oint (L' - L_0) dt \\ &= \frac{1}{\hbar} \oint m\boldsymbol{\Omega} \cdot (\mathbf{r} \times \mathbf{v}) dt \\ &= \frac{m\boldsymbol{\Omega}}{\hbar} \cdot \oint \mathbf{r} \times d\mathbf{r} \\ &= \frac{2m}{\hbar} \boldsymbol{\Omega} \cdot \mathbf{A}. \end{aligned} \quad (4.22)$$

This gives the Sagnac phase shift previously shown in (2.13).

Alternatively, the Sagnac phase shift can be derived by using the exact trajectory of the atom in the rotating coordinate frame and calculating the laser interaction phase $\Delta\phi_{laser}$. The atom in the rotating frame experiences an additional Coriolis

acceleration $\mathbf{a}_{Cor} = -2\boldsymbol{\Omega} \times \mathbf{v}$. Integrating and solving for position gives

$$\mathbf{x}_i \approx \mathbf{x}_0 + \mathbf{v}_0 t_i + \frac{1}{2} \mathbf{g} t_i^2 - \boldsymbol{\Omega} \times \left(\mathbf{v}_0 t_i^2 + \mathbf{g} \frac{t_i^3}{3} \right) \quad (4.23)$$

to first order in $\boldsymbol{\Omega}$. Calculating the laser interaction phase given the exact path gives

$$\begin{aligned} \Delta\phi_{laser} &= \mathbf{k}_{eff} \cdot (\mathbf{x}_1 - 2\mathbf{x}_2 + \mathbf{x}_3)T^2 + \Delta\phi^0 \\ &\approx \mathbf{k}_{eff} \cdot \mathbf{g} T^2 - \underbrace{2\mathbf{k}_{eff} \cdot (\boldsymbol{\Omega} \times \mathbf{v}_0) T^2 - 2\mathbf{k}_{eff} \cdot (\boldsymbol{\Omega} \times \mathbf{g}) T^3}_{= \frac{2m}{\hbar} \boldsymbol{\Omega} \cdot \mathbf{A}} + \Delta\phi^0. \end{aligned} \quad (4.24)$$

Again, the differential phase is modified by the Sagnac phase shift.

Yet another approach is to observe the atom in the inertial frame, and evaluate the effect of the rotating Raman laser beams. Imagine that the rotation is centered around the middle pulse at $t = 0$, such that \mathbf{k}_{eff} for the first and third pulses are rotated by an angle $\pm\Omega T$, so that

$$\begin{aligned} \mathbf{k}'_{eff}(t_1) &\simeq \mathbf{k}_{eff} - \boldsymbol{\Omega} \times \mathbf{k}_{eff} T \\ \mathbf{k}'_{eff}(t_2) &\simeq \mathbf{k}_{eff} \\ \mathbf{k}'_{eff}(t_3) &\simeq \mathbf{k}_{eff} + \boldsymbol{\Omega} \times \mathbf{k}_{eff} T. \end{aligned} \quad (4.25)$$

The path deflected by the first Raman pulse gets an additional momentum kick of $-\hbar(\boldsymbol{\Omega} \times \mathbf{k}_{eff})T$, which leads to a spatial separation of $\Delta\mathbf{x} = -2\frac{\hbar}{m}(\boldsymbol{\Omega} \times \mathbf{k}_{eff})T^2$. In order for the two paths to overlap at the interferometer output, the initial positions of the two paths must be separated by this amount, giving a relative phase shift of

$$\Delta\phi_{sep} = 2\mathbf{k}_{eff} \cdot (\boldsymbol{\Omega} \times \mathbf{v}_0)T^2. \quad (4.26)$$

In the inertial frame, rotations also lead to a Doppler shift in the laser frequencies, which changes the laser phase $\phi_i = \mathbf{k}_{eff} \cdot \mathbf{x} - \omega t + \phi_i^0$ that the atom observes at each Raman pulse. The Doppler shift arises from the motion of the laser source relative

to the inertial atoms, and is given by

$$\Delta\omega(t_i) \approx \mathbf{k}_{eff} \cdot \mathbf{v}_i = \mathbf{k}_{eff} \cdot [\boldsymbol{\Omega} \times (\mathbf{x}_i - \mathbf{x}_2)], \quad (4.27)$$

giving rise to an additional laser phase

$$\begin{aligned} \Delta\phi_{laser} &= \phi_1 - 2\phi_2 + \phi_3 \\ &= -\mathbf{k}_{eff} \cdot [\boldsymbol{\Omega} \times (\mathbf{x}_1 - \mathbf{x}_2)](-T) - \mathbf{k}_{eff} \cdot [\boldsymbol{\Omega} \times (\mathbf{x}_3 - \mathbf{x}_2)](T) \\ &= -2\mathbf{k}_{eff} \cdot [\boldsymbol{\Omega} \times (\mathbf{v}_0 + \mathbf{g}T)]T^2. \end{aligned} \quad (4.28)$$

Finally, evaluating the propagation phase in the inertial frame gives

$$\begin{aligned} \Delta\phi_{prop} &= \frac{1}{\hbar} \left(\int_1 L_1 dt - \int_2 L_2 dt \right) \\ &= -2\mathbf{k}_{eff} \cdot (\boldsymbol{\Omega} \times \mathbf{v}_0)T^2. \end{aligned} \quad (4.29)$$

Summing the three contributions gives the usual Sagnac phase shift

$$\Delta\phi_{total} = -2\mathbf{k}_{eff} \cdot [\boldsymbol{\Omega} \times (\mathbf{v}_0 + \mathbf{g}T)]T^2 = \frac{2m}{\hbar}\boldsymbol{\Omega} \cdot \mathbf{A}. \quad (4.30)$$

In the presence of both a constant gravitational acceleration and rotation, there is an additional phase shift due to the changing direction of \mathbf{g} . In the rotating coordinate frame,

$$\mathbf{g}(t) = \mathbf{g}(t_0) - \int_{t_0}^t \boldsymbol{\Omega} \times \mathbf{g} dt \quad (4.31)$$

$$\mathbf{x}(t) \approx \mathbf{x}_0 + \mathbf{v}_0 t + \frac{1}{2}\mathbf{g}_0 t^2 - \frac{1}{6}(\boldsymbol{\Omega} \times \mathbf{g}_0) t^3 \quad (4.32)$$

for $\Omega T \ll 1$. The position picks up a term cubic in t , which, in general, will not cancel out for a three-pulse sequence. Evaluating the laser interaction phase gives

$$\begin{aligned} \Delta\phi_{laser} &= \mathbf{k}_{eff} \cdot (\mathbf{x}_1 - 2\mathbf{x}_2 + \mathbf{x}_3)T^2 + \Delta\phi^0 \\ &= \mathbf{k}_{eff} \cdot \mathbf{g}_0 T^2 - \mathbf{k}_{eff} \cdot (\boldsymbol{\Omega} \times \mathbf{g}_0) T^3 + \Delta\phi^0. \end{aligned} \quad (4.33)$$

The time-dependent acceleration leads to an additional phase shift cubic in T . Including both the phase shift due to the Sagnac effect and the changing projection of \mathbf{g} , the total phase shift is

$$\Delta\phi = \mathbf{k}_{eff} \cdot \mathbf{g}T^2 + \frac{2m}{\hbar}\boldsymbol{\Omega} \cdot \mathbf{A} - \mathbf{k}_{eff} \cdot (\boldsymbol{\Omega} \times \mathbf{g})T^3 + \Delta\phi^0. \quad (4.34)$$

It is important to note that this additional term $-\mathbf{k}_{eff} \cdot (\boldsymbol{\Omega} \times \mathbf{g})T^3$ only arises if the measured reference frame is rotating relative to \mathbf{g} . If only Earth rotation $\boldsymbol{\Omega}_E$ is considered, then this term disappears because \mathbf{g} rotates along with the rotating reference frame. Therefore, this term only applies to platform rotations independent of Earth rotation that are much faster than $\boldsymbol{\Omega}_E$.

The expression given in (4.34) is valid only if the linear acceleration and rotation of the sensor are constant throughout the entire interferometer sequence. Because the interferometer is actually sampling the atom position at discrete times, the differential phase is really a measure of the mean velocity of the atoms between the Raman laser pulses. In most atom interferometry experiments, it is the average acceleration or rotation that is of interest, so the source of the differential phase shift is assumed to take on the form of a constant acceleration or rotation, and any deviations due to contributions from high frequency accelerations are incorporated into $\Delta\phi^0$ and treated as noise.

The sensitivity of an atom interferometer increases with the interaction time T . To make the most efficient use of a limited size vacuum cell, atoms are collected at the bottom and launched upwards, as opposed to just dropping them from rest. As a result, the atoms follow a trajectory similar to the one shown in fig. 4.3a. For a three-pulse sequence, this forms a “figure 8” geometry. Because the paths cross in the middle, the areas on either side have opposite sign, and therefore the total enclosed area goes to zero. This interferometer configuration therefore has no Sagnac phase shift, although it may still exhibit rotation sensitivity through the \mathbf{g} -projection term.

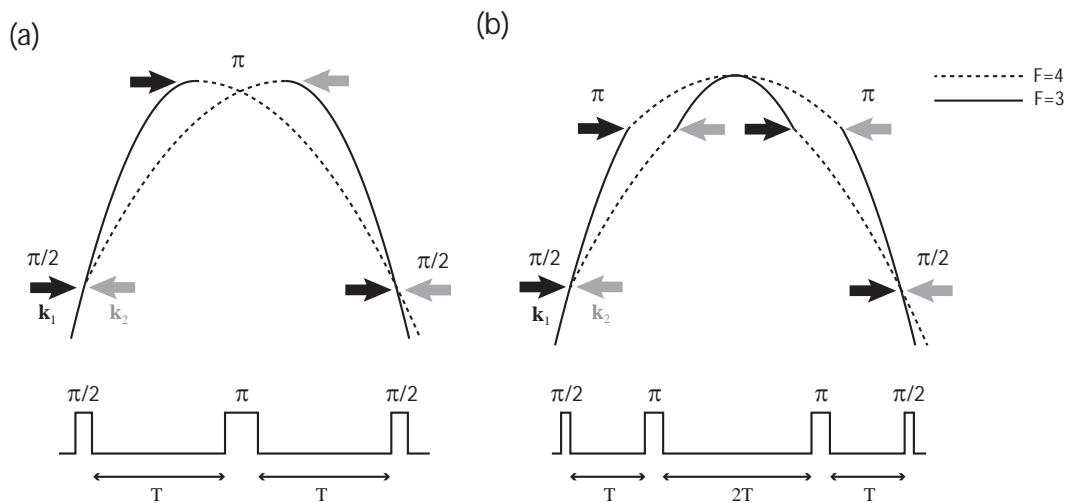


Figure 4.3: Atomic trajectories for interferometers with vertically launched atoms. (a) The three-pulse $\frac{\pi}{2} - \pi - \frac{\pi}{2}$ sequence forms a “figure 8” with two loops of equal area. Because the two paths cross, the areas have opposite sign and the total Sagnac phase shift is zero. (b) In the four-pulse $\frac{\pi}{2} - \pi - \pi - \frac{\pi}{2}$ sequence, the two paths overlap but do not cross. The areas of the two loops maintain the same sign and therefore add together, increasing the rotational sensitivity of the interferometer.

4.3.2 Four-Pulse Gyroscope: $\frac{\pi}{2} - \pi - \pi - \frac{\pi}{2}$

The rotational sensitivity of a launched atom interferometer can be maximized by employing a four-pulse $\frac{\pi}{2} - \pi - \pi - \frac{\pi}{2}$ interferometer sequence, with time T between the first and second pulses, time $2T$ between the second and third pulses, and time T between the third and final pulses. This leads to the atomic trajectory shown in fig. 4.3b. The two paths overlap but do not cross each other, so that the areas of the two loops have the same sign and add constructively to the rotational Sagnac shift.

The differential phase shift for the four-pulse sequence is

$$\Delta\phi = \frac{2m}{\hbar}\boldsymbol{\Omega} \cdot \mathbf{A} + 2\mathbf{k}_{eff} \cdot (\boldsymbol{\Omega} \times \mathbf{g})T^3 + \Delta\phi^0. \quad (4.35)$$

Note that the four-pulse sequence is insensitive to constant accelerations [20, 84], as the $\mathbf{k}_{eff} \cdot \mathbf{g}T^2$ term cancels out. This is because the phase shift for the four-pulse sequence is essentially the difference of two consecutive three-pulse interferometer sequences

$$\Delta\phi = (\phi_1 - 2\phi_2 + \phi_i) - (\phi_i - 2\phi_3 + \phi_4). \quad (4.36)$$

In this case \mathbf{k}_{eff} and \mathbf{g} are constant, but $\mathbf{k}_{eff} \cdot (\boldsymbol{\Omega} \times \mathbf{v})$ reverses sign, so the acceleration terms cancel while the Sagnac terms add.

One of the drawbacks of the four-pulse sequence is that imperfect π -pulses can lead to stimulated echo processes, in which additional closed loops besides the main interferometer loop contribute to the interferometer output. These extra loops have different acceleration and rotation sensitivities as compared to the main interferometer loop, which alters the relationship between rotation rate and the detected phase. In the four-pulse interferometer, the spurious loops shown in fig. 4.4 are sensitive to constant accelerations

$$\begin{aligned} \Delta\phi &= \phi_1 - \phi_2 - \phi_3 + \phi_4 \\ &= 3\mathbf{k}_{eff} \cdot \mathbf{g}T^2 - 6\mathbf{k}_{eff} \cdot (\boldsymbol{\Omega} \times \mathbf{g})T^3. \end{aligned} \quad (4.37)$$

This restored acceleration sensitivity becomes problematic when a significant fraction of the atoms contribute to these stimulated echo processes. Rotation-independent

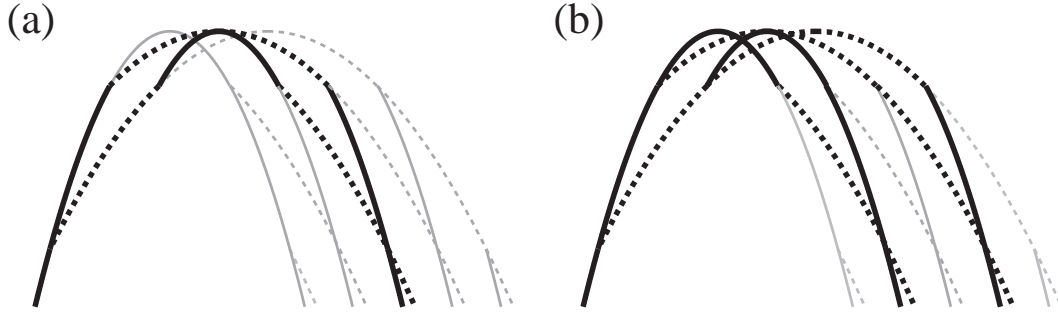


Figure 4.4: Imperfect Raman pulse areas can lead to the formation of spurious closed loops that affect the detected interferometer output. (a) Main interferometer loop for a four-pulse $\frac{\pi}{2} - \pi - \pi - \frac{\pi}{2}$ sequence. (b) Additional interfering loops formed by stimulated echo processes. Because these extra loops exhibit different phase sensitivity to rotations and accelerations from the main interferometer loop, they can lead to errors in the rotation rate measurement.

effects, such as the introduction of gravitational anomalies or slow platform accelerations can now couple directly to the interferometer output.

It has been shown that the effect of these simulated echo processes can be mitigated by slightly changing the direction of \mathbf{k}_{eff} for the different pulses and adjusting the pulse timing such that the phase matching conditions are satisfied for the main interferometer loop but not for the echo processes [85]. If the spatial separation between the interfering paths in the extra loops is larger than the coherence length of the atomic wavepackets, then the fringes from the spurious echo processes get washed out and only contribute to the interferometer output as a constant background.

Chapter 5

Experimental Apparatus

This chapter describes the experimental apparatus, including the laser system, control electronics, and vacuum system. The entire experimental apparatus, shown in fig. 5.1, is designed to be a portable system for mobile inertial and gravitational sensing applications.

5.1 Compact Laser System

The development of a mobile atom interferometer sensor required the miniaturization of the entire experimental apparatus. Considerable time and effort were spent designing and building a compact and rugged laser and control system that could withstand the rigors of a non-laboratory environment.

The laser system was designed to be modular, with a single master laser frame generating the frequencies required to run the experiment, and a series of amplifier frames for obtaining greater optical powers. The frames are stackable, with polarization maintaining optical fibers delivering light between the frames and to the experiment. The laser control electronics and the rf amplifiers and switches are built into separate frames that stack directly beneath the individual laser frames. A single frame stack replaces an entire optical table worth of lasers and optics, and a full rack of associated electronics. A schematic of the laser frame stack is shown in fig. 5.2.

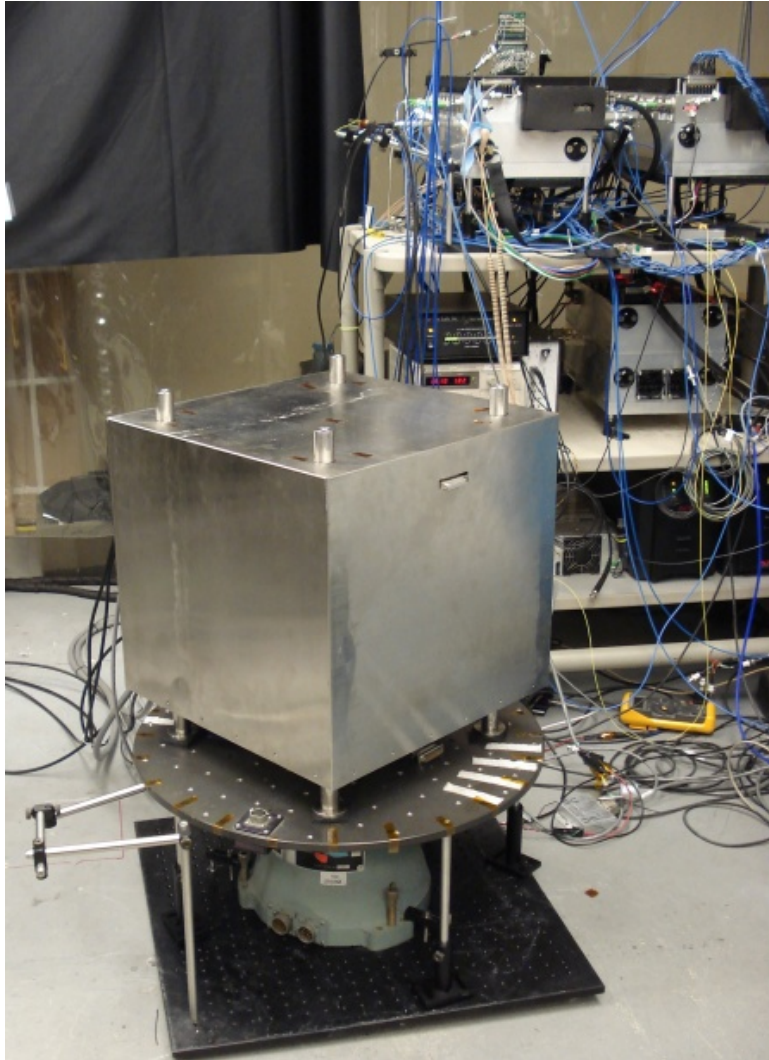


Figure 5.1: A picture of the experimental apparatus. The sensor box on top of the rotating turntable, shown with the magnetic shields on, contains the vacuum chamber and the associated optomechanics. The compact laser and control electronics frames can be seen on the top two shelves of the cart in the background, along with the ion pump controller and temperature interlock box. The bottom shelf houses the power supply and battery backups, as well as the compact tapered amplifier modules.

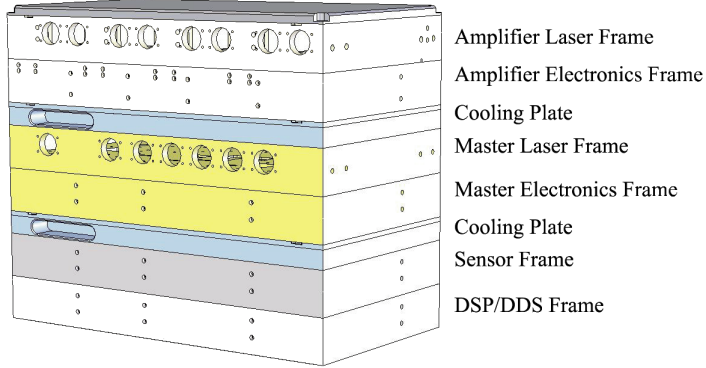


Figure 5.2: A picture of the laser and control electronics frame stack assembly. The modular design allows for the addition of extra laser and electronics frames as needed. The 1 ft. \times 2 ft. \times 2 ft. frame stack replaces an entire optical table worth of optics and a full rack of electronics.

5.1.1 Master Lasers

The master laser frame generates the main frequencies required for the laser cooling and trapping, detection, and Raman beams for the atom interferometry. Three Yokogawa distributed Bragg reflector (DBR) diode lasers (YL85XNW) serve as the master frequency references, and injection lock a series of JDS Uniphase (54-00062) single-mode diode lasers. The Yokogawa lasers have a linewidth of ~ 1 MHz. An anti-reflection (AR) coating was applied to the output facet of the lasers to provide a large tuning range and robust injection locks.

Two Yokogawa DBR diode lasers are locked directly to Cs transitions via saturated absorption spectroscopy, with the $F = 3$ and $F = 4$ master lasers locked to the $F = 3 \rightarrow F' = 2$ and $F = 4 \rightarrow F' = 5$ transitions, respectively. A schematic of the Cs lock is shown in fig. 5.3. Each laser passes through a polarizing beamsplitter, which divides the beam into counterpropagating pump and probe beams through a Cs vapor cell. The probe beam is phase modulated by an electro-optic modulator (EOM) at ~ 4 MHz, and is picked off onto a photodiode. The detected signal is mixed down with the same rf driving the EOM, and a four-wave mixing process gives the error

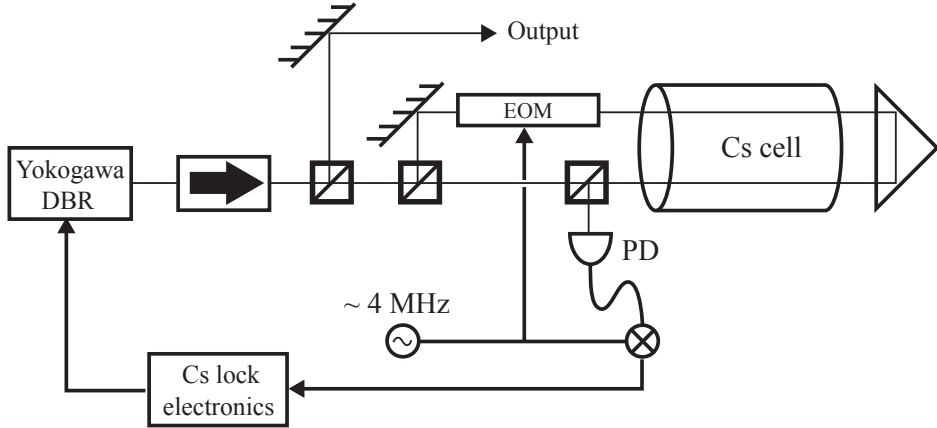


Figure 5.3: Schematic of the saturated absorption spectroscopy laser lock.

signal used to feedback to the master laser current controller. The locking process is fully automated and very robust. The lasers typically remain locked for months at a time, and are stable against temperature fluctuations of up to several $^{\circ}\text{C}$ in the ambient room temperature. A third Yokogawa DBR serves as the master laser for the Raman beams, and is phase locked to the $F = 3$ master laser with a programmable offset frequency of ~ 1 GHz. Light from the $F = 3$ master and Raman amplifier lasers are overlapped on a fast photodiode and mixed down at 1 GHz to generate a feedback signal to the Raman master laser current controller.

Within the master laser frame, the $F = 3$ master laser is frequency shifted up by 172 MHz with a NEOS acousto-optic modulator (AOM), and coupled into a fiber with an output of $\sim 200 \mu\text{W}$. The zero-order (unshifted) light is picked off for the Raman laser offset lock. The $F = 4$ master laser injects a JDSU amplifier laser with an output of ~ 150 mW. The light is double-passed through an AOM, then split into six output fibers, each with an output of $> 500 \mu\text{W}$. The double-passed AOM allows for detunings of up to 70 MHz without losing much power in the fiber outputs. The Raman master laser also injects a JDSU amplifier laser, which is split and coupled into two fibers, each with > 1 mW of power.

The performance of the frames was tested for use in a mobile environment. Thermal cycling of the laser frames over a range of $\Delta T = 20^{\circ}\text{C}$ and mechanical stresses of

$F = 150$ lbs. gave changes in the fiber output power of $\Delta P/P < 3\%$. The frames were also vibration tested at accelerations of $a = 40 \text{ m/s}^2$, resulting in drifts of $\Delta P/P < 6\%$ in the output power.

5.1.2 Amplifier Lasers

The fiber-coupled output powers of the master laser frame are typically on the order of $\sim 1 \text{ mW}$. The amplifier laser frame is designed to amplify the outputs of the master laser frame, as well as provide additional frequency control and fast switching of the light. The amplifier laser frame has eight identical amplifying channels; each channel requires 0.5 mW of injection power and provides a maximum fiber-coupled output power of 50 mW .

Each amplifier channel consists of a JDSU laser, two OFR optical isolators, and a NEOS AOM. The laser diode is injection locked by coupling in light from the master laser frame through an optical fiber, and can output up to 150 mW of power. The laser frequency is shifted up by $\sim 180 \text{ MHz}$ with the AOM, which is driven by rf from a programmable direct digital synthesis (DDS) board. The AOM allows for sub-microsecond switching times, as well as fine-tuning of the output laser frequency. The light is then coupled into another fiber, with a typical maximum output of 50 mW . The lasers operate continuously with constant current, while the AOM rf powers are tuned to adjust the fiber-coupled output powers throughout the experimental cycle.

The incoming DDS rf frequencies are amplified and routed to individual amplifier channels by an rf distribution board. This board also contains attenuators and switches that provide 80 dB of on/off attenuation for the rf, which gives 60 dB of on/off attenuation for the fiber output. The residual power comes from scattered light off of the AOM facet and fiber-coupling optics, and is typically limited to $10 - 100 \text{ nW}$.

5.1.3 Tapered Amplifiers

Tapered amplifier (TA) diodes offer high output powers through broad-area power amplification while maintaining single-mode operation. In this experiment, TAs are

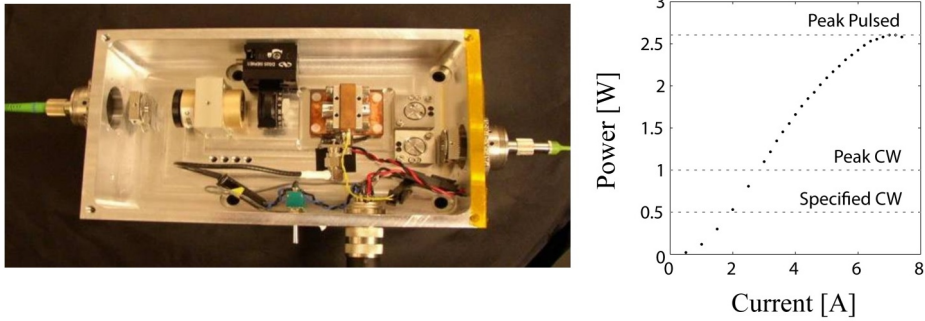


Figure 5.4: On the left, a picture of the tapered amplifier module is shown. The TA is housed in a copper mount that is actively cooled and electrically isolated from the aluminum box. The injection light is collimated out of an optical fiber and focused into the input facet of the TA. The TA output is coupled into another fiber through an optical isolator to eliminate back-reflections. On the right, the total output power of the TA is shown as a function of the pulsed driving current. Peak pulsed powers of up to 2.6 W can be obtained by overdriving the TA current.

used to obtain fiber-coupled powers of up to 500 mW for the Raman and stopping beams, and 200 mW for the 2-D MOT beams.

The TAs used (Eagleyard Photonics EYP-TPA-0850-00500-3006-CMT03-0000) are rated for maximum continuous output powers of 500 mW at 1.5 A of injection current, of which about half can be coupled into a fiber. At higher currents, thermally-induced stress at the facets can permanently damage the TA. However, by operating the TAs in pulsed-mode with a low duty cycle, significantly higher output powers can be achieved by overdriving them at higher currents [86]. A picture of the fiber-coupled TA module is shown in fig. 5.4.

The primary failure mechanism for TAs in pulsed-mode operation is optical damage to the input facet resulting from either amplified spontaneous emission (ASE) or back-reflections. An optical isolator directly after the collimating lenses is used to minimize back-reflections. At high currents, typically > 4 A, the ASE can be large enough to damage the input facet of the TA. Seeding the TA greatly reduces the backwards propagating ASE by saturating the gain and forcing stimulated emission in the forward direction. This allows a TA with constant seed light to be pulsed

at even higher currents. However, for the typical short optical pulses desired, this requires an additional switch or shutter after the TA (for example, an AOM) or very fast switching of the large current. Rather, in this experiment, the TA is operated at moderate currents (~ 3 A) for $500\ \mu\text{s}$, and the seed light is pulsed on for only several μs . Because the ASE output has a different spatial mode than the amplified light, only a small fraction of the total ASE couples into the fiber when the TA is not injected. In addition, the ASE frequency can be tuned far off resonance (~ 840 nm), so that the leakage light has a minimal effect on the atoms.

5.2 Control System and Electronics

The control system is designed to run the experimental sequence. In addition to instrument timing, it is responsible for power up and initialization, diagnostics, frequency synthesis, data acquisition, and signal processing. It also controls the laser system, including frequency stabilization (laser locks) and laser parameter optimization (current and temperature control). Figure 5.5 shows a schematic of the control system architecture.

The system controller is an Innovative Integration SBC6711 digital signal processing (DSP) board. The board features a 900 MFLOP DSP, and was chosen because of its precise timing, compactness, and versatile input/output (I/O). Two Servo16 daughter modules provide the analog to digital and digital to analog conversions at 100 kHz, with a latency time of $30\ \mu\text{s}$. The DSP board is run by a remote terminal (laptop computer) through a custom interface named GradCon.

The DSP uses a low voltage differential signaling (LVDS) system for transmitting digital signals. Digital outputs are used to turn the AOMs and EOMs on and off by controlling a series of rf switches and attenuators. In addition, the DSP generates LVDS signals for triggering the photodetectors and DDS boards. The analog outputs generated by the Servo16 modules run the current controllers for the magnetic field coils, the Cs temperature management, and the laser locks and laser stabilization. Data acquisition is aided by the use of a series of multiplexers for recording the photodetector currents, laser parameters, laser lock error signals, and magnetometer

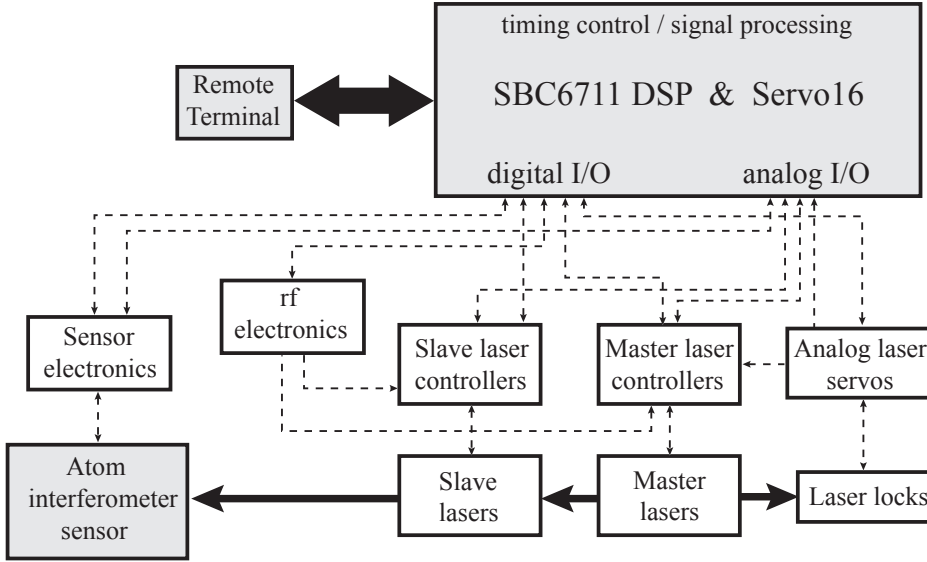


Figure 5.5: Block diagram of the control system. The DSP is responsible for the digital I/O, while the Servo16 modules handle the analog I/O.

readings.

Eight Novatech DDS8m boards generate the rf frequencies for driving the AOMs and EOMs, and are used for dynamic frequency control. The DDS boards can be programmed to either ramp or jump between two predefined frequencies in a phase continuous manner. They are used to control the MOT beam and launch beam detunings, to fine-tune the 9.2 GHz microwave frequency, and for detuning the repump light during the interferometer cycle to minimize scattering of residual leakage light. In addition, two programmable synthesizers provide the frequencies for blasting and detection of the atoms.

The control system and electronics are housed in modular frames similar to the laser frames. The DSP board is housed in the bottom frame, and all of the digital and analog signals are routed through each of the laser/electronics frames. Signal breakout boards allow the simple integration of external devices and electronics if necessary.

5.2.1 Microwave Frequency Generation

The microwave rf electronics are also housed in the same frame as the DSP. The 9.2 GHz rf is used to directly drive transitions between the two hyperfine ground states during the state preparation sequence, as well as for generating the Raman beam frequency difference. The frequency chain begins with a 10 MHz Oscilloquartz (OCXO 8607-BGE) oven controlled crystal oscillator, with a specified phase noise of -120 dBc at 1 Hz. A 100 MHz Wenzel (500-07302) oscillator is phase locked to the Oscilloquartz, and that frequency is multiplied up to 9.2 GHz by a Microlambda (MLPE-1162) phase locked oscillator (PLO). A DDS board generates a frequency of ~ 7 MHz, and is mixed with the 9.2 GHz rf using a single sideband mixer. The sideband frequency can be tuned around the hyperfine splitting frequency in a phase continuous manner by adjusting the DDS frequency.

5.3 Sensor Hardware

The light and electronic signals generated by the laser and control frames are delivered to the main experimental chamber, which consists of the vacuum cell, magnetic field coils, beam delivery optics, and measurement electronics. All of these components are mounted in a box which serves as the gravito-inertial sensor. The sensor box is constructed of stainless steel for structural rigidity and to reduce eddy currents resulting from changing magnetic fields. A picture of the sensor box frame is shown in fig. 5.6.

The laser light delivered by the optical fibers is split between the two MOTs by an array of Canadian Instrument Research Labs (CIRL 968P) fixed ratio fiber splitters. The beam collimation and delivery optics for the trapping, stopping, detection, and Raman light are mounted directly to the frame. The Raman retro-reflecting mirror is also attached rigidly to the frame, so that the motion of the entire sensor box is reflected in the differential phase measurement. Access holes allow the custom Siskiyou flexure mounts to be tweaked from the outside.

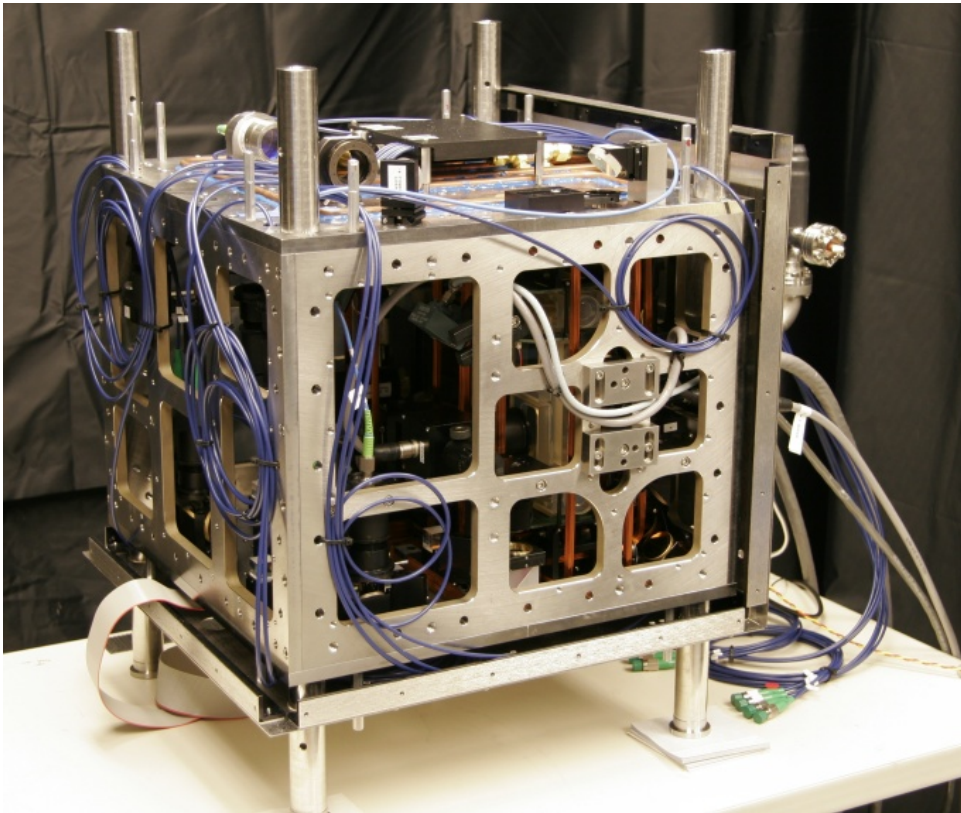


Figure 5.6: A picture of the sensor box with the magnetic shields removed. Light is delivered from the laser frames by the blue optical fibers, while electronic signals are routed through the gray cables. The fiber optic splitters and the collimation and delivery optics for the Raman beam can be seen atop the sensor box. The vacuum cell is located inside the box, while the ion pump is mounted just outside of the magnetic shielding.

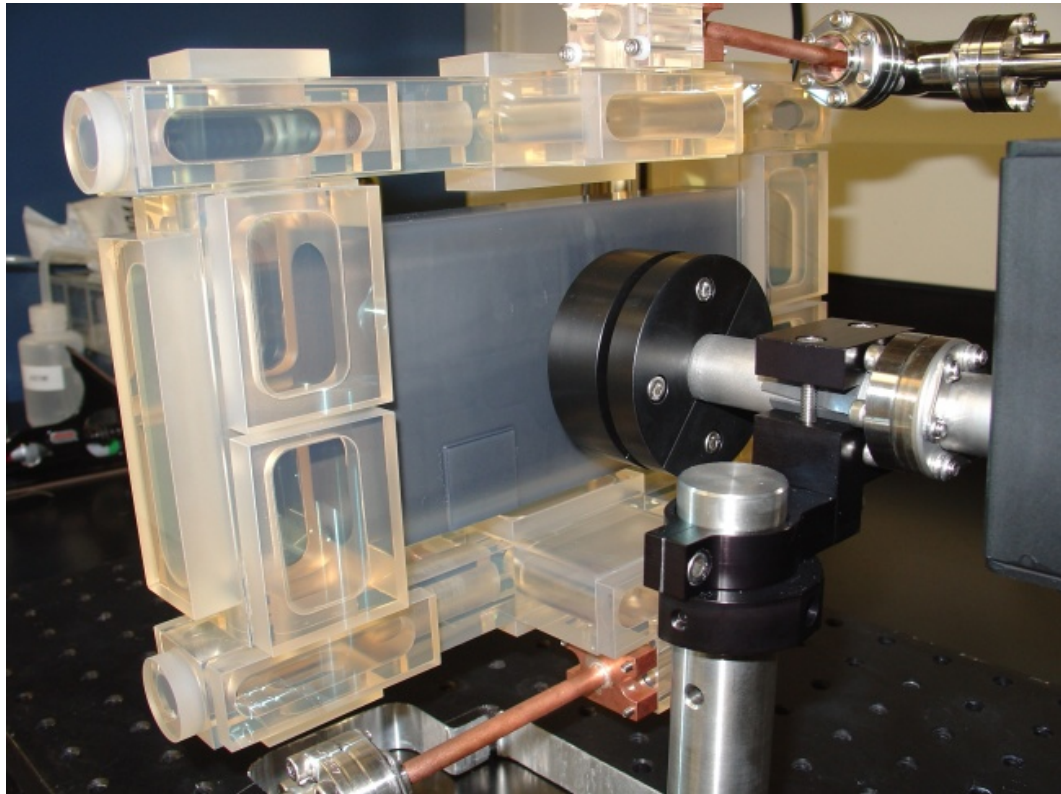


Figure 5.7: A picture of the Zerodur vacuum cell. The ion pump is attached to the center of the cell with an indium seal. The inner walls of the main chamber have been painted with Aquadag. The copper tubes seen at the top and bottom are used for transferring Cs into the vacuum cell, and are pinched off before the cell is mounted in the optomechanics assembly.

5.4 Vacuum System

Atom interferometers need to operate under ultra-high vacuum (UHV) conditions to avoid collisions with background particles, which can lead to spurious phase shifts. The vacuum cell used in this experiment, shown in fig. 5.7, is constructed almost entirely of Zerodur®[87], a glass ceramic with a very low coefficient of thermal expansion and low helium permeability that is both machinable and polishable. An all Zerodur vacuum cell allows for good optical access, while limiting background pressure due to outgassing and diffusion of helium.

The vacuum chamber is constructed by bonding pieces of Zerodur together using a hydroxide-catalyzed hydration/dehydration process originally developed at Stanford University [88]. The surfaces being bonded must first be polished to sub-micron flatness. Two parts of a sodium silicate solution containing 14% NaOH and 27% SiO₂ are mixed with five parts de-ionized water and applied between the two surfaces. The solution is allowed to sit for several days, during which time the silicate forms covalent bonds between the two sides, fusing them into a single piece of Zerodur. The process is simple and inexpensive, and produces mechanically strong bonds [89]. Hydroxide-catalyzed bonding has many advantages over other techniques such as optical contacting, epoxies, and frit bonding because the bonds it creates are optically transparent, it is structurally and thermally reliable, and it is a cold technique.

The main vacuum chamber, which serves as the Raman interaction region, is machined out of a single block of Zerodur. Two milled out MOT chambers are bonded onto the top and bottom sides, and two additional small blocks of Zerodur are bonded onto the 2-D MOT regions for storing the Cs. AR coated windows are bonded onto each surface where a MOT beam or Raman beam enters the vacuum cell.

UHV is maintained in the main chamber and 3-D MOT regions by a 5 L/s Heat-Wave Labs (360560-02) ion pump attached to the center of the vacuum cell via an indium seal. Ion pumps are particularly useful because of their small size and long lifetimes at UHV, and because they operate free of vibrations or contaminants. The ion pump current is used as a rough indicator of the internal vacuum pressure, although at typical operating pressures below 10⁻⁹ Torr the ion pump current is not a very reliable measure of the absolute pressure. The vacuum cell is held in place at a single point by the ion pump port to avoid over-constraining the cell. A 0.06 in. diameter hole serves as a flow restricting throttle for providing differential pumping of the 2-D MOT region.

In addition to the ion pump, getters are used to control the background pressure in the vacuum cell. Graphite plugs are inserted in the path of the 2-D MOT beam to absorb the atoms that are not trapped by the 3-D MOT. The inside of the Raman interaction region is painted with Aquadag, an aqueous graphite solution used to

reduce the background Cs vapor pressure in the vacuum cell.

The vacuum cell is initially pumped out using a turbomolecular pump. It is then thermally cycled above 100°C up to six times over several days to bake off any residual water. A copper tube containing a Cs ampoule is fitted to the vacuum cell with an indium seal, and the Cs is transferred by heating the tube up to 200°C while a cold finger maintains the Cs reservoir at 20°C. After several hours, the copper tube is pinched off and the ampoule is removed.

The Cs reservoir is maintained at $\sim 5^\circ\text{C}$ by a thermo-electric cooler. The temperature of the Cs determines the density of the thermal vapor from which the 2-D MOT is loaded, and is optimized for the 2-D MOT atom flux. If the vapor pressure is too low, then there are not enough atoms to trap. If the vapor pressure is too high, then excessive absorption leads to an imbalance in the retro-reflected 2-D MOT beams, reducing the atom flux.

5.5 Magnetic Field Control

The 2-D and 3-D MOT coils are responsible for generating the magnetic field gradients required for trapping the atoms. They consist of pairs of symmetric anti-Helmholtz coils along each trapping axis, which give an approximately linear field gradient at the center of the trap.

The 3-D MOT coils consist of 39 turns in an eight layer printed circuit board (PCB), which generates a gradient of 0.7 G/cm for 0.25 A of current. Each coil dissipates approximately 0.2 W at 0.25 A, but the coils are thermally isolated from the vacuum cell so that the heat generated does not couple directly to it.

The 2-D MOT coils are constructed of copper wire. Because of the tight spatial constraints around the vacuum cell, the coils along the $\hat{\mathbf{y}}$ and $\hat{\mathbf{z}}$ directions have different sizes. The number of turns in each pair of coils is varied to provide the same magnetic field gradient along both axes. The magnitude of the radial field gradient is 8 G/cm at 1.2 A of current, with 1 W dissipated per coil. The asymmetry in the coils leads to a non-zero longitudinal field gradient along the $\hat{\mathbf{x}}$ direction.

The bias fields are generated by three pairs of coils for each interferometer. The

layout of the coils is shown in fig. 5.8. The bias coils are used to compensate for the longitudinal field gradient created by the 2-D MOT coils during the atom loading, and for generating a constant magnetic bias field during the atom interferometry experiment, which defines a fixed quantization axis for the atoms.

The two states used in the atom interferometry experiments are the $m_f = 0$ magnetic sub-levels of the $F = 3$ and $F = 4$ hyperfine ground states. These states are first-order insensitive to magnetic fields, but are still subject to a quadratic Zeeman shift, which shifts the hyperfine splitting by $\Delta\nu_{\text{HFS}} = 427.5 \text{ Hz/G}^2$.

In general, a spatially uniform, constant magnetic field does not affect the interferometer phase because of the symmetry between the two interfering paths. In both the $\frac{\pi}{2} - \pi - \frac{\pi}{2}$ and $\frac{\pi}{2} - \pi - \pi - \frac{\pi}{2}$ sequences, the atom spends equal amounts of time in the $F = 3$ and $F = 4$ states along each path, canceling out the effect of any level shifts due to the quadratic Zeeman shift. However, time-dependent or spatially inhomogeneous magnetic fields may lead to a spurious phase shift. If the magnetic field is not constant and uniform, then jitter in the launching or the timing sequence can lead to shot-to-shot fluctuations in the differential phase.

In order to minimize magnetic field inhomogeneities inside the sensor box, the magnetizations of all of the optomechanical components are tested before being installed. In addition, magnetic shields are used to suppress the large magnetic field of the ion pump and other external sources, including the Earth's ambient field. Magnetic shielding of the vacuum cell is provided by two layers of mu-metal, as shown in fig. 5.9. Each layer reduces the magnetic field within the shield by a factor of ~ 100 . Two independent sets of bias magnetic field coils are used to cancel out the residual magnetic field at the mG level, so that any residual phase noise is below 1 mrad.

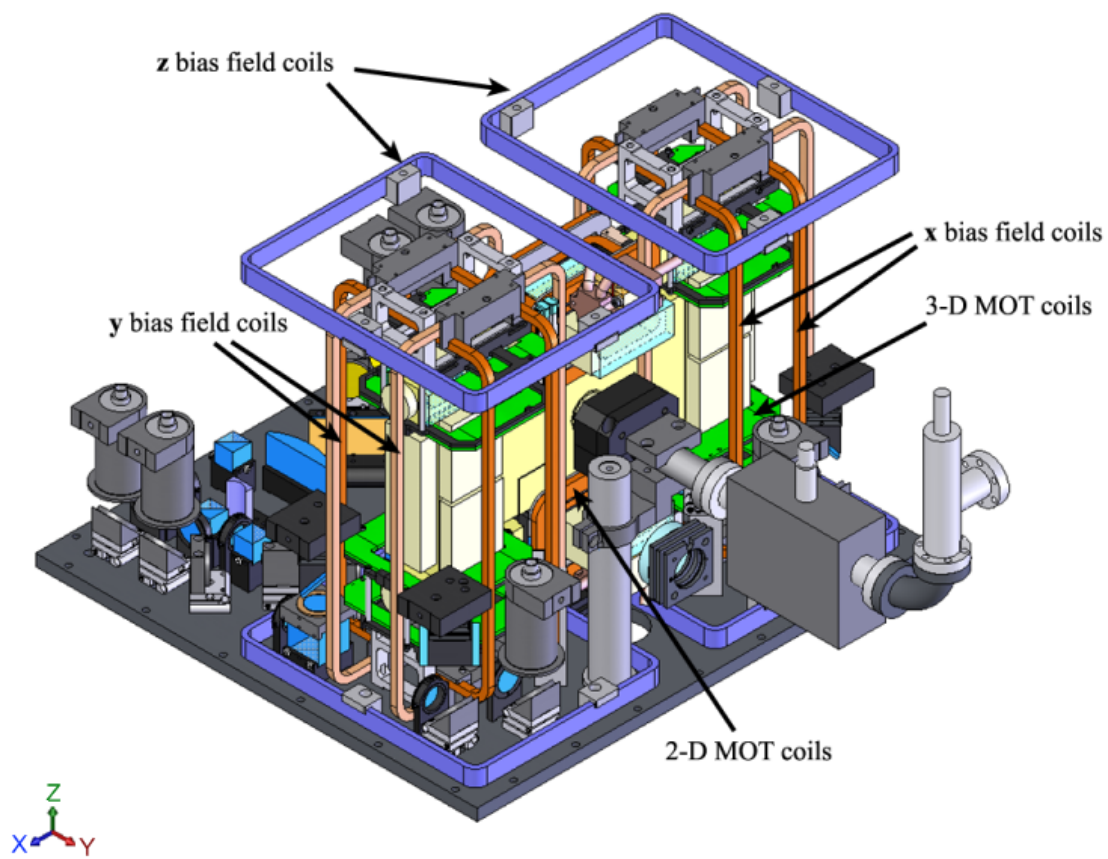


Figure 5.8: Diagram of the MOT and bias magnetic field coils. The 3-D MOT coils are multi-layered PCBs. There are three pairs of orthogonal bias field coils for each atom interferometer.

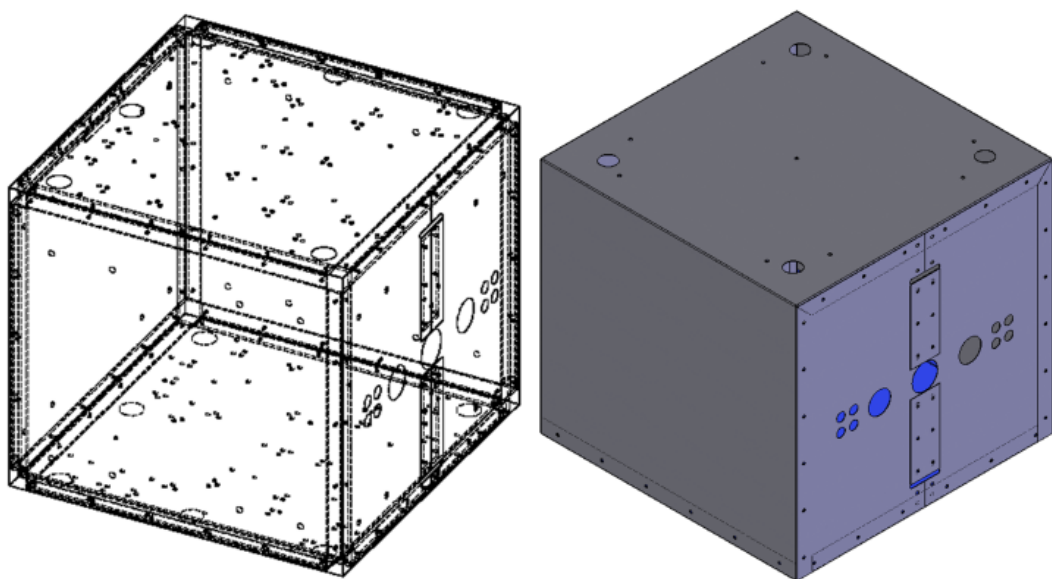


Figure 5.9: A picture of the inner and outer magnetic shields. The inner shield has a large number of access holes for the optomechanics inside the box.

Chapter 6

Interferometer Operation

This chapter discusses the operation of the atom interferometer, including atom loading and state preparation, the retro-reflected Raman beam configuration, and the detection system. A schematic of the experimental sequence is shown in fig. 6.1.

6.1 Atom Loading and Launching

The Cs atoms are initially loaded into a 2-D MOT from a thermal vapor. The atoms are cooled and constrained along two axes, but are free to move along the third, creating a narrow flux of $\sim 10^9$ atoms/s out of both ends of the trap. A double-ended 2-D MOT is advantageous because it reduces the total optical power requirement by eliminating the need for a second trap. The 2-D MOT consists of two retro-reflected elliptical trapping beams, each with 100 mW of power, overlapped with ~ 1 mW of repumping light. Because of absorption in the vapor, the beam collimations must be slightly divergent in order to achieve proper beam intensity balance at the edges of the MOT. The two 3-D MOTs are loaded from the 2-D MOT flux, with approximately 2×10^8 atoms loaded into the trap over 200 ms.

Before the atoms are launched, the magnetic field coils are turned off and the atoms are briefly held in a 3-D optical molasses for 60 ms while eddy currents are allowed to dissipate. The atoms are then launched in a moving molasses by detuning the vertical beams by ± 1.6 MHz, accelerating the atoms to a velocity of $v \approx 1.3$ m/s. As

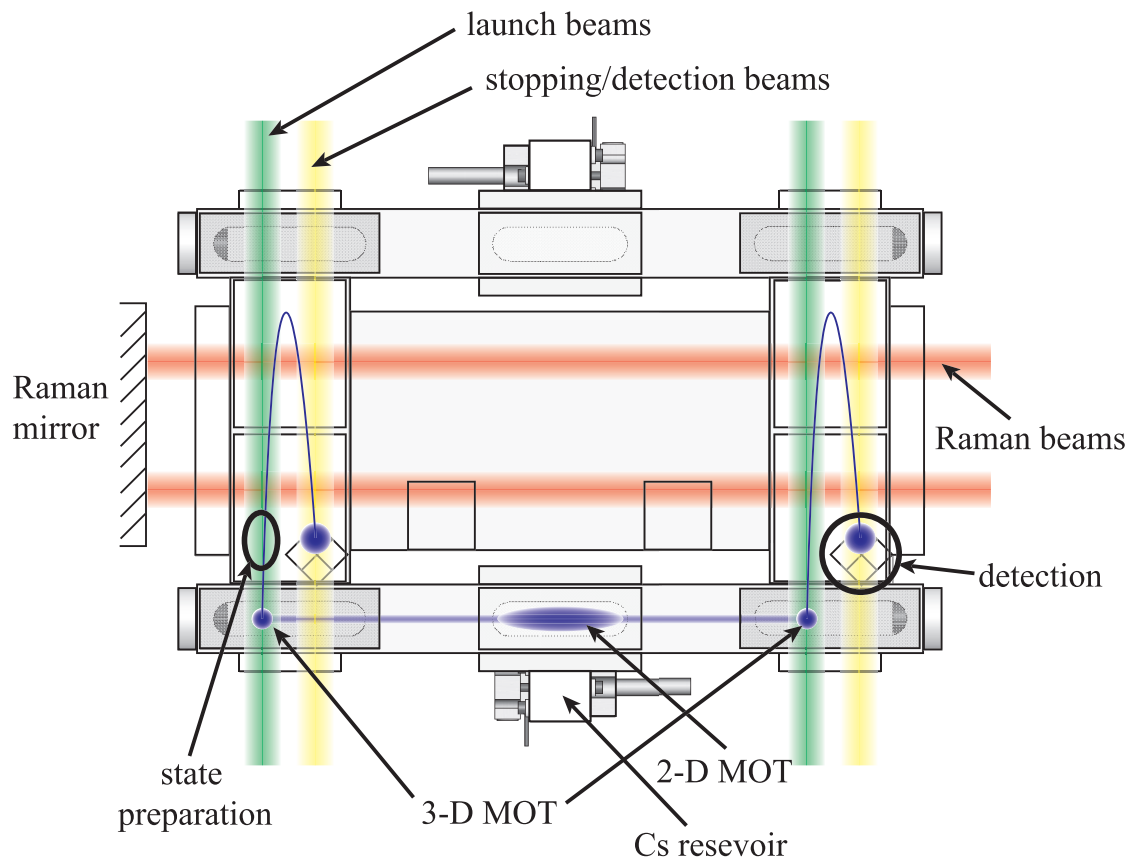


Figure 6.1: Schematic of the experimental sequence. Cs atoms are loaded into two 3-D MOTs from a double-ended 2-D MOT. They are then launched vertically in a moving molasses, and the $m_f = 0$ atoms are state selected. The retro-reflected Raman beams drive the interferometer pulse sequence, and the final state populations are detected at the bottom of the atomic trajectory.

the atoms are being accelerated, the transverse MOT beams are left on to continue cooling the atoms along the transverse direction. The atoms' launch direction is determined by the alignment of the transverse MOT beams, and is independent of the vertical beam alignment.

As the atoms are being launched, they are cooled via polarization gradient cooling. The beam intensities are reduced to 1/10 of the initial values and frequency detuned by 70 MHz. The temperature of the atomic ensemble along the Raman beam axis is measured using velocity selective Raman transitions [80], and is typically $\sim 2 \mu\text{K}$. The velocity spread in the vertical direction is measured by imaging the atomic cloud with a CCD camera. The initial vertical cloud size after launching is $r_{1/e} \approx 2 \text{ mm}$, and the final size at the end of the atomic fountain after 260 ms is $r_{1/e} \approx 8 \text{ mm}$, corresponding to a temperature of $\sim 7 \mu\text{K}$.

6.2 State Preparation

At the conclusion of the launch sequence, all of the atoms are in the $F = 4$ ground state, randomly distributed among the nine m_F sub-levels. Only the $m_F = 0$ sub-levels of the $F = 3$ and $F = 4$ ground states are used in the atom interferometry experiments because they are first-order insensitive to magnetic fields. This minimizes the effects of stray magnetic fields on the differential phase shift.

The $m_F = 0$ atoms are state selected prior to the interferometry sequence. A magnetic bias field is applied along the Raman beam propagation direction to break the degeneracy of the m_F sub-levels. The splitting between adjacent levels is typically around 50 – 100 kHz. A microwave horn drives atoms from the $F = 4, m_F = 0$ level down to the $F = 3, m_F = 0$ level with a 100 μs long microwave π -pulse. Atoms in the other $F = 4$ magnetic sub-levels remain unaffected.

A blasting pulse tuned to the $F = 4 \rightarrow F' = 5$ cycling transition is then applied, causing the atoms remaining in the other $F = 4$ sub-levels to scatter photons. Each scattered photon gives the atoms a velocity recoil of 3.5 mm/s. For typical atomic fountain times of ~ 250 ms, only 10 – 20 photon scatters are required to knock an atom out of the detection region. As a result, the $F = 4$ atoms are blasted away,

leaving behind an ensemble of $\sim 2 \times 10^7$ atoms in the $F = 3, m_F = 0$ state. During the blasting, a very small fraction ($\sim 0.2\%$) of the atoms depump into the $F = 3$ state, randomly populating different m_F sub-levels.

Because the sensitivity of the atom interferometer is ultimately limited by shot noise due to the finite number of atoms, a more efficient state selection sequence is desirable. The initial atom number could improve by up to a factor of 9 by employing optical pumping and other techniques. In a system very similar to this experiment, Zeeman state optical pumping is used to increase the atom number by a factor of three [90].

6.3 Raman Beam Configuration

In this experiment, the two-photon Raman transitions are driven by a single phase modulated retro-reflected beam. A schematic of the Raman beam generation system is shown in fig. 6.2. The master Raman laser is phase locked to the repumper laser with a frequency offset of ~ 1 GHz from the $F = 3 \rightarrow F' = 2$ transition. The light is amplified by injection locking a slave laser for a total fiber output of ~ 50 mW. A Photline (NIR-MPX850-LN08) fiber modulator is used to generate sidebands at the 9.2 GHz hyperfine splitting frequency. After a 4 dB reduction in power due to insertion loss in the fiber modulator, the light is amplified up to > 400 mW by a TA. The Raman system also provides a second unmodulated output for added flexibility, in the case that two independent Raman beams are desired.

The Raman beam is collimated on the top plate of the sensor box, and the beam profile is shaped to obtain nearly uniform intensity while limiting the amount of clipping on the vacuum cell. The beam is then delivered into the vacuum cell as shown in fig. 6.3. A non-polarizing beamsplitter delivers the Raman beam at two different levels, and a single optical flat retro-reflects the two beams. The height of the beamsplitter can be adjusted to alter the pulse timing.

One of the principal advantages of using a single laser is that any phase noise due to the optical fibers or delivery optics up until the final retro-reflecting mirror is common to both frequencies. The effective phase $\phi_{eff} = \phi_1 - \phi_2$, given by the difference of the

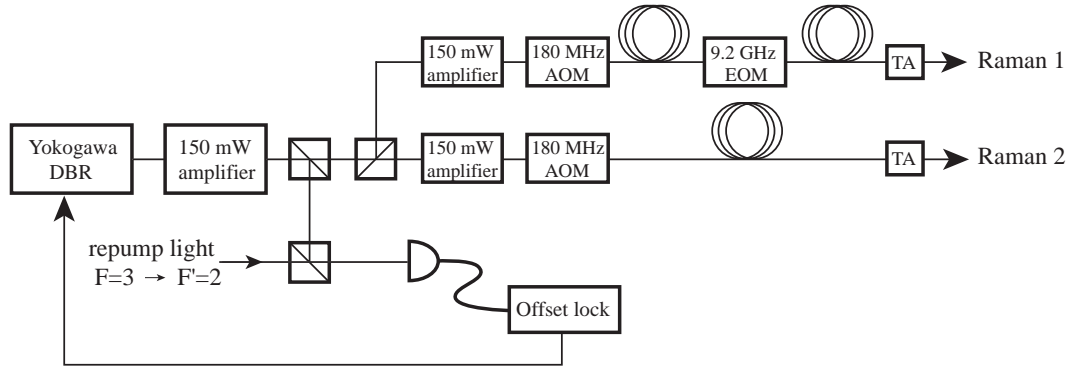


Figure 6.2: Schematic for generating the Raman beams. Raman 1 is the phase modulated light. Raman 2 is a secondary output if two separate beams are desired.

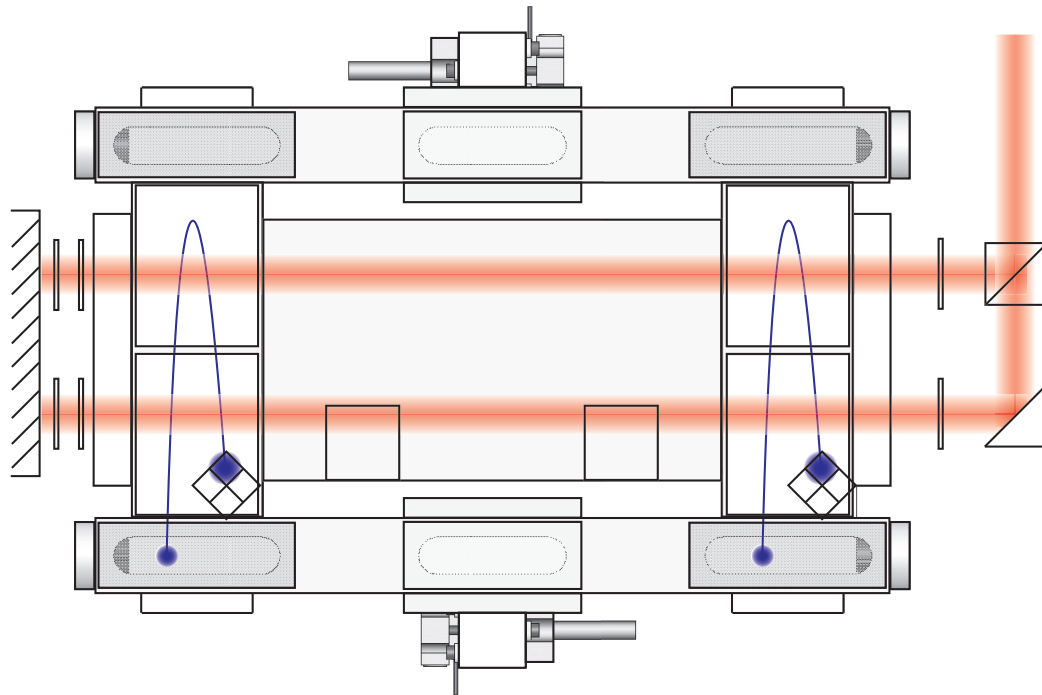


Figure 6.3: Diagram outlining the delivery of the Raman beams. The position of the non-polarizing beamsplitter can be adjusted in order to change the pulse timing. A single optical flat is used to retro-reflect the beam at both levels. The quarter waveplates used to set the beam polarizations are also shown.

local phases of the two Raman frequencies, is determined by the distance from the atom to the mirror. Therefore, as long as the retro-reflecting mirror is stable, phase noise due to the optical delivery is suppressed and the phase of a single interferometer can be determined directly without having to resort to a differential measurement.

Another advantage of the retro-reflected Raman beam scheme is that the effective wave vector, given by the difference $\mathbf{k}_{eff} = \mathbf{k}_1 - \mathbf{k}_2$, is largely immune to jitter in the input angle of the Raman beam. Changes in the direction of \mathbf{k}_{eff} can lead to a degradation of the interferometer contrast, and can affect the coupling of local gravity \mathbf{g} with the interferometer phase. Since \mathbf{k}_1 and \mathbf{k}_2 form opposite angles with respect to the mirror surface normal \mathbf{n} , and $|\mathbf{k}_1| \approx |\mathbf{k}_2|$, the components perpendicular to \mathbf{n} cancel out and $\mathbf{k}_{eff} \parallel \mathbf{n}$ regardless of the input angle.

One disadvantage of the retro-reflecting scheme is that the counterpropagating frequencies can lead to standing waves that degrade interferometer contrast if polarizations are not perfect. Spatial variations in the laser field intensity give an inhomogeneous distribution of Rabi frequencies, which leads to decoherence in the atomic ensemble.

Another problem specific to phase modulating the light arises from the interference of multiple sidebands pairs [91]. The spectrum resulting from the phase modulation is shown in fig. 6.4. Because the phase modulation generates multiple sidebands with the same frequency difference, there are multiple pairs of frequencies that can drive resonant two-photon transitions, each with a different single photon detuning and, consequently, a different effective Rabi frequency.

Consider the effect of just the carrier (ω_c) and the ± 1 sidebands ($\omega_c \pm \omega_{rf}$). Two pairs of frequencies, ω_c and $\omega_c + \omega_{rf}$, and ω_c and $\omega_c - \omega_{rf}$ are resonant with the microwave transition. The effective Rabi frequency resulting from both pairs has the form

$$\Omega_{eff}(l) = \frac{\Omega_{+1}^* \Omega_c}{2\Delta_{+1,c}} e^{ik_{rf}l} + \frac{\Omega_c^* \Omega_{-1}}{2\Delta_{c,-1}} e^{-ik_{rf}l}, \quad (6.1)$$

where l is the distance from the atom to the retro-reflecting mirror. Ω_{eff} therefore has a spatial periodicity of $\lambda_{rf}/2$. The phase modulation produces a symmetric spectrum so that $\Omega_{+1}^* \Omega_c = \Omega_c^* \Omega_{-1}$. Also, since $\Delta_{+1,c} = \Delta_{c,-1} + \omega_{rf}$, the amplitude of the spatial

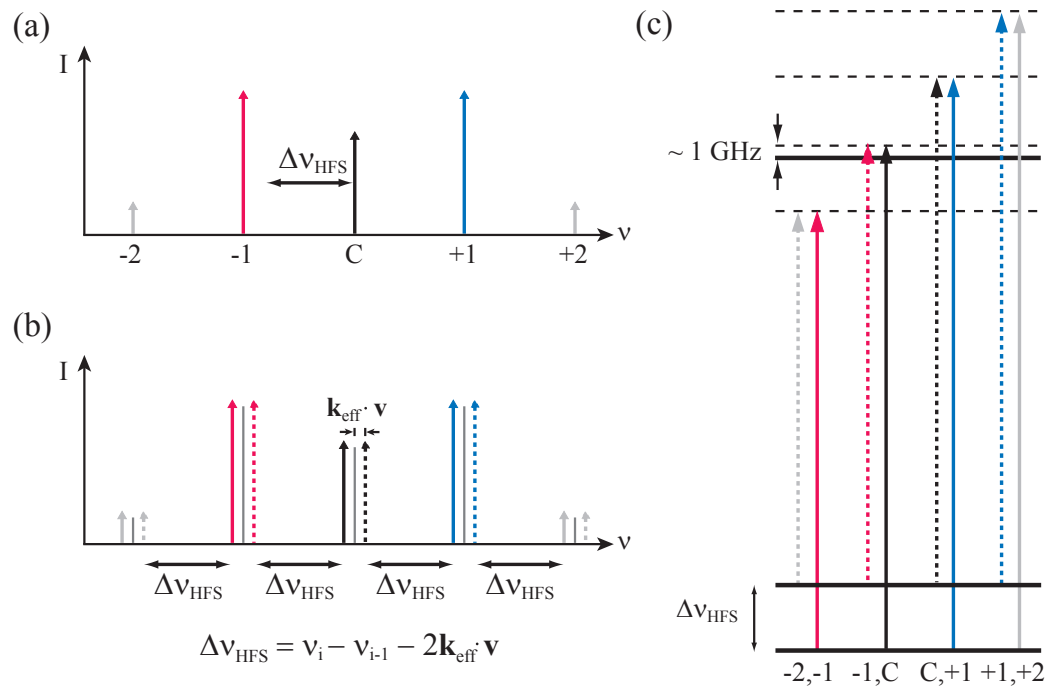


Figure 6.4: Raman beam spectrum. (a) The spectrum of the phase modulated Raman laser. (b) The counterpropagating laser frequencies are Doppler shifted in opposite directions in the rest frame of the atom. Multiple frequency pairs form resonant two-photon Raman transitions. (c) The resonant two-photon pairs are shown with their single photon detunings.

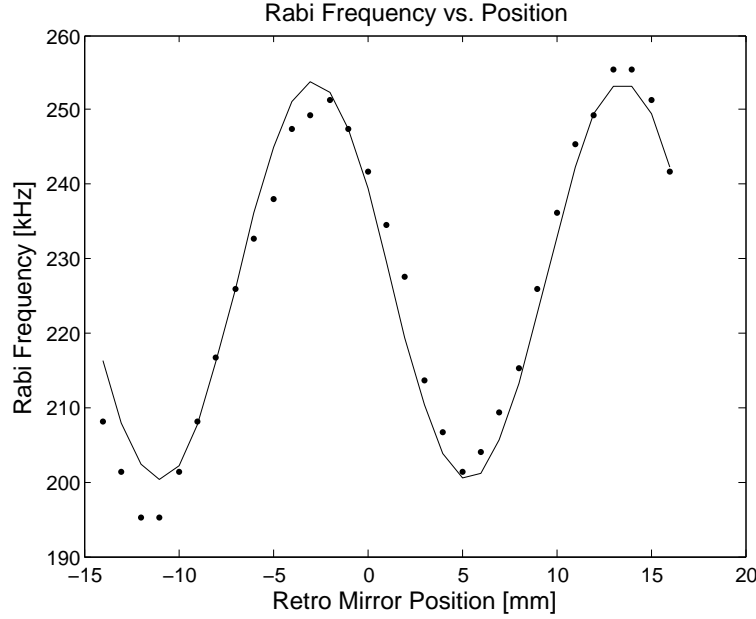


Figure 6.5: Spatially dependent Rabi frequency showing $\lambda_{rf}/2 = 1.6$ cm periodicity.

variations in the Rabi frequency depends only on the detuning of the main frequency pair, ω_c and $\omega_c - \omega_{rf}$.

The spatial dependence of the Rabi frequency due to multiple sidebands is shown in fig. 6.5. The wavelength of oscillations is given by $\lambda_{rf}/2 \approx 1.6$ cm as expected. Figure 6.6 shows the magnitude of the oscillations in the Rabi frequency for different detunings from the $F = 4 \rightarrow F' = 5$ transition. As the detuning gets larger, the relative contribution from the secondary frequency pairs gets larger, leading to a greater fractional change in the Rabi frequency over the rf wavelength. Therefore, small single photon detunings are desirable for minimizing this effect. However, at detunings of much less than ~ 1 GHz, the driving frequency is close enough to resonance to start inducing spontaneous emission events, which also leads to loss of fringe contrast through decoherence. An operating detuning of ~ 0.8 GHz is selected to optimize the total fringe contrast.

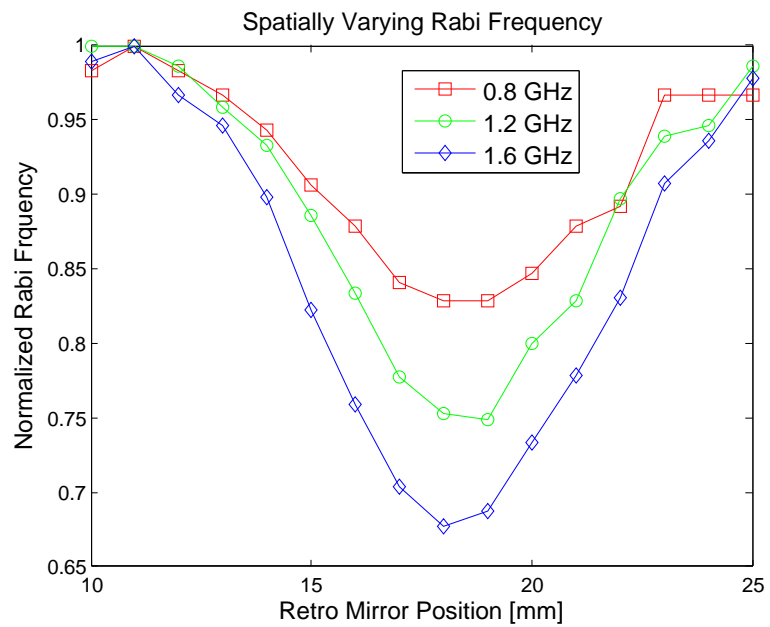


Figure 6.6: Relative amplitude of Rabi frequency variations for different detunings. For smaller detunings, the contribution from the main frequency pair dominates, and the relative magnitude of the Rabi frequency oscillations decreases.

6.4 Detection System

The probability of an atom being in either one of the hyperfine ground states at the end of the interferometer sequence is given by the differential phase between the two arms of the interferometer. Given an ensemble of atoms, measuring the relative populations in the two final states gives a direct way of obtaining the differential phase, and thus the effects of any inertial or gravitational forces on the atoms. Because of shot-to-shot fluctuations in the total number of atoms detected, both populations must be measured directly. In this experiment, the final populations of the $F = 3$ and $F = 4$ ground states are determined by a normalized fluorescence detection scheme described in detail in [92]. This normalized scheme greatly reduces noise due to atom number fluctuations, as well as from frequency and amplitude noise in the detection laser.

At the completion of the interferometer sequence, each atom is in a superposition of the $F = 3$ and $F = 4$ ground states, and is falling under the influence of gravity. Initially the two states are spatially overlapped, with a transverse momentum difference of $\hbar \mathbf{k}_{\text{eff}}$. If the atoms were to continue falling freely, the velocity difference would eventually give enough of a separation to spatially resolve the two states; however, for typical recoil velocities and atom cloud sizes, this would take much too long (> 1 s). Instead, light resonant with the $F = 4 \rightarrow F' = 5$ transition is used to collapse the atomic wavefunctions into either of the two states, “stopping” the $F = 4$ atoms while allowing the $F = 3$ atoms to continue to fall under the influence of gravity. The stopping pulse imparts enough momentum to the $F = 4$ atoms such that the two clouds can be spatially resolved within a short amount of time, typically ~ 10 ms. A CCD camera image showing the spatially resolved states can be seen in fig. 6.7.

Once the two states are spatially separated, the $F = 3$ atoms are optically pumped into the $F = 4$ state. The two clouds are then simultaneously detected via fluorescence by illuminating them with a detection beam tuned slightly to the red of the $F = 4 \rightarrow F' = 5$ transition, along with a repumping beam. The fluorescence from each cloud is captured on a different quadrant of a quadrant photodiode detector.

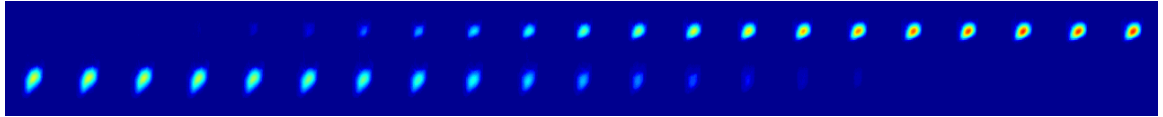


Figure 6.7: A CCD image of the detected atoms showing the change in the relative populations between the $F = 3$ and $F = 4$ states as an interferometer fringe is scanned.

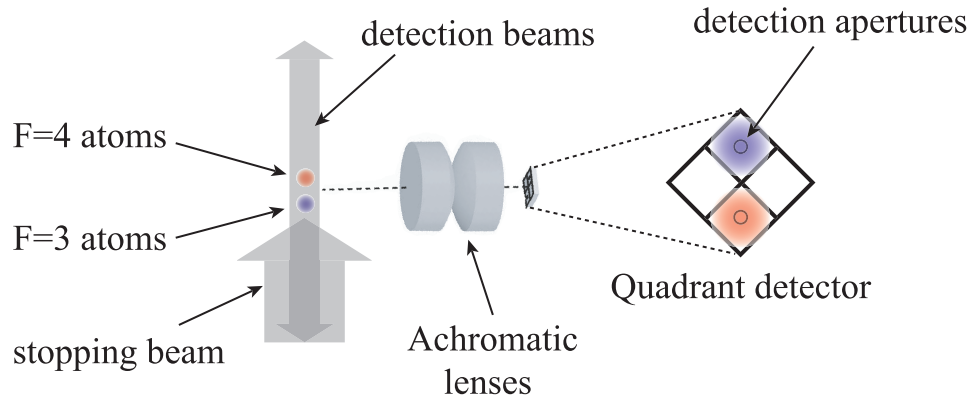


Figure 6.8: Schematic of the detection system.

Simultaneously detecting both states using the same detection laser ensures that any amplitude or frequency fluctuations in the detection beam is common to both signals, and does not affect the relative population measurement.

In this experiment, the $F = 4$ atoms are stopped by a $\sim 30 \mu\text{s}$ pulse on resonance with the $F = 4 \rightarrow F' = 5$ transition. The atoms are allowed to fall freely for $\sim 15 \text{ ms}$, at which point the $F = 3$ atoms are repumped into the $F = 4$ state and the detection beam is turned on. The fluorescence is imaged onto a Hamamatsu (S5981) quadrant detector using two achromatic lenses located 3 cm from the atoms. The $F = 3$ and $F = 4$ atoms are imaged onto the top and bottom quadrants of the detector, respectively. A schematic of the detection system is shown in fig. 6.8.

The detection efficiencies for the two states are not equal due to several factors. Applying the stopping pulse heats the $F = 4$ atoms, resulting in different cloud sizes for the two states. Imperfect imaging can lead to different effective solid angles

and bleed-through between quadrants. Inhomogeneities in the stopping beam and depumping during the stopping pulse lead to a “smearing” of the $F = 4$ atoms that further contributes to bleed-through and different detection efficiencies. In addition, the different initial velocities between the freely falling $F = 3$ atoms and the slowed down $F = 4$ atoms at the time of detection gives a Doppler shift that results in slightly different frequency responses to the detection light.

To account for the difference in detection efficiency, the total atom signal is assumed to have the form

$$\alpha V_3 + \beta V_4 = N, \quad (6.2)$$

where V_3 and V_4 are the integrated photodiode signals for the $F = 3$ and $F = 4$ atoms, respectively. The normalized $F = 4$ population is calculated as

$$N_4 = V_4 / (\epsilon V_3 + V_4), \quad (6.3)$$

where the normalization constant $\epsilon = \alpha/\beta$ is determined empirically by scanning the phase of an interferometer fringe and performing a least squares fit. In this experiment, the normalization coefficient is recalculated every 100 points to account for any drifts in the relative detection efficiencies.

6.4.1 Signal-to-Noise Ratio

Normalized detection is critical to obtaining signal-to-noise ratios (SNR) approaching the atom shot noise limit. The SNR in this experiment is defined as $1/\sigma_{\Delta\phi}$, where $\sigma_{\Delta\phi}$ is the uncertainty in the measurement of the differential phase $\Delta\phi$. $\sigma_{\Delta\phi}$ is evaluated by driving the atoms into an equal superposition of the two hyperfine ground states, and measuring the standard deviation of the normalized $F = 4$ population σ_{N_4} . Since the transition probability is given by

$$|c_e(t)|^2 = \frac{1}{2} + \frac{1}{2} \cos(\Delta\phi), \quad (6.4)$$

the noise on the detected population is multiplied by a factor of 2 to obtain the phase noise $\sigma_{\Delta\phi} = 2\sigma_{N_4}$. The noise is measured for both interferometers simultaneously to

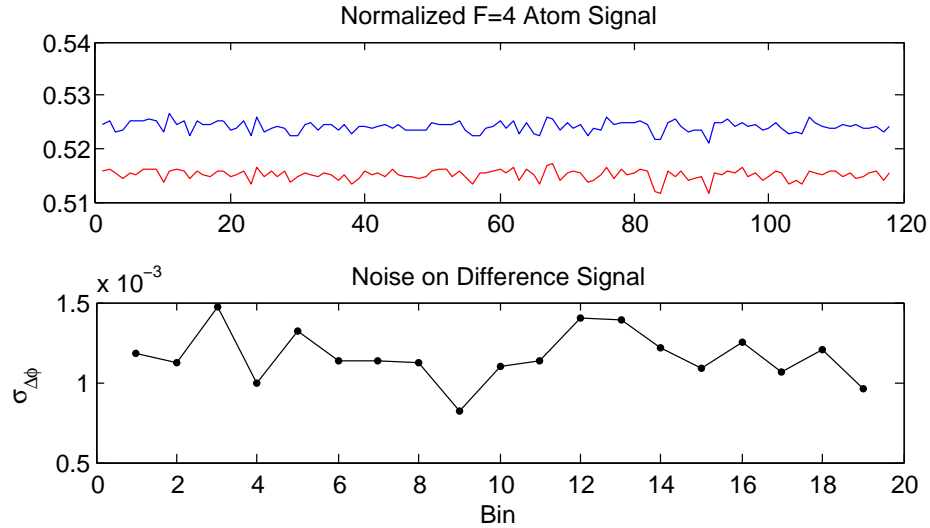


Figure 6.9: Detection system SNR. The top plot shows the normalized $F = 4$ populations for the two atom interferometers. The noise on the difference signal between the two outputs gives a SNR of 860 : 1.

account for any common phase fluctuations due to the microwave system.

One critical factor in obtaining good detection SNR is to control the frequency and intensity noise of the stopping pulse. As a result, a TA is used to amplify the stopping pulse power to $> 20 I_{\text{sat}}$. When the light is well above saturation, intensity fluctuations no longer matter, and the atoms also become less sensitive to frequency noise in the stopping pulse because of power broadening.

In this experiment, SNRs of up to 860 : 1 have been obtained using this normalized fluorescence detection technique. Figure 6.9 shows the uncorrelated noise between two atom interferometers sitting on the side of a microwave clock fringe. The SNR is close to approaching the shot noise limit of 1100 : 1 expected for the 5×10^6 atoms detected. The current limiting factor is shot-to-shot position jitter in the atomic cloud. The factor of four reduction in the number of atoms detected at the end of the interferometer cycle is due to the imaging optics and the expansion of the atomic cloud.

Chapter 7

Rotation Rate Measurements

This chapter summarizes the results for the measurement of the Earth's rotation rate. The performance of the atom interferometer in gyroscope mode is discussed, and a method for eliminating multiple path interference in the four-pulse interferometer sequence is demonstrated. A precision measurement of the Earth's rotation rate using Raman wave vector reversal is presented, and the prospect of using conventional inertial sensors to improve the vibration-limited performance of the atom interferometer is explored.

7.1 Four-Pulse Interferometer Sequence

Rotation rate measurements are performed using the four-pulse $\frac{\pi}{2} - \pi - \pi - \frac{\pi}{2}$ interferometer sequence. This pulse sequence is insensitive to constant accelerations, and therefore immune to long-term drifts in the beam pointing that can change the coupling of \mathbf{g} . For a constant rotation, the interferometer phase shift is given by

$$\Delta\phi = \frac{2m}{\hbar}\boldsymbol{\Omega} \cdot \mathbf{A} + 2\mathbf{k}_{eff} \cdot (\boldsymbol{\Omega} \times \mathbf{g})T^3 + \Delta\phi^0, \quad (7.1)$$

where the second term vanishes if only Earth rotation is considered. Here, \mathbf{k}_{eff} represents the effective two-photon wave vector. The enclosed area of the interferometer

is $\mathbf{A} = \frac{2\hbar}{m}(\mathbf{g} \times \mathbf{k}_{eff})T^3$, giving

$$\Delta\phi = 4\mathbf{k}_{eff} \cdot (\boldsymbol{\Omega} \times \mathbf{g}) T^3 + \Delta\phi^0. \quad (7.2)$$

This represents the phase sensitivity for the Earth rotation rate measurement.

It is interesting to note that the calibration of the Earth rotation measurement only depends on the wavelength of the Raman laser, local gravity, and the pulse timing. The current Raman laser linewidth of 1 MHz gives a fractional frequency uncertainty of 3×10^{-9} , while \mathbf{g} has been measured at the 7×10^{-9} level [25], and a fast photodiode with a response time < 1 ns would give a fractional uncertainty of $< 10^{-8}$ in T . In this experiment, knowledge of the local latitude, which gives the angle between $\boldsymbol{\Omega}_E$ and \mathbf{g} , is the limiting factor. A position uncertainty of 10 m at a latitude of 37.421° gives a relative calibration uncertainty of $\sim 2 \times 10^{-6}$. However, this could be mitigated by measuring $\boldsymbol{\Omega}_E$ at the equator where the interferometer phase is only second-order sensitive to uncertainty in $\theta_{latitude}$, opening the possibility for a very sensitive measurement of the Earth rotation rate with an intrinsic calibration of better than 1 part in 10^8 . Conversely, the atom interferometer could be used to determine the direction of local \mathbf{g} relative to $\boldsymbol{\Omega}_E$ away from the equator, making it a useful tool for geodesy.

Since \mathbf{k}_{eff} is restricted to be in the horizontal plane, the maximum rotational sensitivity occurs when \mathbf{k}_{eff} is oriented East-West, where

$$\Delta\phi = 4k_{eff}g\Omega T^3 \cos(\theta_{latitude}). \quad (7.3)$$

For this experiment, $k_{eff} = 2 \times 2\pi/(852\text{nm})$, $g = 9.7994 \text{ m/s}^2$ [93], $T = 0.0515 \text{ s}$, and $\theta_{latitude} = 37.421^\circ$, so $4k_{eff}gT^3 \cos(\theta_{latitude}) \approx 6.3 \times 10^4 \text{ rad}/(\text{rad/s})$. The maximum expected interferometer phase shift due to the Earth's rotation rate is therefore 4.57 rad.

The rotation sensitivity is fundamentally limited by the detection system SNR and interferometer contrast, which determines how well the interferometer fringe can be resolved. For 5×10^6 atoms and 30% fringe contrast, the anticipated shot noise limited performance is $4 \times 10^{-8} \text{ rad/s}/\sqrt{\text{Hz}}$ ($140 \mu\text{deg}/\sqrt{\text{hr}}$). In practice, however,

the rotation rate measurement is often limited by vibrations or other sources of phase noise. Two important factors in improving the rotation sensitivity have been achieving greater fringe contrast and eliminating contributions from multiple interfering paths. Additionally, controlling and compensating for high frequency vibrational noise has proved critical to the performance of the atom interferometer.

7.2 Contrast

While atom shot noise determines how well the relative atomic state populations can be resolved, the interferometer contrast determines what fraction of those atoms contributes a meaningful signal. Decoherence in the atomic ensemble due to inhomogeneities in the optical driving fields can reduce the overall fringe contrast, limiting the phase sensitivity of the interferometer. For example, standing waves or variations in the intensity profile of the Raman beams can lead to spatially dependent Rabi frequencies, which are randomly sampled by the atoms depending on their relative positions. Also, the finite temperature of the atomic ensemble causes different velocity classes to experience different frequency detunings of the Raman pulse due to Doppler shifts. This effect is minimized if the frequency bandwidth of the Fourier-transform of the laser pulse is much larger than the velocity spread of the atom cloud.

The intensity profile of the Raman beam was characterized using a Photon-Inc. laser beam profiler. The Raman beam is initially collimated using a Micro Laser Systems (FC20-850-T/A) fiber collimator, and a two lens telescope expands the beam to $r_{1/e} = 6$ mm. A large diameter beam is desired so that the intensity is uniform over the atom cloud; however, clipping on the 0.7 in. window aperture of the vacuum cell causes diffraction that leads to large variations in the intensity profile. The beam is apertured at 2/3 of the 1/e radius, and apodized using a spatial filter to eliminate the high frequency components that migrate toward the center of the beam more quickly. This limits the intensity variations in the beam over the 80 cm travel distance. The resulting beam profile is shown in fig. 7.1.

Optical standing waves in the Raman beam can also degrade contrast through variations in the Rabi frequency. They can arise from back-reflections off of the

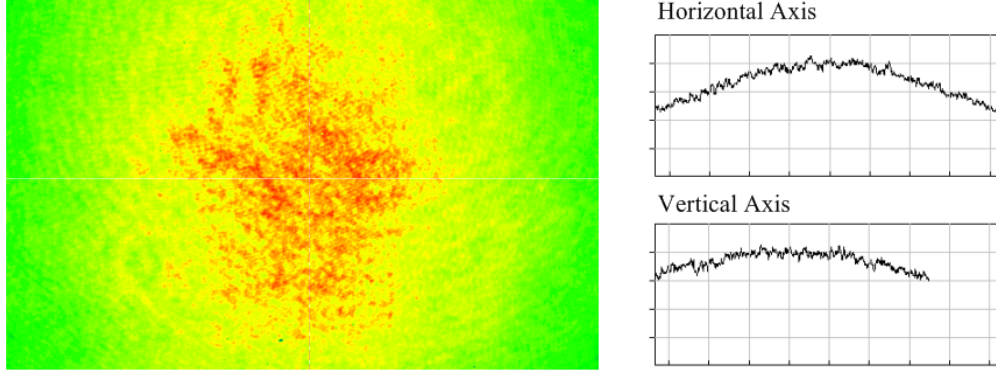


Figure 7.1: Intensity profile of the Raman beam. The beam is apertured at $\frac{2}{3}r_{1/e}$, and apodized to reduce clipping on the vacuum cell.

vacuum chamber windows, or from imperfect polarizations of the counter-propagating Raman beams. In this experiment, Raman transitions are driven with crossed linear polarizations. The incoming beam is linearly polarized with an extinction ratio of > 40 dB using a Polarcor glass polarizer. A quarter waveplate is used to compensate for changes in the polarization due to the Raman window by minimizing Doppler-free transitions in the atoms. The beam is then circularized to $\sim 99\%$ using two more quarter waveplates before the retro-reflecting mirror. The 1% linear component of the light comes back with the same polarization as the initial input light, creating a partial standing wave.

The velocity spread of the atomic ensemble also affects the interferometer contrast. The frequency detuning of the Raman beams depends on the Doppler shift, which varies for different velocity classes. If the frequency bandwidth of the Fourier-transform of the Raman pulse is much larger than velocity spread, then the pulse will drive transitions more uniformly across the entire velocity distribution.

Shorter laser pulses correspond to greater Rabi frequencies. For most atom interferometry experiments, the Rabi frequency is limited by the available laser power. In this experiment, the TAs provide enough power to drive $< 5 \mu\text{s}$ Raman pulses. However, because the Doppler shift from the horizontal velocity of the atoms is only

± 100 kHz, pulses much shorter than $\sim 10 \mu\text{s}$ can drive transitions along both directions, causing some of the atoms to receive a momentum recoil in the wrong direction. This hurts the interferometer contrast, and therefore longer pulses are desired. At the same time, longer pulses lead to reduced pulse areas for the atoms at the edges of the velocity distribution, and consequently faster dephasing within the ensemble. A colder initial atom distribution would allow for the use of longer pulses without sacrificing contrast due to velocity selection.

One way to select a narrow velocity distribution of atoms is to aperture the detection photodiode so that it only images atoms in the center of the cloud. Because of ballistic expansion, the final positions of the atoms within the cloud are correlated with their velocities. A 1.75 mm mask on the detection photodiode reduces the effective atom temperature from $2 \mu\text{K}$ to $0.5 \mu\text{K}$, as shown in fig. 7.2. The atom temperature is measured by scanning the frequency of a narrow, velocity selective Raman pulse. With the apertured detection, four-pulse contrasts of up to 30% have been observed.

7.3 Multiple Interfering Paths

In the four-pulse gyroscope sequence, inefficiencies in the Raman π -pulses can lead to the formation of additional interferometer loops that contribute to the interference signal, as discussed in section 4.3.2. These extra paths have different acceleration and rotation sensitivities than the main interferometer loop, and lead to amplitude noise on the interferometer fringes. In this section, multiple path interference is experimentally demonstrated, and a scheme for eliminating the undesired contributions is implemented and discussed.

The contributions from the multiple interfering paths are characterized using the ellipse fitting technique described in section 8.2.1. Plotting the phase outputs of two atom interferometers parametrically forms an ellipse, where the differential phase is given by ellipticity. Common phase noise only affects where a particular data point lies on the ellipse, which makes this technique ideal for differential phase measurements in the presence of large phase noise contributions.

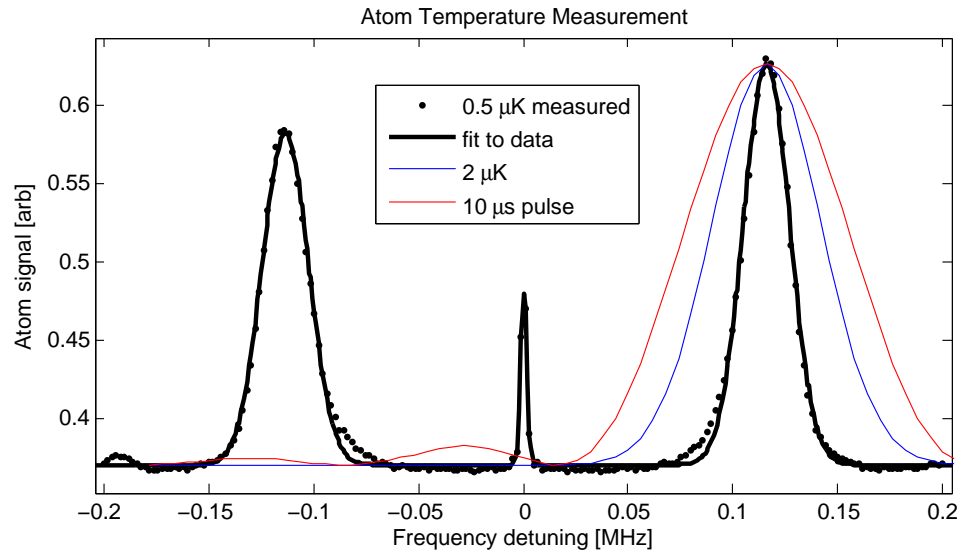


Figure 7.2: A measurement of the effective atom temperature using velocity selective Raman transitions. The measured temperature, shown in black, is limited to $0.5 \mu\text{K}$ by the detection aperture. The two large peaks arise from opposite pairs of counter-propagating Raman frequencies, while the small peak at zero detuning arises from residual Doppler-free transitions due to imperfect Raman beam polarizations. The approximate actual temperature of the full atomic ensemble is shown in blue. The red trace shows the frequency bandwidth of a $10 \mu\text{s}$ transform-limited Raman pulse.

The normalized outputs of the two interferometers are assumed to have the form

$$\begin{aligned} S_A &= \alpha \cos(\Delta\phi_{\text{rot}}) + \beta \cos(\Delta\phi_g) \\ S_B &= \alpha \cos(\Delta\phi_{\text{rot}} + \delta\phi_{\text{rot}}) + \beta \cos(\Delta\phi_g + \delta\phi_g), \end{aligned} \quad (7.4)$$

where $\Delta\phi_{\text{rot}}$ and $\Delta\phi_g$ are the phases of the main interferometer loop and the extra acceleration sensitive loops, and $\delta\phi_{\text{rot}}$ and $\delta\phi_g$ are constant phase offsets between the two interferometers due to things such as magnetic field gradients. In general, $\delta\phi_{\text{rot}} \neq \delta\phi_g$ because the paths for the main loop and extra loops are different.

Both fringe contributions have the same periodicity when the phase of the final pulse is swept. Thus, if both components are in phase, then the relative amplitudes α and β do not matter. However, because the extra loops are sensitive to constant accelerations, small tilts will shift $\Delta\phi_g$ relative to $\Delta\phi_{\text{rot}}$, causing a change in the apparent overall phase.

A simulation showing the effect of the relative amplitude of the extra loops is shown in fig. 7.3. As β/α is increased, the ellipse phase begins to smear out. The direction in which the ellipses smear out depends on the relative phase $\delta\phi_g$, as shown in fig. 7.4. An experimental demonstration of the multiple path interference is shown in fig. 7.5. As the π -pulse efficiencies are decreased, more atoms leak into the extra paths that are sensitive to constant accelerations, blurring the output phase in the presence of acceleration noise.

The multiple path interference is eliminated by shifting the timing of the two π -pulses by a small amount δT , so that the four pulses are applied at $t = 0, T + \delta T, 3T + \delta T$, and $4T$. This leads to a slight asymmetry in the trajectories of the main loop, but the two paths still spend equal amounts of time in each momentum state so that they overlap at the end of the interferometer sequence. On the other hand, for the two extra loops, one path spends a time $T + \delta T$ in a particular momentum state while the other path spends a time $T - \delta T$ in the same momentum state, leading to a spatial separation of $2v_{\text{rec}}\delta T$ between the two paths. If this separation is larger than the coherence length of the atomic wavepacket, which is typically on the order of tens of nanometers, then there will be no interference and the contributions from the extra

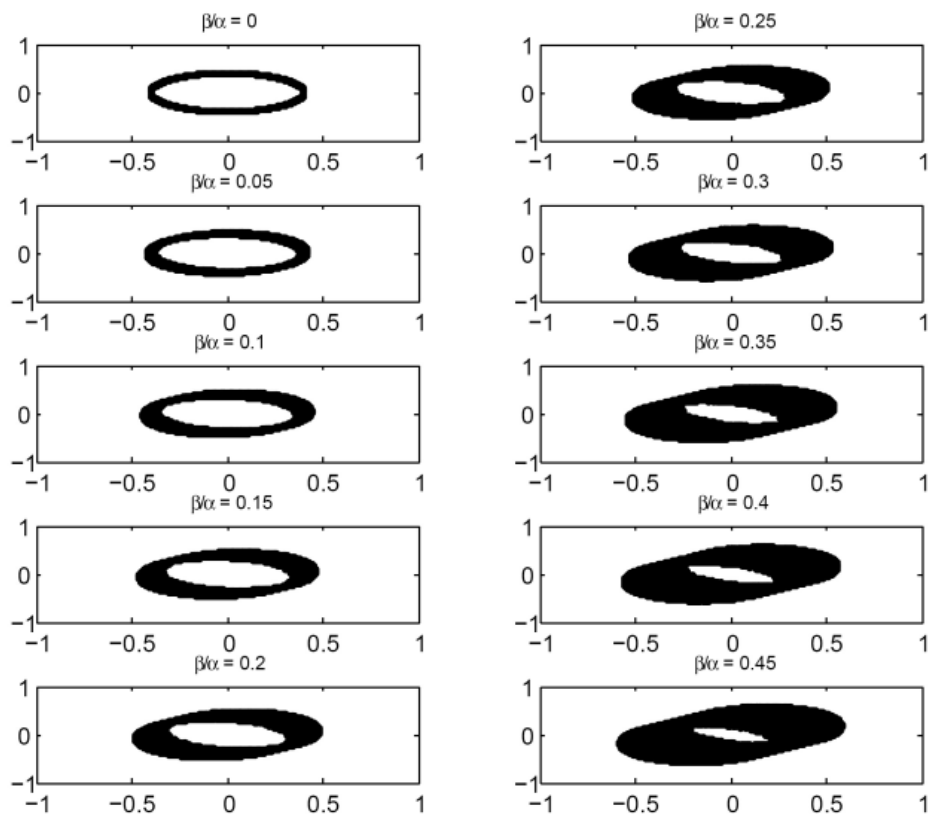


Figure 7.3: Simulation of ellipses resulting from multiple path interference for different relative amplitudes.

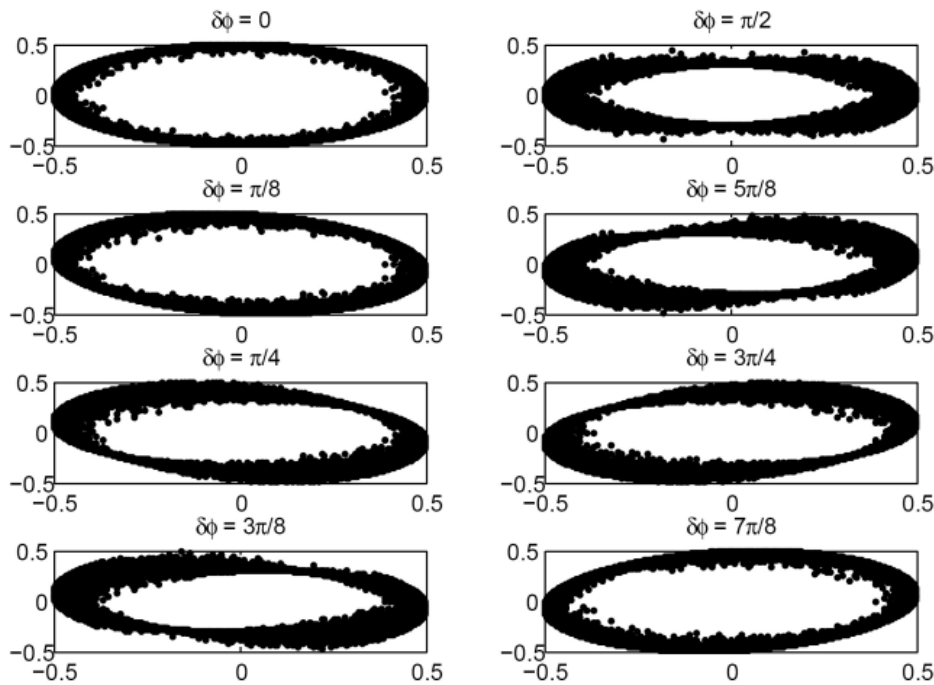


Figure 7.4: Simulation of ellipses resulting from multiple path interference for different relative phases.

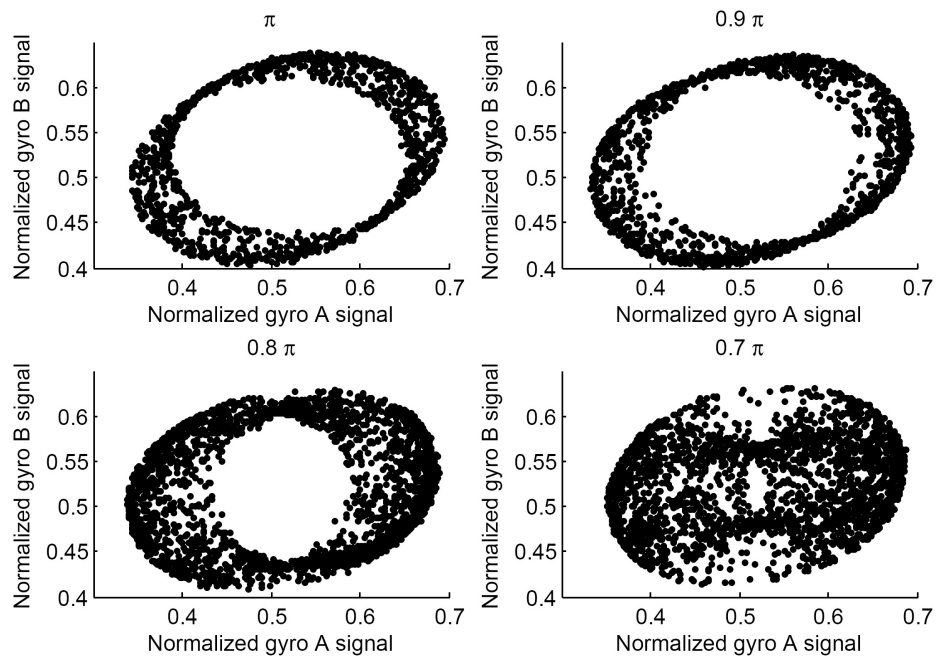


Figure 7.5: Ellipses showing contributions from multiple interfering paths. As the efficiencies of the π -pulses decrease, the phase contributions from the extra paths increase.

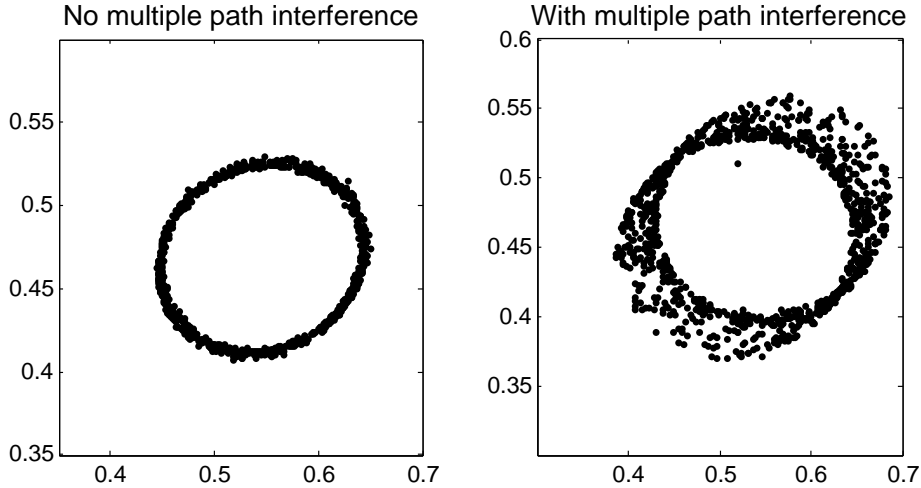


Figure 7.6: Elimination of multiple path interference. The ellipse on the left demonstrates the performance of the gyroscope when contributions from the extra interference loops are removed by modifying the timing of the laser pulses. The right plot shows the same ellipse before removing the multiple path interference.

loops will disappear. In this experiment, a time delay of $\delta T = 15 \mu\text{s}$ is inserted, giving a spatial separation of 210 nm between the two paths, which is enough to eliminate interference in the extra loops. Ellipses demonstrating the elimination of the multiple path interference are shown in fig. 7.6.

One consequence of breaking the time symmetry of the four-pulse sequence is that it opens up the main interferometer loop to a small acceleration sensitivity of $\Delta\phi = 4\mathbf{k}_{eff} \cdot \mathbf{g}\delta TT$. However, because $\delta T \ll T$, the acceleration sensitivity is suppressed by a factor of 10^4 as compared to the three-pulse accelerometer sequence. This residual acceleration sensitivity can, in principle, be eliminated completely by also adjusting the angles of the Raman wave vector at each laser pulse to tune the direction of the momentum recoils.

7.4 Measurement of the Earth's Rotation Rate

The Earth's rotation rate $\Omega_E = 7.2921 \times 10^{-5}$ rad/s gives the largest phase shift when the Raman beams are oriented East-West, such that the area vector \mathbf{A} points North-South. At the latitude of the lab ($\theta_{latitude} = 37.421^\circ$), the expected phase shift from Ω_E is

$$\Delta\phi = 4k_{eff}g\Omega_E T^3 \cos(\theta_{latitude}) \sin(\vartheta) = 4.57 \text{ rad} \times \sin \vartheta, \quad (7.5)$$

where ϑ is the angle between \mathbf{k}_{eff} and North.

To measure Earth rotation rate as a function of the orientation, the atom interferometer was placed on a rotating turntable. The turntable was leveled to within 100 μ rad using an Applied Geomechanics (755-1129) tiltmeter in order to minimize any systematic effects that may arise from a change in the atom launch angle. The phase was measured at 5° intervals from -120° to 120° . Each point is an average of five phase measurements, which are obtained by sweeping over five interferometer fringes in 100 points and performing a least squares sine fit with the amplitude constrained to match the interferometer contrast. The sensor was placed on Sorbothane pads and the turntable was locked down using four posts at each measurement position to minimize vibrationally-induced phase noise.

The results of the turntable measurement are shown in fig. 7.7. The predicted curves shown are one parameter fits using the actual rotation rate of the Earth, with the phase offset being the only variable. The interferometer phase traces out a sine curve with respect to the Raman beam orientation as expected, with the detected rotation rate going to zero at North-South. The typical noise for each phase measurement is several hundred mrad, and is limited by multiple path interference, which was not eliminated prior to this experiment. The multiple path interference also leads to long-term drifts in the phase since the extra paths are sensitive to accelerations, and the Sorbothane allows the sensor to sag, changing the projection of vertical gravity along \mathbf{k}_{eff} . This limits the accuracy of Ω_E as determined by fitting the amplitude of the sine curve to $\sim 1\%$.

A second measurement of the Earth rotation rate was performed once the multiple interfering paths were eliminated. For this measurement, the atom interferometer was

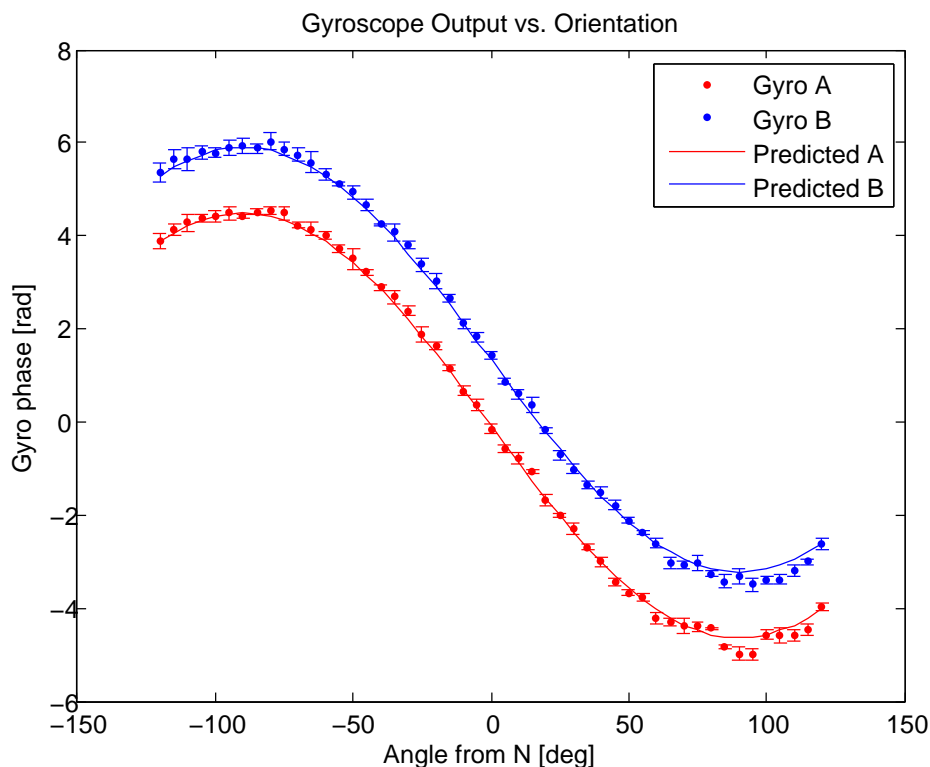


Figure 7.7: Changing projection of Earth rotation rate. The component of the Earth rotation rate measured by the atom interferometer is given by $\boldsymbol{\Omega}_E \cdot \mathbf{A}$, which depends on the orientation of the Raman beam axis. The maximal signal is obtained when the Raman beams are oriented East-West, such that \mathbf{A} points North-South.

oriented to be maximally sensitive to Ω_E , and the signal was integrated over a total of 50 hours. Once again, the fringes were scanned over 100 points, but the direction of \mathbf{k}_{eff} was alternately reversed by chopping the Raman beam frequency difference between $\Delta\nu = \Delta\nu_{HFS} \pm \mathbf{k} \cdot \mathbf{v}$, so that the opposite pairs of frequencies would be Doppler shifted into resonance. When \mathbf{k}_{eff} is reversed, the rotation signal changes sign but many other systematic effects remain unchanged, suppressing many potential sources of long-term drift in the differential signal. This type of wave vector reversal could also benefit the accelerometer and gravity gradiometer operation modes of the atom interferometer, as the acceleration signals also change sign along with \mathbf{k}_{eff} .

The raw interferometer phase for both directions of \mathbf{k}_{eff} are shown in fig. 7.8, along with the phase difference. The individual phases for each direction display long-term drifts of a few hundred mrad on the time-scale of several hours. The chirped frequency of the oscillations may indicate that the phase fluctuations arise from an etalon-like effect in the final window before the retro-reflecting mirror. The temperature in the sensor box typically takes a day or two of continuous operation to reach thermal equilibrium, which is consistent with the time-scales shown here. Since these drifts are independent of the direction of \mathbf{k}_{eff} , the difference phase (shown in blue) demonstrates a significant reduction in the long-term drifts.

The stability of the atom interferometer can be inferred from the Allan deviation of the rotation rate signal, as shown in fig. 7.9. The green and red traces represent the measured phase for each of the two Raman wave vector directions, and the blue trace shows the difference. The black lines show the $1/\sqrt{\tau}$ scaling of the Allan deviation expected for white noise limited performance.

The standard deviation of the phase measurements for each of the two directions over short time-scales is ~ 50 mrad per 100 points, which corresponds to a rotation rate uncertainty of 8×10^{-7} rad/s. The short-term noise is characterized by an ARW of 7×10^{-6} rad/s/ $\sqrt{\text{Hz}}$ (23 mdeg/ $\sqrt{\text{hr}}$), and is dominated by high frequency position jitter in the Raman retro-reflecting mirror. The short-term sensitivity of the difference signal starts off a factor of $\sqrt{2}$ better than the individual measurements because the noise is uncorrelated between successive scans.

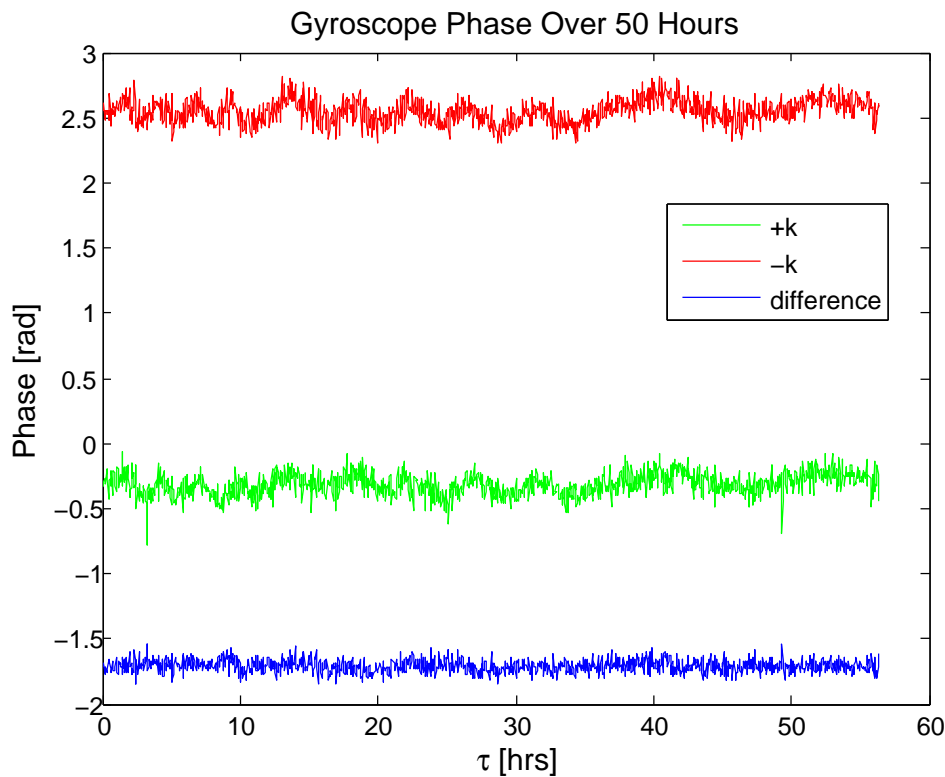


Figure 7.8: The atom interferometer phase measured over 50 hours. Raman wave vector reversal allows for the suppression of noise sources that are independent of the direction of \mathbf{k}_{eff} .

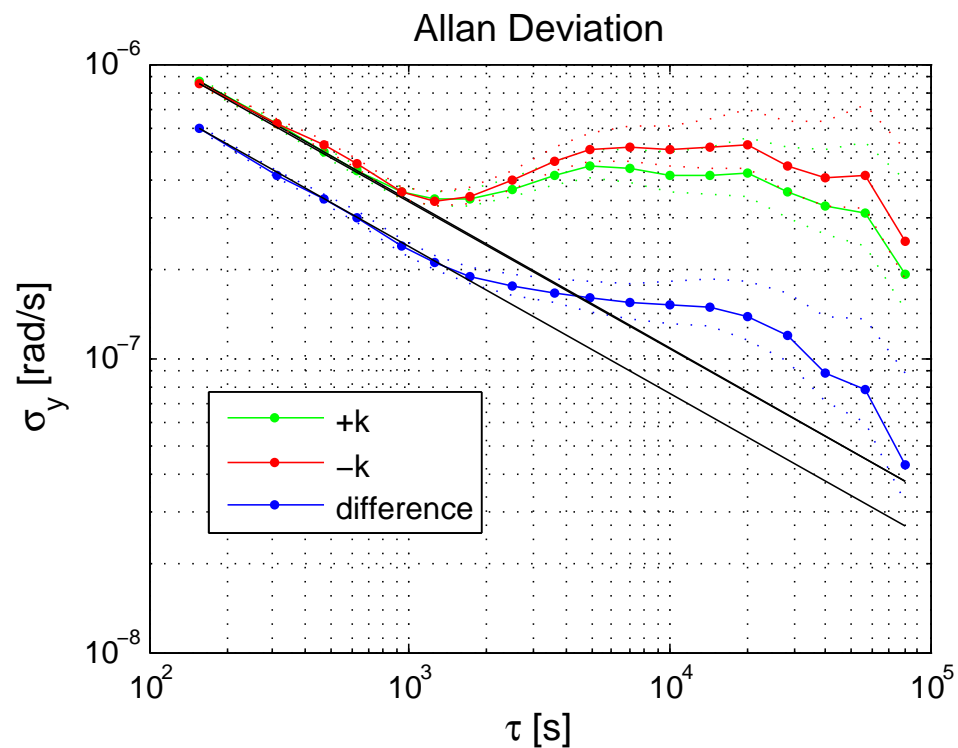


Figure 7.9: Allan deviation of the Earth rotation rate measurement. Raman wave vector reversal suppresses the hour time-scale drifts that otherwise limit the performance of the interferometer.

Both the individual and difference phases begin to deviate from white noise limited performance at time-scales of about an hour due to the oscillations seen in fig. 7.8. The difference signal is able to suppress much of this drift, integrating down to $4 \times 10^{-8} \text{ rad/s} \approx 5 \times 10^{-4} \Omega_E$ at $8 \times 10^4 \text{ s}$. This represents a factor of 5 improvement in the long-term stability over the single direction signals. The maximum integration time is currently limited to ~ 50 hours by the intermittent nature of the vibration noise of the laboratory floor. During the daytime on weekdays, the vibration noise is significantly worse than at nighttime or on weekends, making it impractical to take more than one weekend of consecutive data. A longer data run on a more vibrationally quiet platform is currently being planned.

The mean rotation rate given by the difference signal is $7.2972 \times 10^{-5} \text{ rad/s}$. In terms of the actual value for the Earth's rotation rate, the measured rate is $\Omega/\Omega_E = 1.0007 \pm 0.0005$. Because of the wave vector reversal, many systematic shifts such as stray magnetic fields and residual ac Stark shifts cancel out. The absolute calibration of the measurement is limited by knowledge of $\theta_{latitude}$ at a few parts in 10^6 .

7.5 Vibration Compensation

The phase sensitivity of the atom interferometer in the absence of vibrational noise is determined by the detection system SNR and the fringe contrast. For the current performance of the four-pulse rotation measurement, the SNR is 500 : 1 and the contrast is 20%, giving a noise floor of $\sim 10 \text{ mrad/shot}$, as opposed to the $\sim 400 \text{ mrad/shot}$ observed with vibrations. This would correspond to a rotation rate sensitivity of $1.3 \times 10^{-7} \text{ rad/s}/\sqrt{\text{Hz}}$, without any further improvements to the atom interferometer.

While the four-pulse gyroscope sequence cancels out phase contributions from constant accelerations, it is still sensitive to vibrational noise at frequencies above $1/T$. Jitter in the retro mirror position gives rise to a phase shift

$$\Delta\phi^0 = \mathbf{k}_{eff} \cdot (\delta\mathbf{x}(0) - 2\delta\mathbf{x}(T) + 2\delta\mathbf{x}(3T) - \delta\mathbf{x}(4T)). \quad (7.6)$$

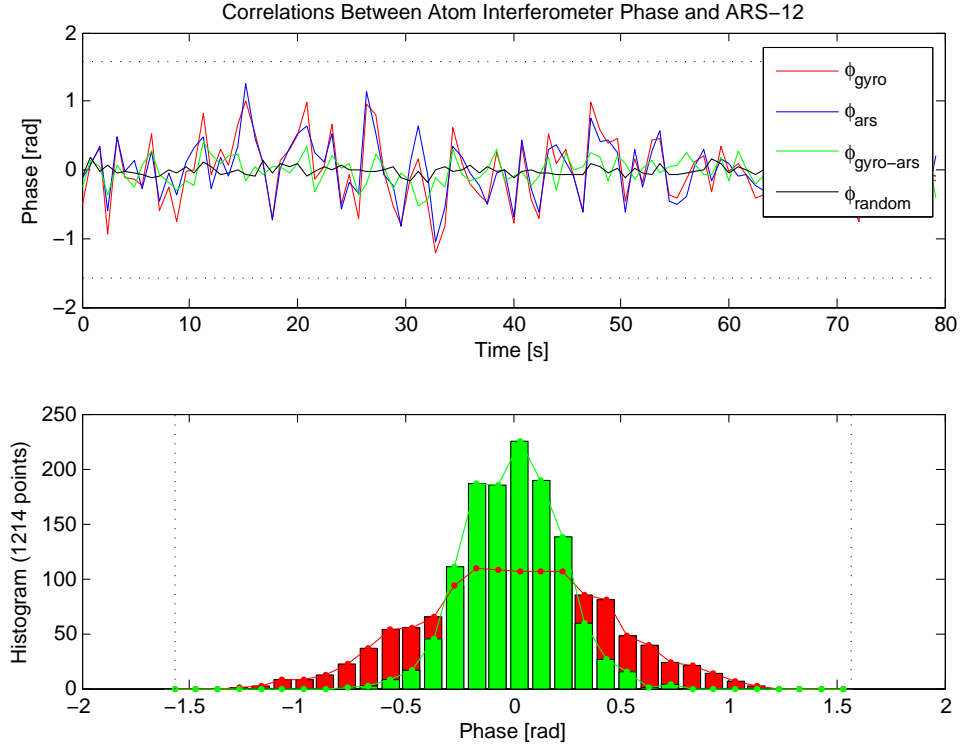


Figure 7.10: Correlations between atom interferometer phase and ARS-12. Monitoring and compensating for high frequency position jitter in the Raman mirror reduces the short-term phase noise by 40 – 50%.

This phase shift, which appears as noise on the rotation rate signal, could be eliminated by tracking the position of the mirror as a function of time using conventional inertial sensors. Because the position only needs to be tracked throughout a single interferometer cycle, the typically large long-term drifts associated with conventional inertial sensors do not matter.

As a demonstration of this vibration phase noise reduction technique, an Applied Technology Associates (ARS-12) MHD gyroscope is used to monitor the high frequency vibrations of the retro-reflecting mirror, and the integrated position jitter is subtracted from the measured interferometer phase. The results are shown in fig. 7.10.

The interferometer is set on the side of a fringe, where the signal is approximately

linear in phase. The high frequency position jitter correlates with the phase noise of the interferometer at the 40 – 50% level. Currently the ARS-12 is only monitoring angular rotations along one axis, and not linear accelerations. Implementing this scheme with multiple sensors monitoring rotations and linear accelerations along all three axes may allow for operation of the atom interferometer at the fundamental sensitivity limit.

Chapter 8

Accelerometry and Gravity Gradiometry

Atom interferometers are very versatile because the Raman pulse sequence can be tailored to make the atomic phase sensitive to a variety of inertial and gravitational effects. The single retro-reflected Raman beam scheme allows the atom interferometer to be configured as a sensitive accelerometer/gravimeter or gravity gradiometer, in addition to a gyroscope. A compact atom interferometer system capable of rotation, acceleration, and gravity gradient measurements would represent a step toward the development of an inertial navigation unit with unprecedented sensitivities and accuracies [42, 94]. In this chapter, the sensitivity of the atom interferometer to inertial and gravitational accelerations is discussed, and its performance is characterized by measuring the differential acceleration due to the gravitational field of a test mass.

8.1 Acceleration Measurements

The three pulse $\frac{\pi}{2} - \pi - \frac{\pi}{2}$ interferometer sequence is sensitive to accelerations, with a phase shift given by

$$\Delta\phi = \mathbf{k}_{eff} \cdot \mathbf{g} T^2 + \frac{2m}{\hbar} \boldsymbol{\Omega} \cdot \mathbf{A} - \mathbf{k}_{eff} \cdot (\boldsymbol{\Omega} \times \mathbf{g}) T^3 + \Delta\phi^0, \quad (8.1)$$

where the $\mathbf{k}_{eff} \cdot (\boldsymbol{\Omega} \times \mathbf{g}) T^3$ term disappears if only Earth rotation is considered. Launching the atoms such that the π -pulse occurs at the peak of the trajectory leads to a symmetric “figure 8” geometry where the enclosed area \mathbf{A} vanishes, giving

$$\Delta\phi = \mathbf{k}_{eff} \cdot \mathbf{g}T^2 + \Delta\phi^0. \quad (8.2)$$

The first term represents the phase shift from a constant acceleration over the full interferometer sequence, while the second term represents fluctuations in the laser phase. For the Raman beam configuration considered here, the position of the retro-reflecting mirror determines the effective laser phase, so that acceleration measurements in a single atom interferometer are sensitive to high frequency vibration noise of the Raman mirror in addition to constant accelerations. In order to measure the constant acceleration, the phase contribution from $\Delta\phi^0$ must be smaller than π radians or the interferometer fringes will wash out.

Acceleration measurements were made with the interferometer placed directly on the lab floor. The Sorbothane pads were removed from under the sensor legs to prevent changes in the interferometer tilt. This is critical as the phase shift $\Delta\phi = k_{eff}g \sin \theta + \Delta\phi^0$ is first-order sensitive to small tilts θ , with a large phase sensitivity of ~ 15 rad per 1 μ rad tilt. Interferometer fringes were obtained by scanning the phase of the final $\frac{\pi}{2}$ -pulse. Typical accelerometer fringes for $T = 105$ ms are shown in fig. 8.1.

The noise on the fringe signal is due to position jitter in the Raman retro-reflection mirror resulting from floor vibrations. The additional phase for each acceleration measurement is given by

$$\Delta\phi^0 = \mathbf{k}_{eff} \cdot (\delta\mathbf{x}(0) - 2\delta\mathbf{x}(T) + \delta\mathbf{x}(2T)) \quad (8.3)$$

where $\delta\mathbf{x}(t_i)$ represents the deviation in the mirror position from a constant acceleration. The typical shot-to-shot noise on the acceleration measurements is 300 mrad ($\sim 1.6 \times 10^{-7}$ g/ $\sqrt{\text{Hz}}$) at nighttime, and over 1 rad during the day.

In the absence of vibrational noise, the expected noise floor of the accelerometer is given by the detection system SNR and interferometer contrast. The detection system

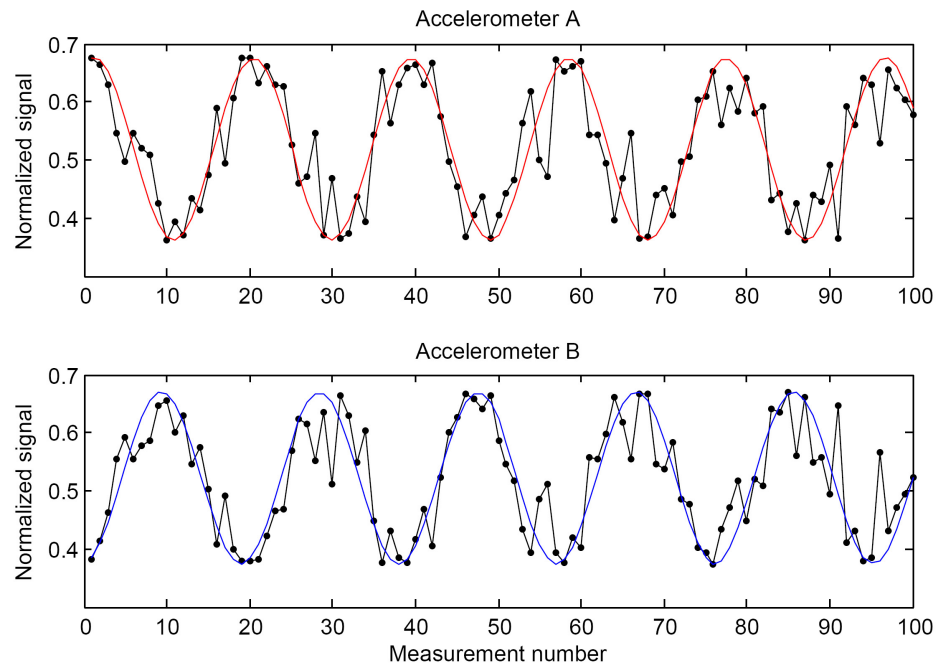


Figure 8.1: Typical accelerometer fringes. The phase of the final pulse of a $\frac{\pi}{2} - \pi - \frac{\pi}{2}$ interferometer sequence is scanned to produce the fringes. The shot-to-shot phase noise induced by vibrations in the lab floor is typically several hundred mrad at night and on weekends, and over 1 rad during the day.

has demonstrated SNRs of $> 800 : 1$, and interferometer contrasts of up to 60% have been obtained for the three-pulse sequence discussed here, giving an inferred phase uncertainty of ~ 2 mrad/shot. For a $T = 105$ ms interferometer, this corresponds to an acceleration sensitivity of 1.1×10^{-9} g/ $\sqrt{\text{Hz}}$. The anticipated shot noise limited performance of the accelerometer for 5×10^6 atoms is 8×10^{-10} g/ $\sqrt{\text{Hz}}$. As with operation in gyroscope mode, using conventional inertial sensors to monitor high frequency position jitter in the retro-reflecting mirror could help bring the accelerometer performance closer to the noise floor of the interferometer.

8.2 Gravity Gradiometry

Differential accelerometry or gravity gradiometry is useful in many mobile applications where vibrations can severely limit the performance of the atom interferometer. The outputs of two spatially separated interferometers sharing a common Raman beam can be differenced in order to eliminate noise due to phase fluctuations in the Raman laser. Any constant gravitational or inertial accelerations that are common to both interferometers also cancel out, leaving only the differential acceleration due to the gradient of the gravitational field.

Gravity gradiometry is essential in inertial navigation as acceleration measurements must be compensated for gravitational variations due to nearby masses. According to the equivalence principle, it is not possible to locally distinguish inertial accelerations from gravitational accelerations; however, by measuring the gradient of the gravity field over a region of space, the gravitational field can be reconstructed and subtracted out to determine the true inertial acceleration. For a detailed description of a long baseline mobile atom interferometer gravity gradiometer, see [90].

The retro-reflected Raman beam scheme considered in this experiment, unlike other gravity gradiometer configurations, allows for the simultaneous measurement of both the differential and absolute accelerations of the two atomic ensembles, making this system particularly useful for navigation applications.

8.2.1 Ellipse Fitting

In environments where phase shifts due to acceleration noise are $> \pi$ rad, the 2π phase ambiguity makes it impossible to determine the individual accelerometer phases directly. However, because both interferometer signals are sine functions sharing the same phase fluctuations, they can be plotted parametrically to reveal the differential phase in the presence of the large common noise. This ellipse fitting technique has been described in detail in [95].

The two interferometers are assumed to have outputs of the form

$$\begin{aligned} x &= A' \sin(\phi) + B' \\ y &= C' \sin(\phi + \Delta\phi_g) + D', \end{aligned} \quad (8.4)$$

where $\Delta\phi_g$ is the constant gravity gradient, and ϕ is the common phase that varies from shot to shot. Plotting the two outputs parametrically gives the shape of an ellipse, with $\Delta\phi_g$ determining the ellipticity, and ϕ determining where on the ellipse the point lies. Figure 8.2 shows simulated data demonstrating the ellipse fitting technique. The ellipse on the left is for two pure sine waves with a constant differential phase of 1 rad, while the ellipse on the right is for the same fringes with 5 rad of white phase noise added to both interferometer signals. Even though the individual accelerometer phases are indeterminable because of the added noise, the differential phase can be measured with the same accuracy.

While the simplicity of ellipse fitting makes it appealing, phase calculations using this process are not optimal. Because the ellipse samples points with random phases and not just those with the maximum phase sensitivity, it is inherently less sensitive than measuring phase fluctuations on the side of an interferometer fringe by a factor of $2/\pi$. Also, the ellipse fitting algorithm used is particularly susceptible to outliers, which can lead to a further reduction in phase sensitivity. The ultimate performance of an atom interferometer gradiometer could benefit from improved phase estimation techniques using Bayesian logic that leverage experimental knowledge of the system noise [96].

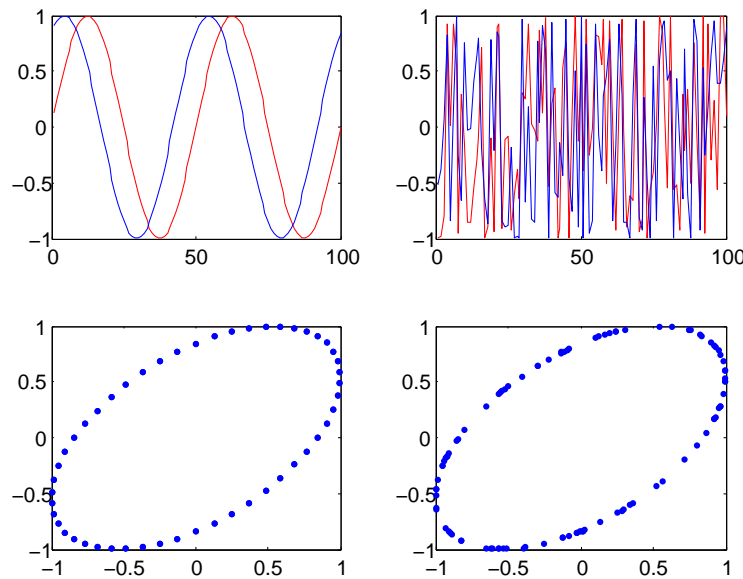


Figure 8.2: Ellipse fitting technique. The differential phase between two interferometers can be determined even in the presence of large amounts of common phase noise by measuring the ellipticity of the ellipse formed by plotting the two outputs parametrically. The ellipse on the left is for two pure sine waves, while the ellipse on the right is for two noisy interferometer fringes.

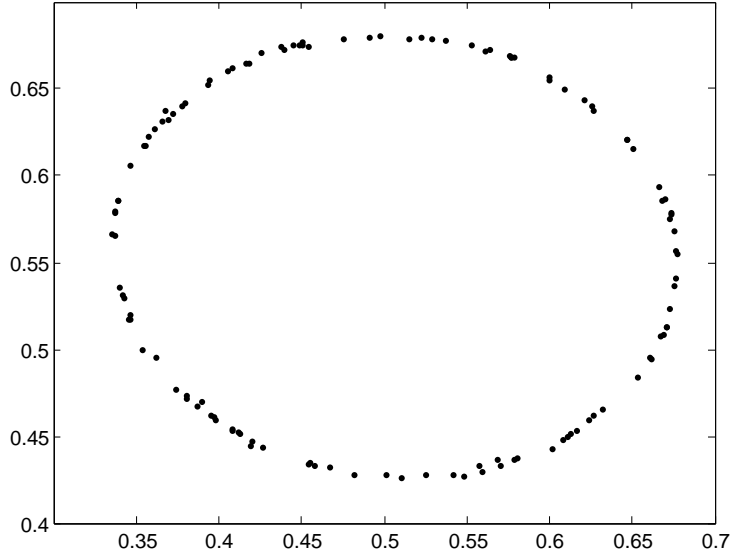


Figure 8.3: Example of a low noise interferometer ellipse. The phase is calculated for each set of 20 data points, and the variation in the phase measurements reflects the noise floor of the system. The phase noise as determined by these ellipses is 2.3 mrad per 20 point ellipse.

8.2.2 Gradiometer Performance

The short-term noise performance of the atom interferometer in gradiometer mode is determined from the ellipses. The phase noise is measured by dividing the data into bins of equal numbers of points, and extracting the differential phase by fitting an ellipse to each set of points. The bin size is varied to minimize the inferred shot-to-shot phase fluctuations. In this experiment, the ellipse fitting is typically performed over 20 point intervals.

An ellipse demonstrating exceptionally low noise is shown in fig. 8.3. The fluctuations in the successive ellipse phase measurements are 2.3 mrad per 20 point ellipse. The inferred shot-to-shot noise in the gradient signal over the 0.2 m gradiometer baseline is $270 \text{ E}/\sqrt{\text{Hz}}$ ($1 \text{ E} \approx 10^{-10} \text{ g/m}$). Meanwhile, the anticipated noise floor for shot noise limited performance with 5×10^6 atoms and 60% interferometer fringe contrast is $38 \text{ E}/\sqrt{\text{Hz}}$.

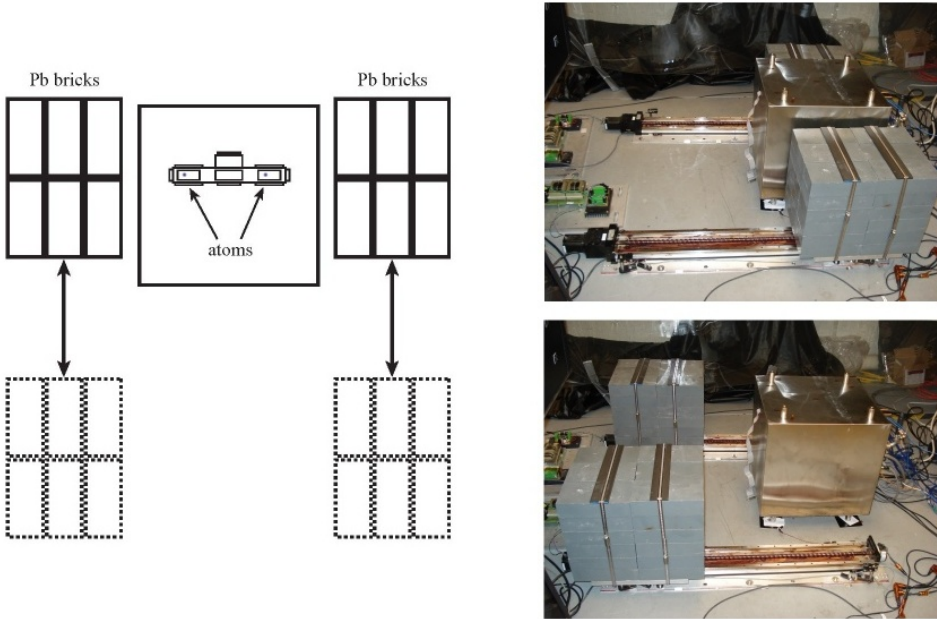


Figure 8.4: Schematic of the gradiometer mass test. The positions of the two stacks of lead bricks relative to the atoms are shown. The bricks were moved back and forth every 1000 s. The gravitational force of the bricks leads to a differential acceleration of $3 \times 10^{-8} \text{ g}$ over the 0.2 m baseline between the two atom interferometers, giving a gravitational gradient of 1500 E.

8.3 Mass Testing

To evaluate the performance of the interferometer as a gradiometer, the gravitational gradient of a test mass was measured. The test masses used were two identical stacks of 36 lead bricks, placed on either side of the atom interferometers. Each brick weighs $\sim 10 \text{ kg}$ for a total of 360 kg on either side, giving a gravity gradient of 1500 E over the 20 cm baseline of the gravity gradiometer. The bricks were repositioned every 1000 s using two stepper motors. A schematic of the brick positions is shown in fig. 8.4.

The differential phase resulting from the applied gravity gradient is determined by using the ellipse fitting technique described in the previous section. A typical ellipse consisting of 100 data points is shown in fig. 8.5. The phase is extracted by

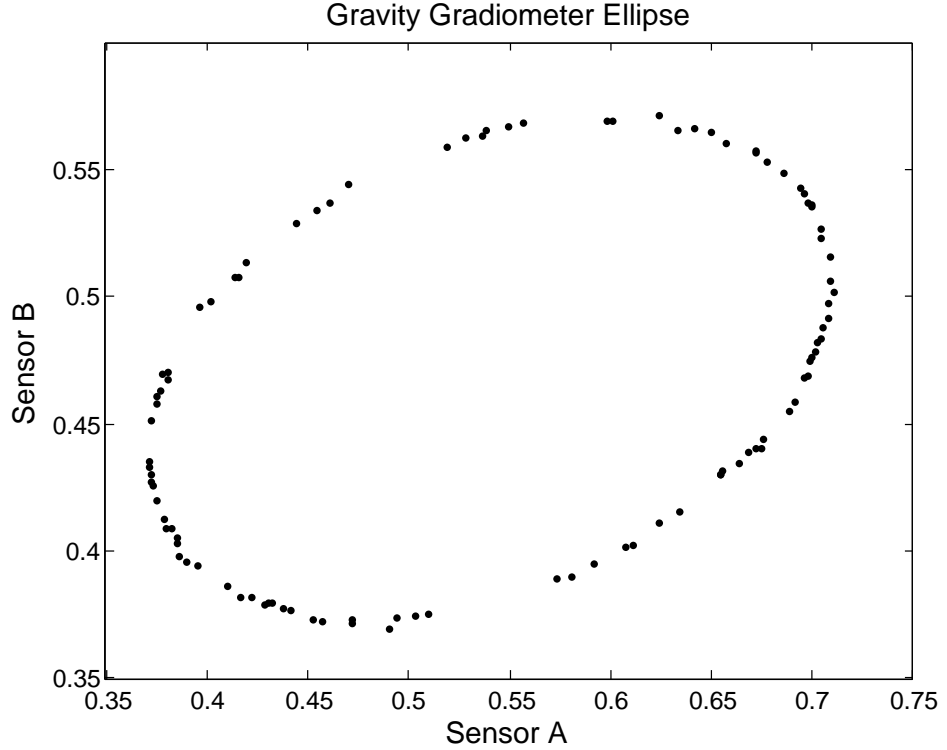


Figure 8.5: Typical gradiometer ellipse for the mass test consisting of 100 data points. The ellipticity determines the differential phase between the two parametrically plotted interferometer outputs. The phase noise as determined from the ellipse fit is ~ 7 mrad per 20 point ellipse.

fitting an ellipse for every 20 data points. The typical phase noise is ~ 7 mrad per 20 points, or ~ 30 mrad per shot, corresponding to a gradient sensitivity of $780 \text{ E}/\sqrt{\text{Hz}}$ for the 20 cm baseline. In the absence of common-mode noise, this implies a single accelerometer performance of $2.2 \times 10^{-8} \text{ g}/\sqrt{\text{Hz}}$, which is a factor of 20 away from the noise floor as expected from the detection system SNR.

One factor that could potentially improve the noise on the differential phase measurement is the linewidth of the Yokogawa DBR used as the master Raman laser. The difference between the two interferometer outputs is given by

$$\Delta\phi_A - \Delta\phi_B = \mathbf{k}_{eff} \cdot (\Delta\mathbf{x}_1 - 2\Delta\mathbf{x}_2 + \Delta\mathbf{x}_3), \quad (8.5)$$

where $\Delta x_i \approx 20$ cm is the separation between the two atomic ensembles at each laser pulse. Fluctuations in \mathbf{k}_{eff} due to frequency jitter in the Raman laser leads to phase noise proportional to the gradiometer baseline. For the ~ 1 MHz measured linewidth of the Raman laser used in this experiment, the expected phase noise is ~ 20 mrad per shot, which is close to the current noise performance of the system.

The change in the differential phase resulting from the masses is shown in fig. 8.6, along with the individual accelerometer phases. The accelerations for each atom interferometer are measured by directly fitting the fringes for every 100 points. The resulting phases change by several radians each time the bricks are repositioned. This large phase shift is attributed to the bricks weighing down the floor, causing a change in the tilt of the experimental apparatus. Because the interferometer is configured as a horizontal accelerometer, it is extremely sensitive to tilt. However, this large phase shift is common to both accelerometers, so the difference should still give the gravitational gradient induced by the lead bricks. Indeed, we see in fig. 8.6 that this is the case, as the difference of the individual accelerometer outputs matches the differential phase obtained using ellipse fitting.

The differential phase calculated by fitting the fringes is much noisier than the ellipse fitting because of the vibration noise. While the vibrations are common to both accelerometers, the noise does not easily subtract out because it is phase noise and not amplitude noise. Since there is an initial phase offset between the interferometers due to the gravity gradient, the two sensor outputs exhibit different signal responses to the same phase fluctuations. The phase noise derived from ellipse fitting is a factor of 10 smaller, implying that the performance of the individual accelerometers would improve by at least that amount in the absence of high frequency vibrations.

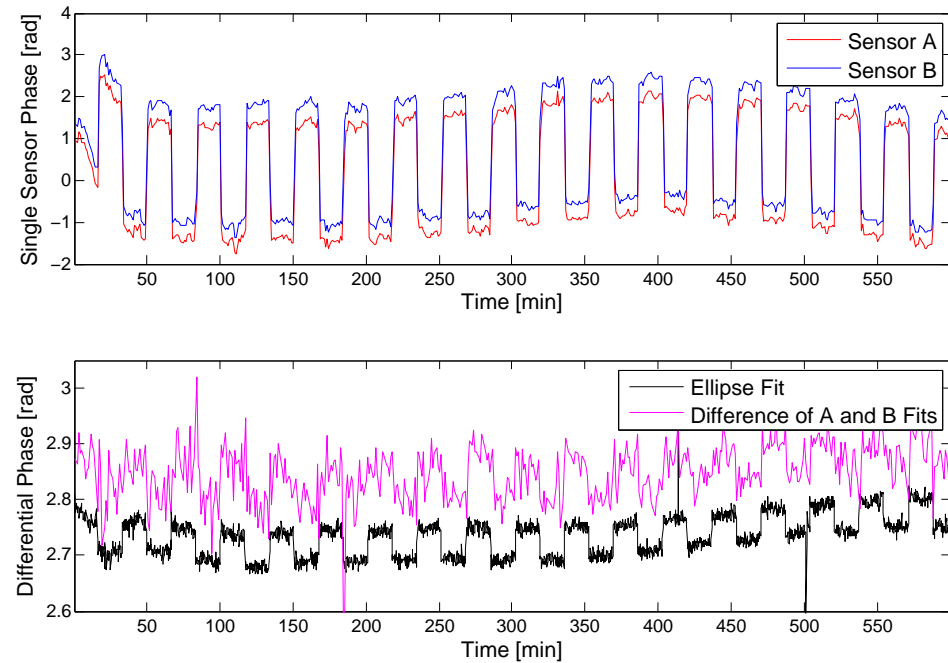


Figure 8.6: Interferometer phases for the brick chop test. The top plot shows the individual interferometer phases as determined by fitting directly to the fringe. The large phase shift is mostly due to the tilt of the floor changing as the bricks are repositioned. The bottom plot shows the differential phase as determined both by subtracting the individual phases and by ellipse fitting. A constant offset is added to make the correlations easier to see.

Chapter 9

Zero Dead Time Operation

Pulsed atom interferometers such as the one described in this experiment suffer from long-term drifts due to nonuniform coverage of the time axis. The discrete interferometer measurements sample the high frequency phase noise of the reference oscillator at the cycle repetition rate, leading to measurement errors that accumulate over time and give a random walk of the integrated signal. In this chapter, the Dick effect is introduced in the context of atomic clocks, and a zero dead time (ZDT) scheme for eliminating errors due to this effect is demonstrated in a dual atomic clock system. Also, a ZDT scheme for navigation applications is explored.

9.1 The Dick Effect in Atomic Clocks

Atomic clocks or frequency standards are a special class of atom interferometer designed to measure constant frequencies. While inertial force sensors based on atom interferometry measure the atom's position relative to an optical reference, atomic clocks measure the frequency of a local oscillator (LO) relative to the atom's internal resonance frequency. The differential frequency is evaluated by measuring the relative phase accrued over an interrogation time T . The sensitivity of atomic clocks therefore scales linearly with T .

The first Cs clocks were based on a two-pulse Ramsey sequence in a thermal beam of atoms [97]. The ultimate sensitivity of these clocks was limited by the fast atomic

velocities and vacuum cell size. The advent of laser cooling and trapping in the 1990s provided a robust source of cold atoms in the MOT, allowing for significantly longer interrogation times and much improved sensitivities. At the same time, the discrete nature of these atomic sources led to the implementation of time-domain interferometers relying on microwave or optical pulses rather than constant interaction regions. This, combined with finite atom loading and detection times, results in dead time between successive interferometer cycles.

The role of the atomic clock is to monitor and correct for phase noise in the LO by comparing it to a pristine reference (the atomic resonance frequency). During the dead time, however, the relative phase is not monitored and therefore noise can lead to an error in the corrected phase of the LO. These random errors produce a random walk of the cumulative relative phase between the LO and the atomic reference, and results in what is known as the Dick effect [98].

9.1.1 Example: the Microwave Fountain Clock

In a microwave fountain clock, atoms are interrogated using a two-pulse $\frac{\pi}{2} - \frac{\pi}{2}$ Ramsey sequence. Unlike the gyroscope where two-photon Raman transitions are used, a microwave field is applied to drive transitions between the two hyperfine ground states, giving a negligibly small momentum recoil. The differential phase for the two paths is given by

$$\Delta\phi = (\phi_1 - \phi_2) - \omega_{eg}T \quad (9.1)$$

where ω_{eg} is the hyperfine splitting, and ϕ_1 and ϕ_2 represent the local phase of the driving field at the first and second pulses. For an ideal LO operating at frequency ω_{LO} , the phase of the field picked up by the atoms for each pulse is given by

$$\phi_i = \mathbf{k} \cdot \mathbf{x}_i - \omega_{LO}t_i + \phi_i^0. \quad (9.2)$$

The position-dependent term $\mathbf{k} \cdot \mathbf{x}_i$ and arbitrary phase term ϕ_i^0 are assumed to be controllable parameters such that the differential phase becomes

$$\Delta\phi = (\omega_{LO} - \omega_{eg})T, \quad (9.3)$$

which goes to zero when the LO is tuned to the atomic resonance frequency.

In practice, the phase of the LO deviates from that of a perfect oscillator due to environmental perturbations, which can manifest as fast fluctuations in the phase or slow drifts in the average oscillation frequency. The actual LO phase is given by

$$\phi_i = \mathbf{k} \cdot \mathbf{x}_i - \omega_{LO} t_i + \phi_i^0 + \delta\phi(t_i), \quad (9.4)$$

where $\delta\phi(t_i)$ represents the deviation from a perfect oscillator at time t_i . The differential phase is therefore given by

$$\Delta\phi = \delta\phi(t_1) - \delta\phi(t_2). \quad (9.5)$$

The differential phase measurement captures the phase noise in the LO at the beginning and end of the interferometer sequence, which gives the frequency error in the LO integrated over the interrogation time. However, the interferometer does not monitor the LO phase during the dead time between successive clock measurements. The phase noise continues to accumulate until the beginning of the next interferometer sequence at t_3 , so that the total accumulated phase error over the entire cycle time T_c from t_1 to t_3 is actually $\delta\phi(t_1) - \delta\phi(t_3)$. This gives an error in the measured phase of $\delta\phi(t_2) - \delta\phi(t_3)$ that cannot be compensated for. Likewise, between the second and third interferometer cycles, there is a phase error of $\delta\phi(t_4) - \delta\phi(t_5)$. In general, for N successive interferometer cycles, the cumulative phase error for the entire time interval is

$$\Phi = \sum_{n=1}^N \delta\phi(t_{2n}) - \delta\phi(t_{2n+1}). \quad (9.6)$$

One way of characterizing clock performance is to measure the two-sample Allan

standard deviation

$$\sigma_y(\tau) = \frac{\sigma_\Phi(\tau)}{2\pi\nu_0} \frac{1}{\eta\tau}, \quad (9.7)$$

where ν_0 is the frequency being measured, $\eta \equiv T/T_c$ is the duty cycle, and $\sigma_\Phi(\tau)$ is the standard deviation of the phase error accumulated over a fixed time interval τ . There are a total of $N = \tau/T_c$ differential phase measurements over the time interval τ . Assuming no correlations between consecutive phase errors due to the dead time, then $\sigma_\Phi(\tau)$ including measurement errors is

$$\sigma_\Phi(\tau) = [N\sigma_{\Delta\phi}^2 + N\sigma_m^2]^{1/2}, \quad (9.8)$$

where $\sigma_{\Delta\phi}$ is the standard deviation of the differential phase measurements $\Delta\phi_n$, and $\sigma_m = \langle(\delta\phi^m)^2\rangle^{1/2}$ is the standard deviation in the error $\delta\phi^m$ for each measurement. The measurement noise $\delta\phi^m$ depends on technical sources as well as sensitivity, which generally scales with T . If the noise on the LO is white phase noise, then $\sigma_{\Delta\phi}$ is independent of τ , and the Allan deviation scales as

$$\sigma_y(\tau) \sim \frac{\sqrt{N}}{\tau} \sim \tau^{-1/2}. \quad (9.9)$$

In order to minimize phase errors accumulated during dead time, many atomic clock systems utilize LOs with ultra-high stability [99, 100]. By reducing high frequency ($> 1/T$) contributions to the phase noise, long-term drifts in the average oscillator frequency can still be monitored by assuming that the phase errors accumulated during the dead time are the same as the phase errors measured during the interferometer interrogation time. The use of ultra low noise LOs often sets the cost for atomic clock systems, and while they serve to decrease the rate at which these errors accumulate, they do not eliminate them completely. Other efforts to mitigate these errors have included minimizing the dead time between cycles and using continuous atomic fountains [101, 102].

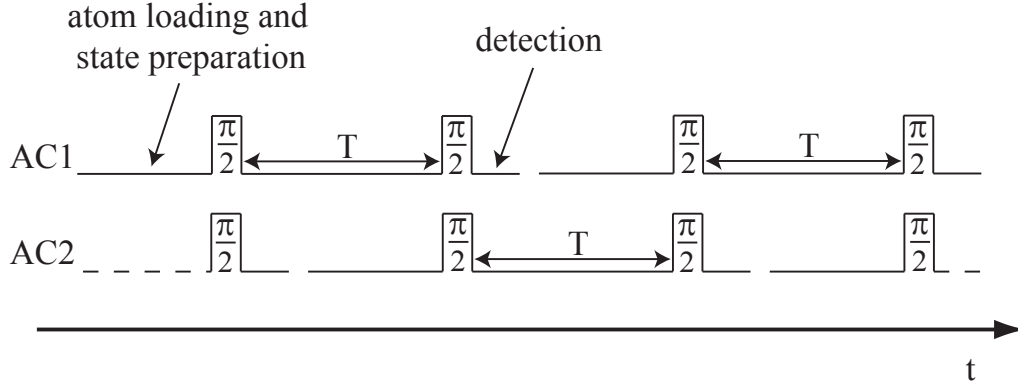


Figure 9.1: ZDT pulse sequence. Two atomic clocks are alternately operated such that the second $\frac{\pi}{2}$ -pulse of each clock is driven simultaneously with the first $\frac{\pi}{2}$ -pulse of the other. The phase contributions have opposite sign for the two clocks, so when the total accumulated phase is calculated, contributions from all but the first and final pulses cancel out.

9.2 Zero Dead Time Atomic Clock

The Dick effect can be eliminated by continuous monitoring of the LO phase. ZDT operation is achieved by alternating measurements between two interferometers referenced to the same LO, allowing for uniform coverage of the time axis. The two-clock timing sequence is shown in fig. 9.1. Each clock is operated with a duty cycle of 0.5, and interleaved such that the first (second) $\frac{\pi}{2}$ -pulse for one clock always lines up with the second (first) $\frac{\pi}{2}$ -pulse of the other. Detection of the final atomic states and loading for the subsequent cycle in one clock occurs during the interrogation time of the other clock.

The ZDT sequence starts with a $\frac{\pi}{2}$ -pulse in the first atomic clock (AC1) at time t_1 , followed by the second pulse at t_2 . Meanwhile, the second atomic clock (AC2) interrogates the atoms from t_2 to t_3 , and AC1 again from t_3 to t_4 , and so on. The

cumulative phase errors of the two clocks are given by

$$\begin{aligned}\Phi_{AC1} &= \sum_{n=1}^N \delta\phi(t_{2n}) - \delta\phi(t_{2n+1}) \\ \Phi_{AC2} &= \sum_{n=1}^N \delta\phi(t_{2n-1}) - \delta\phi(t_{2n}).\end{aligned}\quad (9.10)$$

The combined sum of the two clock outputs is therefore

$$\begin{aligned}\Phi_{AC1} + \Phi_{AC2} &= \sum_{n=1}^N (\delta\phi(t_{2n-1}) - \delta\phi(t_{2n+1})) \\ &= \sum_{n=1}^N \delta\phi(t_{2n-1}) - \sum_{n=2}^{N+1} \delta\phi(t_{2n-1}) \\ &= \delta\phi(t_1) - \delta\phi(t_{2N+1}).\end{aligned}\quad (9.11)$$

Meanwhile, the exact phase error of the LO accumulated over that time interval is also $\Phi = \delta\phi(t_1) - \delta\phi(t_{2N+1})$. The ZDT approach therefore tracks the exact phase of the LO, eliminating the random walk between the LO and atomic reference.

The standard deviation of the total measured phase over a period τ is given by

$$\sigma_\Phi(\tau) = [\sigma_{\Delta\phi}^2 + 2N\sigma_m^2]^{1/2}, \quad (9.12)$$

where there are $2N = \tau/T$ differential phase measurements made between the two clocks, each with some measurement error $\delta\phi^m$. In the limit where the phase noise in the local oscillator is much larger than the measurement uncertainty, the Allan deviation scales as

$$\sigma_y(\tau) \sim \frac{1}{\tau}. \quad (9.13)$$

The phase noise integrates down quickly under ZDT operation, until the performance becomes limited by the large number of measurements involved for long integration times τ .

9.3 Experimental Demonstration

The ZDT technique was demonstrated using two Cs fountain clocks referenced to the same local oscillator (Oscilloquartz OCXO 8607-BGE). In each atomic fountain, approximately 10^7 atoms were prepared in the $F = 3, m_F = 0$ ground state, and launched with a temperature of $2 \mu\text{K}$. A two-pulse $\frac{\pi}{2} - \frac{\pi}{2}$ Ramsey sequence with an interrogation time of $T = 215$ msec was alternately driven in the two fountains. The final atomic state distribution was measured using the same normalized fluorescence detection technique outlined in section 6.4.

The LO frequency was adjusted to tune the output of each clock onto the side of a fringe, in order to maximize the sensitivity to phase fluctuations. The fringe contrast is limited to $\sim 90\%$ due to inhomogeneities in the microwave field and bleed-through in the detection system. The microwave electronics exhibit phase noise at the 33 mrad per shot level, corresponding to a fractional frequency error of $1.8 \times 10^{-12}/\sqrt{\tau}$. Noise due to the detection system is negligibly small compared to the phase noise in the LO.

To demonstrate the performance of the ZDT scheme, 300 mrad of additional white phase noise $\delta\phi(t)$ is introduced to the LO. The added noise is monitored by mixing down the noisy microwave rf with the original LO output shifted by 1 kHz. The beatnote is sampled at 20 kHz, and the measured zero crossings are used to determine the induced phase noise [103]. The total accumulated phases for the individual clocks, as well as the combined ZDT phase are shown in fig. 9.2. The linear slope in the combined phase due to the difference between the mean LO frequency and the atomic resonance ($\omega_{LO} - \omega_{eg}$) is subtracted out.

The cumulative phase error for a single clock is given by integrating the 300 mrad phase noise over all of the dead time for that clock up to that point. This results in a random walk of the accumulated phase at a rate of $\sim 0.5 \text{ rad}/\sqrt{\text{s}}$. The ZDT phase, given by the sum of both clock outputs, follows the actual phase of the noisy LO given by the beatnote measurement within 50 mrad rms. While the single clock exhibits phase drifts up to 7 rad rms over 200 s, the total accumulated ZDT phase is limited to 440 mrad rms, representing a factor of 15 improvement in the long-term

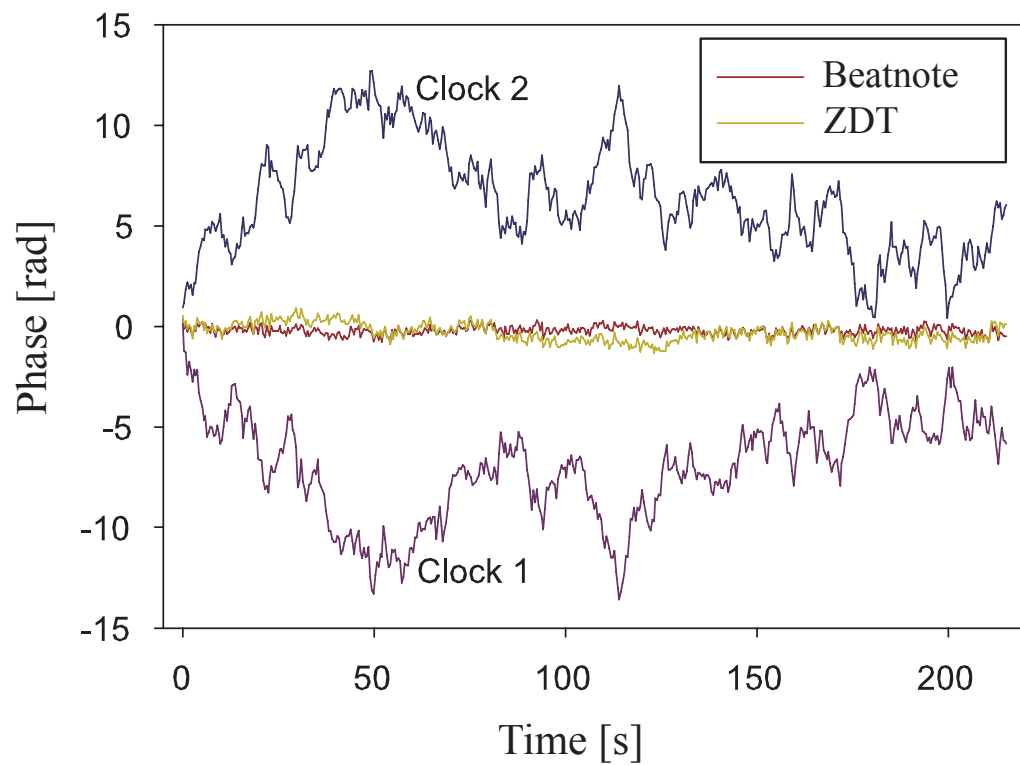


Figure 9.2: Cumulative phase measurements of the individual clocks and the ZDT system. The individual clock phases exhibit a random walk due to errors that accumulate during the dead time. The combined ZDT phase, shown in yellow, closely tracks the actual phase of the LO determined by the beatnote measurement. For this time window, ZDT operation reduces the long-term phase drift by a factor of 15.

stability.

Figure 9.3 shows the Allan deviation for both a single clock and the ZDT scheme. The single clock output integrates down as $1.3 \times 10^{-11}/\sqrt{\tau}$, typical of a system limited by white frequency noise. The ZDT output, meanwhile, exhibits a slope of $7.9 \times 10^{-12}/\tau$, and integrates down much more quickly to the noise floor of the system.

9.4 Zero Dead Time Inertial Measurements

The ZDT approach applies to inertial sensors as well. In the case of optical atom interferometers, phase noise arises from fluctuations in the optical delivery path or from the laser itself. Using the same laser beam to interrogate two alternating atomic fountains ensures that the phase noise is common to both measurements, allowing for the possibility to cancel it out. One such scheme for obtaining a continuous velocity measurement is presented here.

Consider the four-pulse $\frac{\pi}{2} - \tau - \frac{\pi}{2} - T - \frac{\pi}{2} - \tau - \frac{\pi}{2}$ sequence shown in fig. 9.4, where $T \gg \tau$. The differential phase is given by $\Delta\phi = (\phi_1 - \phi_2) - (\phi_3 - \phi_4)$. Two alternating atomic fountains are interleaved such that the first two pulses of one interferometer are synchronized with the last two pulses of the other interferometer. Thus, the differential phase of the first interferometer sequence is $(\phi_1 - \phi_2) - (\phi_3 - \phi_4)$, while the second gives $(\phi_3 - \phi_4) - (\phi_5 - \phi_6)$. Since ϕ_3 and ϕ_4 are shared by both interferometers, summing the two measurements simply gives $(\phi_1 - \phi_2) - (\phi_5 - \phi_6)$. For N consecutive measurements, the sum of the measured phases gives $(\phi_1 - \phi_2) - (\phi_{2N+1} - \phi_{2N+2})$, where the first and N th pairs of pulses are separated by a total time NT . In terms of atom position, this is

$$\Delta\phi = \mathbf{k}_{eff} \cdot ((\mathbf{x}_1 - \mathbf{x}_2) - (\mathbf{x}_{2N+1} - \mathbf{x}_{2N+2})). \quad (9.14)$$

Assuming that the accelerations are small enough that the velocity is constant over

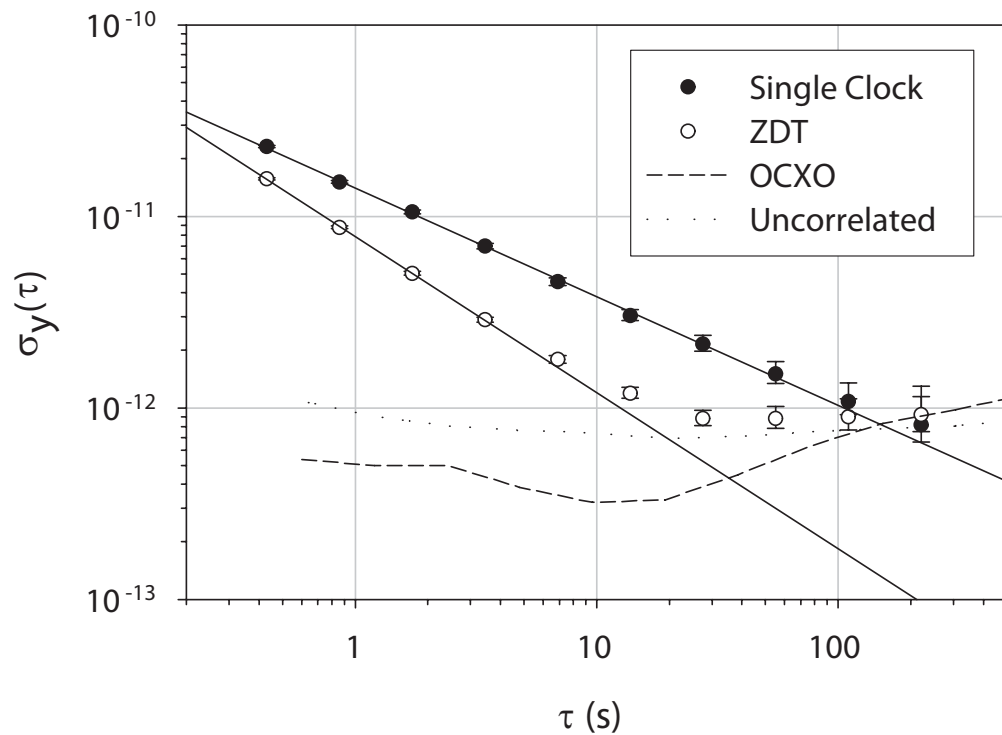


Figure 9.3: Allan deviation for a single clock and ZDT scheme. For a single clock, the Allan deviation integrates down as $1/\sqrt{\tau}$ as expected for a white noise limited measurement. Meanwhile, the combined ZDT output integrates down as $1/\tau$ because the randomly sampled phase noise cancels out for successive measurements. The short-term sensitivity of the combined signal starts a factor $\sqrt{2}$ better because it is the sum of two independent clocks.

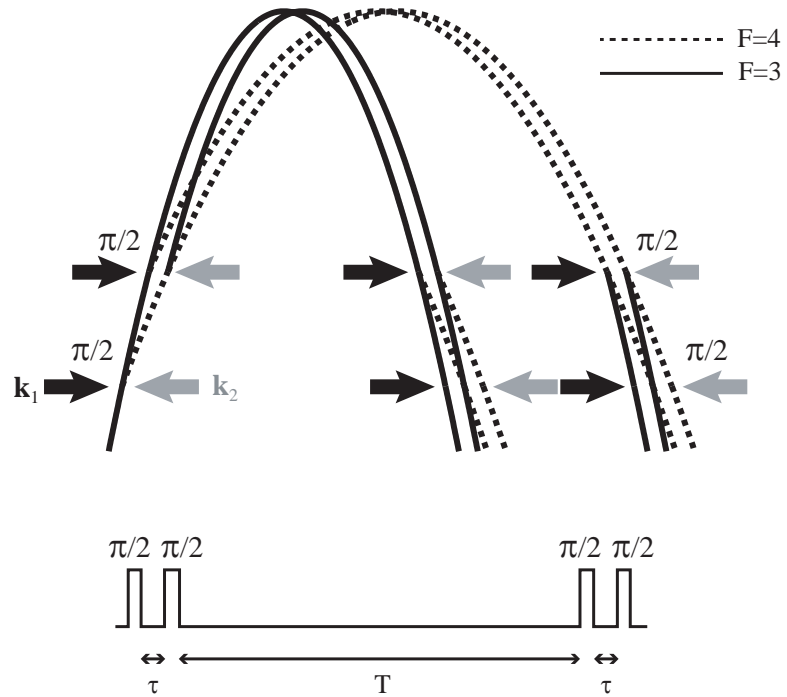


Figure 9.4: Four-pulse Ramsey-Bordé interferometer for continuous velocity measurements. The phase shift for this atom interferometer sequence is given by $\Delta\phi = (\phi_1 - \phi_2) - (\phi_3 - \phi_4)$. Interleaving two interferometers with shared Raman beams gives a total combined phase shift of $(\phi_1 - \phi_2) - (\phi_{2N+1} - \phi_{2N+2})$. For small values of τ , this reduces to a differential velocity measurement $v(t_{2N+1}) - v(t_1)$.

the short time scale τ , the phase shift expression may be written as

$$\Delta\phi \approx \mathbf{k}_{eff} \cdot (\mathbf{v}(t_{2N+1}) - \mathbf{v}(t_1))\tau, \quad (9.15)$$

thus forming the basis for a continuous velocity measurement.

Chapter 10

Conclusion

An atom interferometer based on Raman transitions in a dual atomic fountain has been developed for mobile navigation and scientific applications. Operation of the atom interferometer as a gyroscope was demonstrated, and the rotation rate of the Earth was determined with an accuracy of $\Omega/\Omega_E = 1.0007 \pm 0.0005$. The short-term sensitivity is currently limited by high frequency position jitter in the Raman mirror. A vibration compensation scheme using conventional inertial sensors to monitor the mirror position was demonstrated to suppress the vibrationally-induced phase noise by up to 50%. In addition, an operation mode for simultaneous differential and absolute acceleration measurements was demonstrated. The accelerometer/gravity gradiometer performance of the atom interferometer was evaluated by measuring the differential acceleration induced by the gravitational field of a test mass. Finally, a zero dead time technique for continuous phase monitoring of a microwave LO was demonstrated by configuring the atom interferometer as part of a dual atomic clock system.

10.1 Future Improvements

The current performance of the atom interferometer in gyroscope mode is limited by vibration noise at 400 mrad/shot, which is reduced by $\sim 50\%$ by using a single ARS-12 gyroscope to monitor the angle jitter in the Raman mirror. Even with the

vibration compensation, the gyroscope performance is still a factor of 20 away from the noise floor of the sensor as determined by the detection system. Using additional gyroscopes and linear accelerometers to monitor the Raman mirror position may allow for performance closer to the true noise floor of the system.

In the absence of vibration noise, the performance of the atom interferometer is determined by the SNR of the system, which is limited by the number of atoms detected. Increasing the atom number improves the shot noise limit, but also decreases the integration time needed to avoid technical noise sources such as optical scatter and electronic noise. This is important because it limits the amount of heating in the atoms during the detection, which can lead to additional phase noise. Currently over 90% of the atoms that are initially trapped are being thrown away by the state preparation sequence. Optical pumping could provide up to a 9 times increase in atom number. Optimizing the Cs vapor pressure and 2-D MOT beam collimations could also potentially yield a factor of 8 improvement in the 2-D MOT flux. In addition, increasing the horizontal velocity of the atoms would give a larger Doppler separation between the counter-propagating Raman modes, allowing for shorter Raman pulses. This would eliminate the need for the detection apertures that are currently being used for velocity selection, leading to a larger detected atom signal.

The rotational Sagnac phase shift for the atom interferometer scales with the enclosed area, which depends on the momentum recoil of the atoms. If the atoms were to receive a momentum recoil of $n\hbar k_{eff}$ instead of $\hbar k_{eff}$, then the rotation sensitivity would also increase by a factor of n . Large momentum recoils can be achieved, for example, by the application of multiple pulses combined with Raman wave vector reversal as described in [104]. An atom initially in the state $|F = 3, \mathbf{p}_0\rangle$ is driven into the state $|F = 4, \mathbf{p}_0 + \hbar\mathbf{k}_{eff}\rangle$ by a single π -pulse. If the Raman wave vector is reversed and a second π -pulse is applied, then the atom transitions into the state $|F = 3, \mathbf{p}_0 + 2\hbar\mathbf{k}_{eff}\rangle$. In general, the application of n successive pulses yields a total momentum recoil of $n\hbar k_{eff}$. The drawback of using extended pulse sequences is that the interferometer contrast degrades rapidly with each successive pulse, as inhomogeneities in the Raman beam lead to decoherence in the atomic ensemble. Currently the application of more than a few consecutive π -pulses washes out the

interferometer fringe completely. However, future improvements in the Raman pulse efficiencies could allow for the use of multiple $\hbar k_{eff}$ atom optics.

10.2 Future Measurements

Because the current gyroscope performance is limited by vibrations, moving the sensor to a more vibrationally quiet location would allow for better characterization of the fundamental noise floor of the system and the long-term performance limits. A measurement of the Earth rotation rate at the noise floor of the detection system would integrate down to $10^{-6} \Omega_E$ in two days without any further improvements to the interferometer. The atom interferometer is currently being prepared for an extended data run on a quiet vibration pad in the basement of the Varian physics building at Stanford.

Another possible gyroscope configuration consists of simultaneously driving the usual $\frac{\pi}{2} - \pi - \frac{\pi}{2}$ pulse sequence in two atom interferometers with staggered launching. While the four-pulse gyroscope sequence presented in this work is insensitive to constant linear accelerations, this particular configuration is insensitive to any arbitrary linear motion of the retro-reflecting mirror. The trajectories of the two interferometers are shown in fig. 10.1. The atoms in the left interferometer are launched earlier by a time T , so that they are just reaching the top Raman beam as the atoms in the right interferometer are approaching the bottom beam. The atomic trajectories in the two interferometers are essentially mirror images of each other, but with the same direction for \mathbf{k}_{eff} . As a result, the rotational Sagnac phase shift has opposite sign, while phase shifts due to constant accelerations and linear vibration noise are common to both interferometers. The difference between the two atom interferometer outputs gives the rotation rate independent of any linear vibration noise. It is, however, still sensitive to high frequency rotation noise, as the vertical separation of the two atom clouds at the first and third pulses acts as a lever arm for rotation-induced phase shifts. The staggered launch configuration, combined with the high frequency vibration compensation scheme described earlier, would make the gyroscope robust for mobile applications, opening the door for a variety of future precision rotation

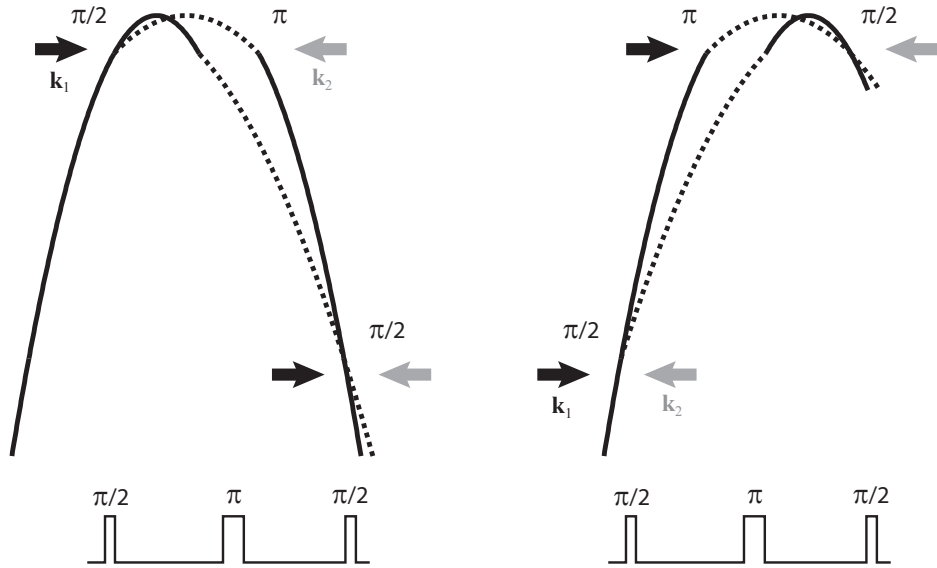


Figure 10.1: Three-pulse sequence with staggered launching. The atoms in the left interferometer are launched earlier by a time T . The rotational phase shift has opposite sign for the two atomic ensembles, while phase shifts due to linear motions have the same sign. The difference between the two interferometer signals gives the rotation rate independent of linear vibration noise.

rate measurement experiments in non-laboratory environments.

Appendix A

Fundamental Constants and Numerical Values

Quantity	Symbol	Value (SI)
Speed of light	c	$2.997\ 924\ 58 \times 10^8$ m/s
Newtonian constant of gravitation	G	$6.674\ 28(67) \times 10^{-11}$ m 3 /kg s 2
Planck's constant	\hbar	$1.054\ 571\ 628(53) \times 10^{-34}$ J s
Boltzmann constant	k_B	$1.380\ 6504(24) \times 10^{-23}$ J/K
(unified) atomic mass unit	u	$1.660\ 538\ 782(83) \times 10^{-27}$ kg
Earth rotation rate	Ω_E	$7.292\ 115 \times 10^{-5}$ rad/s
Earth equatorial radius	R	$6.378\ 1378(26) \times 10^6$ m
Earth mass	M	$5.972\ 19 \times 10^{24}$ kg
Sidereal day		86164.1 s

Table A.1: A list of relevant fundamental constants and numerical values. Fundamental constants are CODATA internationally recommended values from NIST database [105]. Numerical values for Earth parameters are from [106].

Appendix B

Cesium Properties

Quantity	Symbol	Value (SI)
Atomic number	Z	55
Atomic mass [107]	m	132.905 451 931(27)u
Nuclear spin	I	7/2
Melting point		28°C
Cooling transition frequency [108]	$\omega/2\pi$	351.725 718 50(11) THz
Wavelength	λ	852.347 275 82(27) nm
Natural linewidth	$\gamma/2\pi$	5.18 MHz
Saturation intensity	I_{sat}	1.09 mW/cm ²
Doppler temperature	T_D	124.39 μK
Recoil temperature	T_{rec}	198 nK
Hyperfine frequency	$\omega_{HFS}/2\pi$	9.192 631 770 GHz
Two-photon recoil velocity	v_{rec}	7.04 mm/s
Two-photon recoil Doppler shift	$\omega_{rec}/2\pi$	8.265 kHz

Table B.1: Properties of ^{133}Cs . The cooling transition frequency refers to the $6^2S_{1/2}, F = 4 \rightarrow 6^2P_{3/2}, F' = 5$ transition. The hyperfine splitting is for the $6^2S_{1/2}$ level $F = 3$ and $F = 4$ ground states.

Appendix C

Laser Frequencies

Below is an energy level diagram of the Cs D_2 -line, showing the laser frequencies used in the atom interferometry experiments. The AOM shifts for generating the frequencies used for trapping, launching, and detecting the atoms are also shown. The Raman master laser is locked to the $F = 3$ master laser with a programmable offset $\Delta_{offset} \sim 1$ GHz, and the two Raman frequencies are generated by phase modulating the Raman slave at 9.2 GHz.

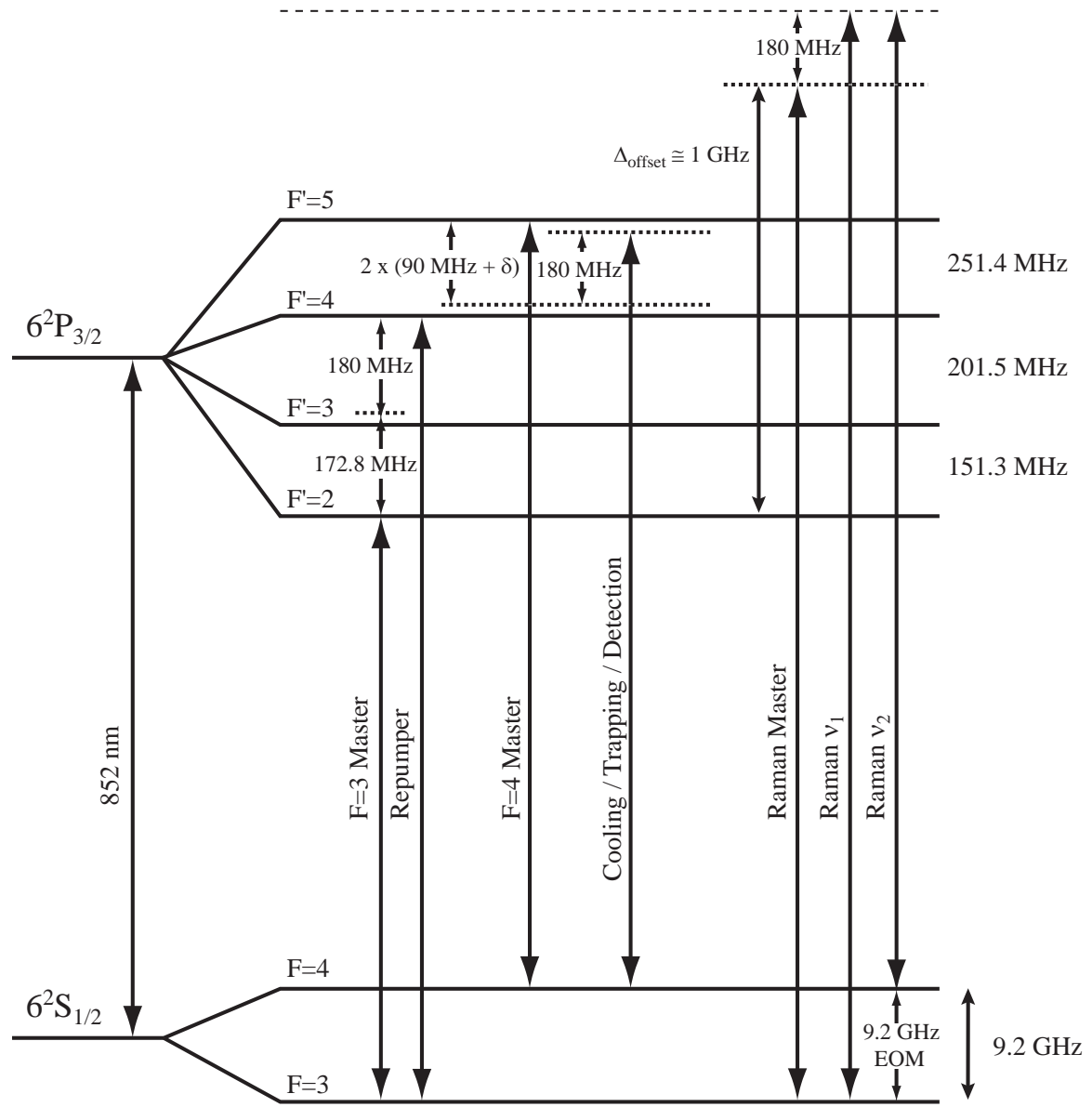


Figure C.1: Cs energy level diagram showing the different laser frequencies used in the experiment.

Bibliography

- [1] J. F. Wagner, “From Bohnenberger’s machine to integrated navigation systems, 200 years of inertial navigation,” in “Photogrammetric Week ’05,” (Wichmann Verlag, Heidelberg, 2005).
- [2] Space Studies Board, Board on Physics and Astronomy, Commission on Physical Sciences, Mathematics, and Applications, and National Research Council, *Review of Gravity Probe B* (National Academy Press, 1995).
- [3] L. de Broglie, “Recherches sur la théorie des quanta (Research on quantum theory),” Ph.D. thesis, Paris (1924).
- [4] C. Davisson and L. H. Germer, “Diffraction of electrons by a crystal of nickel,” *Phys. Rev.* **30**, 705–740 (1927).
- [5] G. P. Thomson and A. Reid, “Diffraction of cathode rays by a thin film,” *Nature (London)* **119**, 890 (1927).
- [6] N. F. Ramsey, “A molecular beam resonance method with separated oscillating fields,” *Phys. Rev.* **78**, 695–699 (1950).
- [7] R. Colella, A. Overhauser, and S. Werner, “Observation of gravitationally induced quantum interference,” *Phys. Rev. Lett.* **34**, 1472 (1975).
- [8] O. Carnal and J. Mlynek, “Young’s double-slit experiment with atoms: A simple atom interferometer,” *Phys. Rev. Lett.* **66**, 2689–2692 (1991).
- [9] D. W. Keith, C. R. Ekstrom, Q. A. Turchette, and D. E. Pritchard, “An interferometer for atoms,” *Phys. Rev. Lett.* **66**, 2693–2696 (1991).

- [10] F. Riehle, T. Kisters, A. Witte, J. Helmcke, and C. J. Bordé, “Optical Ramsey spectroscopy in a rotating frame: Sagnac effect in a matter-wave interferometer,” *Phys. Rev. Lett.* **67**, 177 (1991).
- [11] M. Kasevich and S. Chu, “Atomic interferometry using stimulated Raman transitions,” *Phys. Rev. Lett.* **67**, 181–184 (1991).
- [12] G. Sagnac, “L’éther lumineux démontré par l’effet du vent relatif d’éther dans un interféromètre en rotation uniforme,” *Comptes Rendus de l’Academie des Sciences* **157**, 708–710 (1913). [The existence of light ether demonstrated by the effect of the relative ether wind on a uniformly rotating interferometer].
- [13] A. A. Michelson and H. G. Gale, “The effect of the Earth’s rotation on the velocity of light, Part II,” *Astrophys. J.* **61**, 140 (1925).
- [14] W. M. Macek and D. T. M. Davis, Jr., “Rotation rate sensing with traveling-wave ring lasers,” *Appl. Phys. Lett.* **2**, 67–68 (1963).
- [15] V. Vali and R. W. Shorthill, “Fiber ring interferometer,” *Appl. Opt.* **15**, 1099–1100 (1976).
- [16] S. Altshuler and L. M. Frantz, “United States patent no. US 3,761,721,” (1973).
- [17] L. A. Page, “Effect of Earth’s rotation in neutron interferometry,” *Phys. Rev. Lett.* **35**, 543 (1975).
- [18] J. Anandan, “Gravitational and rotational effects in quantum interference,” *Phys. Rev. D* **15**, 1448 (1977).
- [19] S. A. Werner, J.-L. Staudenmann, and R. Colella, “Effect of Earth’s rotation on the quantum mechanical phase of the neutron,” *Phys. Rev. Lett.* **42**, 1103 (1979).
- [20] J. F. Clauser, “Ultra-high sensitivity accelerometers and gyroscopes using neutral atom matter-wave interferometry,” *Physica B* **151**, 262–272 (1988).

- [21] A. Lenef, T. D. Hammond, E. T. Smith, M. S. Chapman, R. A. Rubenstein, and D. E. Pritchard, “Rotation sensing with an atom interferometer,” *Phys. Rev. Lett.* **78**, 760 (1997).
- [22] T. L. Gustavson, P. Bouyer, and M. A. Kasevich, “Precision rotation measurements with an atom interferometer gyroscope,” *Phys. Rev. Lett.* **78**, 2046–2049 (1997).
- [23] F. Hasselbach and M. Nicklaus, “Sagnac experiment with electrons: Observation of the rotational phase shift of electron waves in vacuum,” *Phys. Rev. A* **48**, 143 (1993).
- [24] T. L. Gustavson, A. Landragin, and M. A. Kasevich, “Rotation sensing with a dual atom-interferometer Sagnac gyroscope,” *Class. Quantum Grav.* **17**, 2385 (2000).
- [25] A. Peters, K. Y. Chung, and S. Chu, “High-precision gravity measurements using atom interferometry,” *Metrologia* **38**, 25–61 (2001).
- [26] M. J. Snadden, J. M. McGuirk, P. Bouyer, K. G. Haritos, and M. A. Kasevich, “Measurement of the Earth’s gravity gradient with an atom interferometer-based gravity gradiometer,” *Phys. Rev. Lett.* **81**, 971–974 (1998).
- [27] J. M. McGuirk, G. T. Foster, J. B. Fixler, M. J. Snadden, and M. A. Kasevich, “Sensitive absolute-gravity gradiometry using atom interferometry,” *Phys. Rev. A* **65**, 033,608 (2002).
- [28] J. B. Fixler, G. T. Foster, J. M. McGuirk, and M. A. Kasevich, “Atom interferometer measurement of the Newtonian constant of gravity,” *Science* **315**, 74–77 (2007).
- [29] D. S. Weiss, B. C. Young, and S. Chu, “Precision measurement of the photon recoil of an atom using atomic interferometry,” *Phys. Rev. Lett.* **70**, 2706–2709 (1993).

- [30] C. Will, *Theory and Experiment in Gravitational Physics* (Cambridge University Press, New York, 1993).
- [31] C. J. Bordé, A. Karasiewicz, and P. Tourrenc, “General relativistic framework for atomic interferometry,” *Int. J. Mod. Phys. D* **3**, 157–161 (1994).
- [32] S. Wajima, M. Kasai, and T. Futamase, “Post-Newtonian effects of gravity on quantum interferometry,” *Phys. Rev. D* **55**, 1964–1970 (1997).
- [33] S. Dimopoulos, P. W. Graham, J. M. Hogan, and M. A. Kasevich, “Testing general relativity with atom interferometry,” *Phys. Rev. Lett.* **98** (2007).
- [34] J. Audretsch and K.-P. Marzlin, “Ramsey fringes in atomic interferometry: Measurability of the influence of space-time curvature,” *Phys. Rev. A* **50**, 2080–2095 (1994).
- [35] *Hyper-Precision Cold Atom Interferometry in Space (HYPER)*, “Assess. Study Rep. ESA-SCI(2000)10,” Tech. rep., European Space Agency (2000).
- [36] R. Y. Chiao and A. D. Speliotopoulos, “Towards MIGO, the matter-wave interferometric gravitational-wave observatory, and the intersection of quantum mechanics with general relativity,” *J. Mod. Opt.* **51**, 861–899 (2004).
- [37] S. Foffa, A. Gasparini, M. Papucci, and R. Sturani, “Sensitivity of a small matter-wave interferometer to gravitational waves,” *Phys. Rev. D* **73** (2006).
- [38] P. Delva, M.-C. Angonin, and P. Tourrenc, “Matter waves and the detection of Gravitational Waves,” *J. Phys.: Conf. Ser.* **66** (2007).
- [39] C. Jekeli, “Precision free-inertial navigation with gravity compensation by an onboard gradiometer,” *J. of Guidance, Control, and Dynamics* **29**, 704–713 (2006).
- [40] J. Kwon and C. Jekeli, “Gravity requirements for compensation of ultra-precise inertial navigation,” *Eur. J. Navig. 3* **58**, 479–492 (2005).

- [41] N. Yazdi, F. Ayazi, and K. Najafi, “Micromachined inertial sensors,” *Proc. IEEE* **86**, 1640 (1998).
- [42] DARPA Precision Inertial Navigation Systems (PINS), Defense Sciences Office.
<http://www.darpa.mil/dso/thrusts/physci/newphys/pins/index.htm>.
- [43] G. E. Stedman, “Ring-laser tests of fundamental physics and geophysics,” *Rep. Prog. Phys.* **60**, 615–688 (1997).
- [44] A. Cochard, H. Igel, B. Schuberth, W. Suryanto, A. Velikoseltsev, U. Schreiber, J. Wassermann, F. Scherbaum, and D. Vollmer, *Earthquake Source Asymmetry, Structural Media and Rotation Effects* (Springer, Berlin, 2006), chap. “Rotational Motions in Seismology: Theory, Observation, Simulation”, pp. 391–411.
- [45] K. U. Schreiber, G. E. Stedman, H. Igel, and A. Flaws, *Earthquake Source Asymmetry, Structural Media and Rotation Effects* (Springer, Berlin, 2006), chap. “Ring Laser Gyroscopes as Rotation Sensors for Seismic Wave Studies”, pp. 377–390.
- [46] M. Takeo and H. M. Ito, “What can be learned from rotational motions excited by earthquakes?” *Geophys. J. Int.* **129**, 319–329 (1997).
- [47] B. F. Chao, R. S. Gross, and Y.-B. Han, “Seismic excitation of the polar motion, 1977–1993,” *PAGEOPH* **146**, 407–419 (1996).
- [48] R. S. Gross, “Combinations of Earth orientation measurements: SPACE97, COMB94, and POLE94,” *J. Geophys. Res.* **101**, 8729–8740 (1996).
- [49] B. F. Chao and R. D. Ray, “Oceanic tidal angular momentum and Earth’s rotation variations,” *Prog. Oceanogr.* **40**, 399–421 (1997).
- [50] J. Wahr, “The Earth’s rotation rate,” *Am. Scientist* **73**, 41 (1985).
- [51] H. R. Bilger, “Low frequency noise in ring laser gyros,” *Proc. SPIE* **487**, 42–48 (1984).

- [52] M. O. Scully, M. S. Zubairy, and M. P. Haugan, “Proposed optical test of metric gravitation theories,” *Phys. Rev. A* **24**, 2009–2016 (1981).
- [53] J. Lense and H. Thirring, “Über den einfluss der eigenrotation der zentralkörper auf die bewegung der planeten und monde nach der einsteinschen gravitations-theorie,” *Physikalische Zeitschrift* **19**, 156–163 (1918). [On the influence of the proper rotation of central bodies on the motions of planets and moons according to Einstein’s theory of gravitation].
- [54] L. I. Schiff, “Possible new experimental test of general relativity theory,” *Phys. Rev. Lett.* **4**, 215–217 (1960).
- [55] J. Mester, *Gravitation and Experiment* (Birkhäuser Basel, Switzerland, 2007), chap. “Testing Einstein in Space: The Gravity Probe B Relativity Mission”, pp. 101–109.
- [56] Gravity Probe B, “Post Flight Analysis - Final Report,” Tech. rep., NASA (2007).
- [57] C. Lämmerzahl and G. Neugebauer, *Gyros, Clocks, Interferometers...: Testing Relativistic Gravity in Space* (Springer, Berlin, 2001), chap. “The Lense-Thirring Effect: From the Basic Notions to the Observed Effects”, pp. 31–51.
- [58] A. Delgado, W. P. Schleich, and G. Süssmann, “Quantum gyroscopes and Gödel’s universe: entanglement opens a new testing ground for cosmology,” *New J. Phys.* **37**, 1–8 (2002).
- [59] A. H. Rosenthal, “Regenerative circulatory multiple-beam interferometry for the study of light-propagation effects,” *J. Opt. Soc. Am.* **52**, 1143–1148 (1962).
- [60] R. W. Dunn, D. E. Shabalin, R. J. Thirkettle, G. J. MacDonald, G. E. Stedman, and K. U. Schreiber, “Design and initial operation of a 367 m² rectangular ring laser,” *Appl. Opt.* **41**, 1685–1688 (2002).
- [61] H. E. Ives, “Light signals sent around a closed path,” *J. Opt. Soc. Am.* **28**, 296–299 (1938).

- [62] G. B. Malykin, “The Sagnac effect: correct and incorrect explanations,” *Physics-Uspekhi* **43**, 1229–1252 (2000).
- [63] T. W. Kornack, R. K. Ghosh, and M. V. Romalis, “Nuclear spin gyroscope based on an atomic comagnetometer,” *Phys. Rev. Lett.* **95** (2005).
- [64] F. E. Zimmer and M. Fleischhauer, “Quantum sensitivity limit of a Sagnac hybrid interferometer based on slow-light propagation in ultracold gases,” *Phys. Rev. A* **74**, 063,609 (2006).
- [65] R. E. Packard and S. Vitale, “Principles of superfluid helium gyroscopes,” *Phys. Rev. B* **46**, 3540–3549 (1992).
- [66] O. J. Woodman, “An introduction to inertial navigation,” Tech. Rep. UCAM-CL-TR-696, University of Cambridge (2007).
- [67] H. Xie and G. Fedder, “Fabrication, characterization, and analysis of a DRIE CMOS-MEMS gyroscope,” *IEEE Sensors Journal* **3**, 622–631 (2003).
- [68] Applied Technology Associates, ARS-12B MHD Angular Rate Sensor Product Specifications.
- [69] O. Avenel, Y. Mukharsky, and E. Varoquaux, “Superfluid gyrometers,” *J. Low Temp. Phys.* **135**, 745–772 (2004).
- [70] S. J. Sanders, L. K. Strandjord, and D. Mead, “Fiber optic gyro technology trends - a Honeywell perspective,” in “Optical Fiber Sensors Conference Technical Digest,” (2002), pp. 5–8.
- [71] G. E. Stedman, K. U. Schreiber, and H. R. Bilger, “On the detectability of the Lense-Thirring field from rotating laboratory masses using ring laser gyroscope interferometers,” *Class. Quantum Grav.* **20**, 2527 (2003).
- [72] D. S. Durfee, Y. K. Shaham, and M. A. Kasevich, “Long-term stability of an area-reversible atom-interferometer Sagnac gyroscope,” *Phys. Rev. Lett.* **97**, 240,801 (2006).

- [73] B. Young, M. Kasevich, and S. Chu, *Atom Interferometry* (Academic Press, San Diego, CA, 1997), chap. “Precision Atom Interferometry with Light Pulses”, pp. 363–406.
- [74] H. J. Metcalf and P. van der Straten, *Laser Cooling and Trapping* (Springer, 1999).
- [75] L. Allen and J. H. Eberly, *Optical Resonance and Two-Level Atoms* (John Wiley and Sons, Inc., 1975).
- [76] D. J. Wineland and W. M. Itano, “Laser cooling of atoms,” *Phys. Rev. A* **20**, 1521–1540 (1979).
- [77] J. Dalibard and C. Cohen-Tannoudji, “Laser cooling below the Doppler limit by polarization gradients: simple theoretical models,” *J. Opt. Soc. Am. B* **6**, 2023–2083 (1989).
- [78] M. A. Kasevich, E. Riis, S. Chu, and R. G. DeVoe, “RF spectroscopy in an atomic fountain,” *Phys. Rev. Lett.* **63**, 612–615 (1989).
- [79] M. Kasevich, D. S. Weiss, E. Riis, K. Moler, S. Kasapi, and S. Chu, “Atomic velocity selection using stimulated Raman transitions,” *Phys. Rev. Lett.* **66**, 2297–2300 (1991).
- [80] K. Moler, D. S. Weiss, M. Kasevich, and S. Chu, “Theoretical analysis of velocity-selective Raman transitions,” *Phys. Rev. A* **45**, 342–348 (1992).
- [81] R. P. Feynman and A. R. Hibbs, *Quantum Mechanics and Path Integrals* (McGraw-Hill, New York, 1965).
- [82] P. Storey and C. Cohen-Tannoudji, “The Feynman path integral approach to atomic interferometry,” *J. Phys. II (France)* **4**, 1999–2027 (1994).
- [83] C. Antoine, “Matter wave beam splitters in gravito-inertial and trapping potentials: generalized ttt scheme for atom interferometry,” *Appl. Phys. B* **84**, 585–597 (2006).

- [84] K.-P. Marzlin and J. Audretsch, “State independence in atom interferometry and insensitivity to acceleration and rotation,” *Phys. Rev. A* **53** (1996).
- [85] B. Dubetsky and M. A. Kasevich, “Atom interferometer as a selective sensor of rotation or gravity,” *Phys. Rev. A* **74** (2006).
- [86] K. Takase, J. K. Stockton, and M. A. Kasevich, “High-power pulsed-current-mode operation of an overdriven tapered amplifier,” *Optics Lett.* **32**, 2617–2619 (2007).
- [87] Zerodur is a registered trademark of Schott Glass Technologies, Inc.
- [88] D.-H. Gwo, “United States patent no. US 6,284,085 B1,” (2001).
- [89] S. Rowan, S. M. Twyford, J. Hough, D.-H. Gwo, and R. Route, “Mechanical losses associated with the technique of hydroxide-catalysis bonding of fused silica,” *Phys. Lett. A* **246**, 471–478 (1998).
- [90] G. W. Biedermann, “Gravity tests, differential accelerometry, and interleaved clocks with cold atom interferometers,” Ph.D. thesis, Stanford University (2007).
- [91] M. Kasevich, “Atom interferometry in an atomic fountain,” Ph.D. thesis, Stanford University (1992).
- [92] G. W. Biedermann, X. Wu, L. Deslauriers, K. Takase, and M. A. Kasevich, “Low-noise simultaneous fluorescence detection of two atomic states,” *Optics Lett.* (2007). To Be Published.
- [93] National Geodetic Survey Geodetic Toolkit, Surface Gravity Prediction, <http://www.ngs.noaa.gov/TOOLS/Gravity/gravcon.html>.
- [94] B. Canuel, F. Leduc, D. Holleville, A. Gauguet, J. Fils, A. Virdis, A. Clairon, N. Dimarcq, C. J. Bordé, and A. Landragin, “Six-axis inertial sensor using cold-atom interferometry,” *Phys. Rev. Lett.* **97**, 010,402 (2006).

- [95] G. T. Foster, J. B. Fixler, J. M. McGuirk, and M. A. Kasevich, “Method of phase extraction between coupled atom interferometers using ellipse-specific fitting,” *Optics Lett.* **27**, 951–953 (2002).
- [96] J. K. Stockton, X. Wu, and M. A. Kasevich, “Bayesian estimation of differential interferometer phase,” *Phys. Rev. A* **76**, 033,613 (2007).
- [97] L. Essen and J. V. L. Parry, “An atomic standard of frequency and time interval: A caesium resonator,” *Nature* **176**, 282 (1955).
- [98] G. J. Dick, “Local oscillator induced instabilities in trapped ion frequency standards,” in “Proceedings of the 19th Annual Precise Time and Time Interval (PTI) Applications and Planning Meeting,” (1988), pp. 133–147.
- [99] G. Santarelli, P. Laurent, P. Lemonde, A. Clairon, A. G. Mann, S. Chang, A. N. Luiten, and C. Salomon, “Quantum projection noise in an atomic fountain: A high stability cesium frequency standard,” *Phys. Rev. Lett.* **82**, 4619–4622 (1999).
- [100] A. G. Mann, S. Chang, and A. N. Luiten, “Cryogenic sapphire oscillator with exceptionally high frequency stability,” *IEEE Trans. Instrum. Meas.* **50**, 519–521 (2001).
- [101] J. Guéna, G. Dudle, and P. Thomann, “An experimental study of intermodulation effects in an atomic fountain frequency standard,” *Eur. Phys. J. Appl. Phys.* **38**, 183–189 (2007).
- [102] A. Joyet, G. Milet, G. Dudle, and P. Thomann, “Theoretical study of the Dick effect in a continuously operated Ramsey resonator,” *IEEE Trans. Instrum. Meas.* **50**, 150–155 (2001).
- [103] D. W. Allan, J. H. Shoaf, and D. Halford, *Characterization of Frequency Stability* (IEEE Trans. on Instrum. and Meas., 1973), chap. 8, “Statistics of Time and Frequency Data Analysis”, pp. 151–204.

- [104] J. M. McGuirk, M. J. Snadden, and M. A. Kasevich, “Large area light-pulse atom interferometry,” *Phys. Rev. Lett.* **85**, 4498–4501 (2000).
- [105] The NIST Reference on Constants, Units, and Uncertainty, <http://physics.nist.gov/cuu/Constants/index.html>.
- [106] B. H. Chovitz, “Parameters of common relevance of astronomy, geodesy, and geodynamics,” *J. Geodesy* **62**, 359–367 (1988).
- [107] M. P. Bradley, J. V. Porto, S. Rainville, J. K. Thompson, and D. E. Pritchard, “Penning trap measurements of the masses of ^{133}Cs , $^{87,85}\text{Rb}$, and ^{23}Na with uncertainties ≤ 0.2 ppb,” *Phys. Rev. Lett.* **83**, 4510–4513 (1999).
- [108] T. Udem, J. Reichert, T. W. Hänsch, and M. Kourogi, “Absolute optical frequency measurement of the cesium D_2 line,” *Phys. Rev. A* **62**, 031,801 (2000).